Chair of Physical Metallurgy and Metallic Materials

Doctoral Thesis

Defects and their influence on mechanical properties in nitrides: an atomistic study

Dipl.-Ing. Lukas Löfler, BSc.

April 2022

MONTANUNIVERSITÄT LEOBEN
www.unileoben.ac.at

EIDESSTATTLICHE ERKLÄRUNG

Ich erkläre an Eides statt, dass ich diese Arbeit selbständig verfasst, andere als die angegebenen Quellen und Hilfsmittel nicht benutzt, und mich auch sonst keiner unerlaubten Hilfsmittel bedient habe.

Ich erkläre, dass ich die Richtlinien des Senats der Montanuniversität Leoben zu "Gute wissenschaftliche Praxis" gelesen, verstanden und befolgt habe.

Weiters erkläre ich, dass die elektronische und gedruckte Version der eingereichten wissenschaftlichen Abschlussarbeit formal und inhaltlich identisch sind.

Datum 28.04.2022

Unterschrift Verfasser/in
Lukas Löfler

Acknowledgements

During my doctoral studies, I had the pleasure to work with and meet countless great people. I am especially grateful to my colleagues from the Computational Materials Science group at Montanuniversität Leoben and the Materials Science Division at TU Wien. My special gratitude belongs to the following few.

To my supervisor **David Holec** for giving me the opportunity of continuing to work with you after my master thesis. I am grateful for all the travel opportunities the initiation for establishing contacts and the independence and trust you gave me to do my work. I was able to learn a lot from you, and I am thankful for all your support, advice, know-how, patience and open ears you had for me all these years.

To **Paul Mayerhofer** for taking me in, his support, knowledge and excitement for every new result.

To **Matthias Bartosik** for his open ear, discussions and insightful comments and for allowing me to be part of our joint project.

To **Antonia Wagner**, **Nikola Koutná** and **Julian Buchinger** for being the best office mates one can wish for. I enjoyed our discussions, and the time we could spend together in and out of the office. To **Vincent Moraes, Lukas Zauner, Stefan Kagerer, Alexander Kirnbauer, Philipp Ertelthaler and Helmut Riedl-Tragenreif** for providing the best work environment I could ever imagine.

To my **family** and **friends** for accompanying me on my journey.

Contents

Abbreviations

afm anti-ferromagnetic

CTB coherent twin boundary

CVD chemical vapour deposition

DFT Density Functional Theory

fm ferromagnetic

HAADF high-angle annular dark-field

HRTEM high-resolution transmission electron microscopy

MD molecular dynamics

pm paramagnetic

PVD physical vapour deposition

SL superlattices

SQS special quasi-random structure

TMN transition-metal nitrides

Abstract

Transition metal nitride-based thin films are commonly used as protective coatings in applications with demanding environments such as cutting tools or turbine blades. The high demand for such coatings drives a significant research effort to improve their hardness, fracture toughness, thermal stability and resistance against wear, oxidation and corrosion. One approach for improvement is to carefully introduce defects in the material systems to tune their properties. Another possibility is to design a microstructure, such as creating a multilayered system.

In this work, atomisitc simulations within the scope of Density Functional Theory (DFT) and classical molecular dynamics (MD) were used to investigate the impact of microstructure and defects on the mechanical properties of cubic transition metal nitride thin films. Atomistic simulations allow us to study phenomena and processes at the atomic level granting access to information that is not accessible otherwise, or only with great efforts.

Using DFT simulations in this thesis, we could show that vacancies in the $Mo_xAl_{1-x}N$ system stabilise the metastable cubic MoN and improve the elastic constants for low Al contents. The role of the microstructure, namely the superlattice architecture, was studied on AlN/CrN, TiN/CrN and AlN/TiN multilayers. The fracture toughness of AlN/CrN and TiN/CrN superlattices was predicted using DFT. The results show that a discrete interface description is necessary to model the systems and that approximations (e.g., the method of Grimsditsh and Nizzoli) can sometimes lead to wrong results. Our calculations also revealed that the magnetic nature of CrN is not reflected in lattice parameter oscillations. Additionally, we calculated the energy barrier while moving a twin boundary in CrN for various processes and confirmed that an asynchronous process is energetically preferred. It results in a termination of the twin boundary with a nitrogen plane, as observed experimentally.

Next, we performed tensile loading and nanoindentation simulations using molecular dynamics for the AlN/TiN system with different bilayer periods. Utilising the larger number of

atoms in MD calculations allowed us to study the development of dislocation networks, phase transformations and cracks. We could show toughening for small bilayer periods driven by a phase transformation in the AlN and differences in the failure mechanisms dependent on the loading direction and bilayer period. The nanoindentation simulations pointed towards intermixing of the layers, driven by the plastic deformation; this leads to weakening the superlattice structure.

Kurzfassung

Übergangsmetallnitrid-Dünnschichten werden häufig als Schutzschichten von Bauteilen die in harschen Umgebungen zum Einsatz kommen, wie zum Beispiel in beim Zerspanen oder in Turbinen. Die große Nachfrage an solchen Bauteilen treibt eine umfangreiche Forschungstätigkeit zur Verbesserung von Härte, Festigkeit, thermischer Stabilität, sowie Widerstand gegen Verschleiß, Oxidation und Korrosion. Ein Weg zur Manipulation von Materialeigenschaft ist die gezielte Einbringung von Punktdefekten, eine andere ist eine sorgfältig gewählte Mikrostruktur wie zum Beispiel mehrschichtige Systeme.

In dieser Arbeit wurden atomistische Simulationen auf Basis von Dichte Funktional Theorie (DFT) und Molekulardynamik (MD) durchgeführt um den Einfluss von Mikrostruktur und Defekten auf die mechanischen Eigenschaften von kubischen Übergangmetallsnitrid-Dünnschichten zu untersuchen. Atomistische Simulationen geben die Möglichkeit Phänomene und Prozesse zu studieren die in Experimente nicht oder nur schwer zugänglich sind.

Mit Hilfe von DFT Simulationen konnten wir demonstrieren, dass Leerstellen in dem $Mo_xAl_{1-x}N$ System die metastabile Phase von MoN stabilisieren und die mechanischen Eigenschaften für niedrige Al Konzentrationen verbessern. Die Rolle der Mikrostruktur wurde anhand von AlN/CrN, TiN/CrN und AlN/TiN Mehrlagensystemen untersucht. Die Bruchzähigkeit von AlN/CrN und TiN/CrN konnte mittels DFT Simulationen bestimmt werden. Die Ergebnisse verdeutlichen die Notwendigkeit für eine explizite Beschreibung der Grenzfläche, da Näherungen (z.B. die Methode von Grimsditsh and Nizzoli) zu falschen Resultaten führen können. Es wurde demonstriert dass die magnetischen Momente in den einzelnen CrN Lagen keinen Effekt auf die Oszillationen des Gitterparmeters haben. Weiters wurde die nötige Energiebarriere um eine Zwillingsgrenze in CrN zu bewegen für verschiedene Prozesse berechnet. Dabei konnten wir einen asynchronen Prozess als den energetisch Bevorzugten bestätigen. Dieser resultiert in einer Stickstoff terminierten Zwillingsgrenze, welche auch experimentell beobachtet wurde.

Folgend wurden Zug- und Nanoindentationversuche an AlN/TiN Mehrlagensystemen mittels Molekularerdynamik-Simulationen durchgeführt. Durch die große Anzahl an Atomen in MD Simulationen konnten wir die Entstehung von Versetzungen, Phasentransformation und Rissen untersuchen. Wir demonstrierten eine Steigerung der Festigkeit durch Phasentransformation in den AlN Schichten mit kleiner Lagentdicke sowie eine Abhängigkeit des Versagensmechanismus an der Belastungsrichtung. Nanoindentation zeigte eine Vermischung der verschiedenen Lagen durch plastische Deformation, welche zu einer Schwächung der Mehrlagenstruktur führt.

Chapter 1

Introduction

To keep up with the requirements of modern production and applications, a constant need for improvements of material properties drives both academic as well as industrial research. In many cases, the surface of a component is the critical region that has to withstand the harshest environmental impacts. The surface needs to provide protection against chemical, thermal and mechanical influences. To do so, the surface material has to exhibit high hardness and toughness, excellent resistance against oxidation and corrosion, and high chemical and thermal stability. To decouple the properties of surfaces from the bulk of a component, one can cover the component with a thin film coating. This gives the possibility to produce a surface specifically tuned to the environment of the operation. Such thin films can be produced in several ways, such as chemical vapour deposition chemical vapour deposition (CVD) or physical vapour deposition physical vapour deposition (PVD), which is typically the technique used to deposit the coatings investigated in this thesis. The principle of PVD is to bombard a target with ions of a plasma. Upon the impact of these ions, the transferred energy ejects ions out of the target material, which travel and adhere to the surface of the to be coated component, also called substrate. The far from equilibrium thermodynamics in PVD, going from a gas phase directly to solid, allows for synthesis of immiscible material or metastable phases, which is not possible with other techniques. To improve the coatings themselves, there are two main approaches: I) search for new material combinations or II) design a microstructure within the coating to tune the desired properties. A straightforward way to create a controlled microstructure is a multilayered architecture. This can be done by alternating the film's chemical and/or structural composition periodically and thus creating layers with different properties. Doing so allows tuning the film's mechanical, electric, magnetic , and tribological properties[1–3].

This thesis focuses mainly on ceramic superlattices (SL), which are a specific type of mul-

tilayer coatings defined by coherently grown layers thicknesses of just a few nanometers. In the following, a more detailed account of the possible improvements of the mechanical properties of thin films due to a SL structure is given.

1.1 Protective coatings

Ceramic thin film coatings are commonly used to enhance the properties of components to withstand the ever-increasing requirements of modern applications [4]. In many cases, both high hardness and fracture toughness are sought after, which are, however, often mutually exclusive [5].

The protective hard coatings are typically synthesised by either physical vapour deposition (PVD) or chemical vapour deposition (CVD) [6]. Several approaches are available to tune the coating's properties. Considering monolithic films, the material composition can be fine-tuned by additional alloying element(s) or the controlled introduction of defects in order to enhance various functional properties such as oxidation resistance [7–10] or thermal stability [3, 11–13]. Microstructural design concepts include nanocomposite coatings. [14–17], superlattice/multilayer coatings [2, 18–20] or advanced (hierarchical) architectures [21–23]. We note that the references given above are by far not exhaustive and should serve the reader as a starting point for further exploring the rich existing literature. Importantly, each of the mentioned categories contains simulation/modelling contributions, demonstrating their role in modern materials science.

1.2 Superlattices

The superlattice/multilayer configurations consist of layers of alternating materials and often show improved properties (see Fig. 1.1). Superlattices are a subset of multilayered coatings. They are classified by their (semi-)coherently interface between the individual layers. The layers themself are of a few nanometers of thickness. In most cases, the constituents of the multilayer are of the same crystallographic structure and miscible such as rocksalt-TiN and rocksalt-CrN in TiN/CrN SLs. There are some exceptions, such as bcc-Mo and rocksalt-NbN, for example. To create a (semi)-coherent interface, the lattice has to be rotated by 45° resulting in an interface between the $(1\bar{1}0)$ direction of Mo and the (100) of NbN [24]. One of the critical features of SLs is the bilayer period (Λ), which is the thickness of one pair of consecutive layers. The bilayer period and the crystallographic orientations of the layers are responsible for achieving desired sublattices effects in the coating.

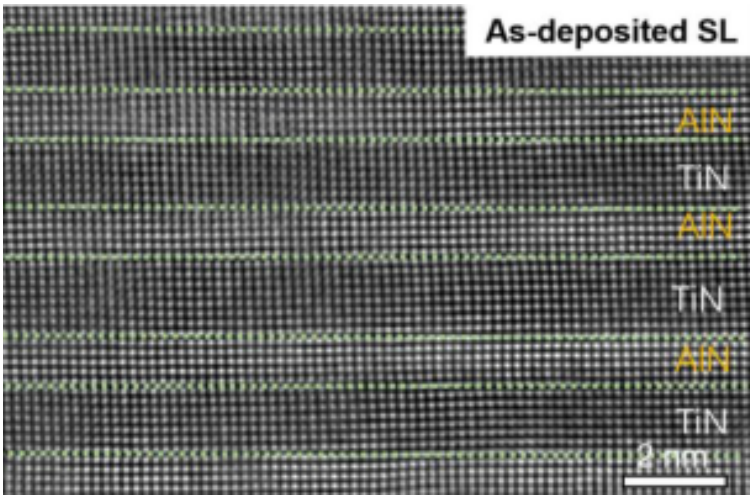

Figure 1.1: High-resolution TEM image of as-deposited TiN/AlN superlattice [29].

Concerning transition-metal nitrides (TMN), it was shown that SLs can improve mechanical properties such as hardness and fracture toughness. This was shown, e.g. for TiN/VN and TiN/CrN superlattices [1, 2]. Another positive effect of SLs in the epitaxial stabilisation of metastable phases. Here especially the metastable cubic phase of AlN is of interest, which can be stabilised in multilayers as shown for AlN/TiN and [25, 26] and AlN/CrN [27, 28].

1.3 Strategies to increase hardness

For protection against mechanical wear, high hardness is crucial. The demand for coating with a high hardness led to great research efforts with the goal of improving the hardness of coatings. The most commonly used concept to achieve these goals is to hinder the movement of dislocation and grain boundaries. Successful approaches to so so are alloying, e.g. solid solutions of $Ti_xAl_{1-x}N$ [30, 31] and $Mo_xAl_{1-x}N$ [32, 33], the growth of nanocomposites [34] or intentionally introducing vacancies into the material [35–37]. In superlattices, the interfaces hinder dislocation movement efficiently and strengthen the coating. The strong influence of the interfaces in superlattices on the hardness was shown early on [2] [38]. The increase in hardness due to the hinderance of dislocation motion has two accepted explanations. The first one is related to the difference in shear moduli between the different layers. The second one explanation relates the increase in harness to the periodic stress-strain fields in the layers, which stem from the lattice mismatch between the constituents. [24, 39–41].

The model proposed by Chu and Barnett [24] and Barnett and Madan [39] is in good quantitative agreement with experimental findings in metals and nitrides regarding the found maximum of hardness/strength dependent on the bilayer period. The model is based on

the assumptions that the materials of the superlattice are miscible and have the same slip systems to allow dislocation migration through the interface. The different shear moduli of the different constituting layers cause the dislocation line energy changes at the interface when a dislocation has to move from one material to the other. This hinders the movement of the dislocation and increases the hardness/strength of the SLs [25].

After the peak, the hardness/strength decreases with a further increase of Λ, governed by the glide of dislocations within the individual layers. The maximum is located where the required stresses to move a dislocation for both mechanisms are of the same value. The case of immiscible Sls with a sharp interface and the same slip systems is trivial. They exhibit higher hardness/strength at small Λ with little change a larger values [24]. When the individual layers exhibit different glide systems, the slip across the interfaces is the limiting factor for small bilayer periods.

The coherency stresses stem from the mismatch of the lattice parameters between the materials of the individual layers. To allow the lattice planes to match over the whole thickness (i.e. over all layers), the difference in the lattice parameters has to be compensated by elastic strains within the layer. The introduced strain field exhibits forces on the dislocation impeding their movement through the interfaces and increasing the strength of the SLs. However, this is only true for small Λ. In thicker layers, the strains can be relaxed by the nucleation of dislocations[42]. Overall the effect on the hardness is considered much smaller compared to the effect of the shear module difference [39].

Already in 1987, Helmersson *et al.* [2] showed that TiN/VN multilayers exhibit an increased hardness compared to bulk TiN. Similar trends were also reported for CrN/AlN [28], TiN/CrN [18], TiN/WN [19] and MoN/TaN [20]. Later studies on superlattices showed an additional increase in the coating's fracture toughness peaking at certain bilayer periods depending on the combined materials, TiN/CrN [18], TiN/WN [19] or MoN/TaN [20]. The nature of these coatings, namely a small bilayer period for which the enhancement of the mechanical properties is observed, introduces a significant amount of "interface material". This is the interface between the individual layers and their nearest region, which significantly differs from the bulk by the broken (chemical) symmetry on both sides of the interface. Therefore, it is expected to play a key role in determining both the hardness and the fracture toughness of superlattices and small bilayer period multilayers. Recently, Hahn *et al.* [1] reported that the fracture toughness of TMNs superlattices is susceptible to the superlattice effect as well (see next section).

Nevertheless, despite this great progress, the exact mechanisms behind the outstanding

mechanical properties of nitride superlattices are not yet fully understood.

1.4 Increase in fracture toughness

The high strength of transition metal nitrides makes them resilient against the initial formation of a crack when free from defects. The existence of a pre-existing crack, however, proves to be fatal since already minor strain can lead to crack propagation, hence damaging the component fatally. The material choice often falls on weaker materials with higher toughness to avoid failure [43]. To make TMN coatings more applicable in demanding modern applications, increasing their fracture toughness is essential.

A high fracture toughness requires both high strength and ductility of the material. To quantify it, in 1921, Griffith [44] suggested that the fracture strength (σ_f) is dependent on the Young's modulus (E) and the surface energy (γ) according to

$$\sigma_f \approx \sqrt{\frac{1}{\pi a} 2\gamma E} \, , \tag{1.1}$$

with a as the length of the crack. Griffith based his theory on linear elastic fracture mechanics ignoring any plastic deformations at the crack tip. For brittle materials, such as glasses, this is a good approximation. Ductile materials, such as metals, require the consideration of additional energy terms to describe the plastic region at the crack tip. To accommodate the plastic behaviour, Irwin [45] replaced the surface energy with the total dissipated energy (G). With that, Eq. (1.1) changes to

$$\sigma_f = \sqrt{\frac{1}{\pi a} GE} = \sqrt{\frac{1}{\pi a} (2\gamma + G_p) E} \, . \tag{1.2}$$

Here, G_p mainly contains the energy required for the plastic deformation (friction in dislocation movement (heat)) and any other form of energy dissipation. For ductile materials $G_p \gg \gamma$ whereas for brittle materials the inverse relation is true and $G_p \ll \gamma$. To describe the stress state, in relation to an external load, around the vicinity of the crack tip, the stress intensity factor (K) was proposed by Irwin. K is dependent on the magnitude and distribution of the load and the geometry of both the component and the crack [46]. K can be described with the following equation:

$$K = \sigma \sqrt{\pi a} \cdot f(a/W) \, , \tag{1.3}$$

with σ being the applied stress, a the crack length and $f(a/W)$ the geometry factor dependent on the specimens geometry and its width W. To distinguish between different loading

scenarios, K is subscribed with I, II and III [47]. For the mode, I, in which the load is perpendicular to the crack (tensile loading), the stress intensity factor is denoted as K_I. Mode II describes in-plane shear (sliding), with the corresponding stress intensity factor K_II, while the mode III is related to other loading scenarios with out-of-plane shear (tear) and a corresponding stress intensity factor K_III. To propagate a crack in a mode I scenario, one can define the minimal K_I as the *critical* stress intensity factor K_{IC} [46, 47]. K_{IC} a widely accepted parameter for quantifying the fracture toughness materials. To determine the fracture toughness experimentally, both pillar splitting [48] and micro-cantilever [49, 50] experiments are often utilised.

There are two approaches to improve the fracture toughness: either to increase the hardness to prevent forming cracks (intrinsic) or, after a crack is formed, hindering any further crack propagation extrinsic). The intrinsic ways to improve the fracture toughness include changing the structure and bonding of the initial material, adding microstructural features of additives per phase or transformation-induced toughening. Extrinsic approaches include toughening by nanostructural design, e.g. by the superlattice structure.

In contrast to hardness, the effect of superlattices on fracture toughness was the focus of research only in recent years. Nanocrystal TiN/amorphous-(W,Ti)$C_{0.}$68 superlattices were prepared by Zhang in 2011, exhibiting super hardness (52 GPa) in combination with decent toughness (590 MPa)[51]. Micromechanical bending tests on CrN/Cr and TiN/SiO_x superlattices films showed an increase in fracture toughness of up to 40 and 60 % respectively, compared to the individual constituents [43]. The enhancement in fracture toughness was attributed to the significant difference in elastic moduli in TiN/SiO_x on the one hand and the difference in the strength of the individual materials in CrN/Cr superlattices on the other hand. It was suggested that the combination of microstructural heterogeneity and the different intrinsic mechanical properties increase the fracture toughness in brittle materials, altering the crack path and deflecting it at the interface.

Later on Hahn *et al.* [1] could show for CrN/Tin SLs that both the hardness and the fracture toughness of the coatings show the same behaviour in relation to the bilayer thickness. At a bilayer period of ≈ 6 nm both properties have their respective peak. This study could show that it is possible to simultaneously improve both properties with superlattice structure.

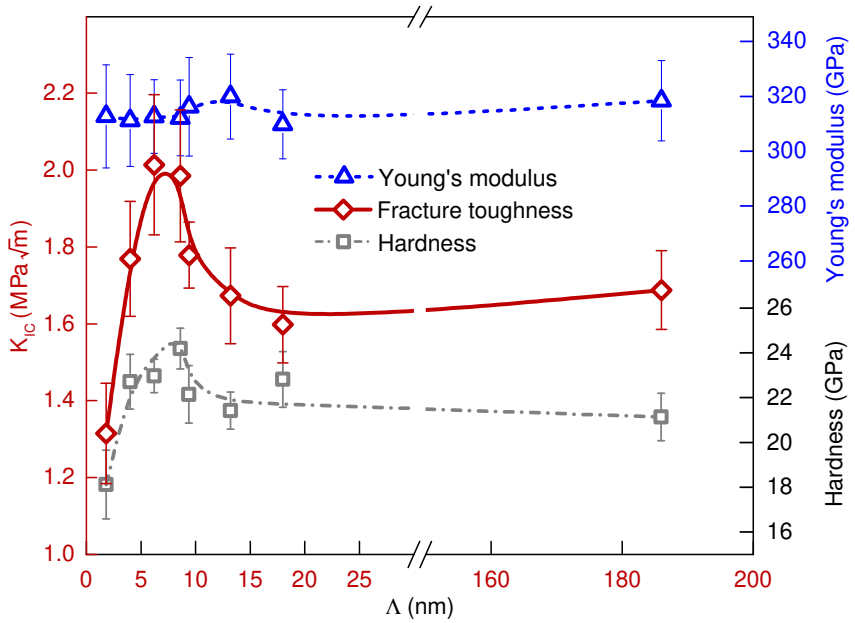

Figure 1.2: Fracture toughness (KIC), hardness (H) and Youngs's modulus (E) of CrN/TiN superlattices over the bilayer period (Λ)[1]. This figure by Hahn *et al.* shows the simultaneous increase of hardness and fracture toughness at small Λ

1.5 Superlattice phase stabilisation

The superlattice structure allows the stabilisation of metastable phases. The mechanism behind the stabilisation is the template effect. During the layered growth, The deposited layer on the top strongly influences the layer currently growing during the layered growth. Such templating allows for the new layer to deposit in a metastable crystal structure, which typically has positive effects on the strength of the superlattice. The metastable cubic rocksalt phase of AlN is desired for its good mechanical properties exceeding those of the hexagonal ground state. However, a spontaneous formation of the rs structure requires high pressures of over 22 GP at room temperature [52] and still 14–16.5 GPa at 1800 K[53]. In superlattices, however, it is possible to stabilise AlN in its rocksalt structure, as shown for TiN/AlN [25, 26, 54] and CrN/AlN [27, 55] multilayers with small layer thicknesses of 1.5–3 nm.

Chapter 2

Materials

The studied materials in this thesis are nitride ceramics, namely CrN/TiN, CrN/AlN and AlN/TiN superlattices (SLs) as well as $Mo_xAl_{1-x}N$ solid solution thin films. All materials were considered in the cubic rock-salt (B1) structure, with space group #225, $Fm\bar{3}m$. The motivations for choosing those systems were multi-fold and are detailed in the respective results section. In short, the SLs with CrN as one of the constituents were mainly investigated to determine the influence of different magnetic configurations of the CrN on the mechanical properties. AlN/TiN was chosen as a material system to investigate the impact of the SL effect on mechanical properties because of the availability of a reliable classical molecular dynamics potential. This provided the opportunity to computationally study SLs on a larger scale, including extended defects. Finally, point and planar defects were investigated in $Mo_xAl_{1-x}N$ and CrN, respectively, as inspired by available experimental data.

The following sections provide a brief overview of the different studied nitrides.

2.1 Transition Metal Nitrides

Transition metal nitrides (TMNs) are a group of materials with an interesting mix of properties. They have high melting points, strength and incompressibility, are both good heat and electric conductors and are stable under thermal and chemical influences [56, 57]. TMNs are often used as thin films to tune the surface of a component to a specific application. These can range from protective coatings for cutting tools or structural components [58, 59] over diffusion barriers in integrated circuits [60] and energy storage and energy conversion [61, 62]. Some TMNs (TiN, VN, NbN, TaN) can exhibit superconductive behaviour at temperatures of 6–18 K e.g. TiN exhibiting critical temperature $T_c = 5.49\,\mathrm{K}$ [63] or NbN with $T_c = 17.3\,\mathrm{K}$ [64].

Considering the structure of transition metal nitrides one finds that the cubic rock salt phase (B1, $Fm\bar{3}m$) is present for all nitrides of transition metals from the groups IV-VI, including **TiN**, ZrN and HfN in group IV; VN, NbN and TaN in group V and **CrN**, **MoN** and WN in group VI [65]. The TNMs studied in the scope of this work are all in their B1 phase. We note, however, that the thermodynamically stable structures of NbN, TaN, MoN and WN are different (mostly hexagonal) structures whose stability may, moreover, depend on temperature; nonetheless, they all can be stabilised in the cubic B1 phase.

The bonds in transmission metal nitrides are of covalent, ionic and metallic nature. The high mechanical strength and the good chemical stability stem from the directional nature of the covalent and ionic bonds. The metallic part of the bonding is responsible for the electrical conductivity, good adhesion and ductility [66]. The interactions of p(N)–d(TM) and d(TM)-d(TM) orbitals (N = nitrogen, TM = transition metal) in rocksalt, TMNs are the main contribution to the good mechanical properties [67].

2.1.1 CrN

In industrial applications, CrN coatings are valued for their good wear, oxidation and corrosion resistance [68]. At room temperature, CrN assumes the cubic B1 (rock-salt, $Fm\bar{3}m$) structure in a paramagnetic state with a lattice constant of $a = 4.148\,\text{Å}$ [69]. Below the Néel temperature ($\approx 273\,\text{K}$), a phase transformation impacting both the structure and the magnetic configuration happens [70]. The crystal structure, considering now the antiferromagntic periodicity, changes to an orthorhombic ($Pnma$) like shape, with a small deviation from the 90 °angles with $\alpha \approx 88.3°$. The magnetic configuration switches to antiferromagnetic with alternating double (110) planes with spin up and spin down Cr atoms [69, 70]. The elastic constants of paramagnetic CrN are reported to be 540, 27 and 88 GPa[71, 72] for C_{11}, C_{12} and C_{44} respectively. CrN thin films show hardness of 23–30 GPa [73, 74] and fracture toughness of $3.13\,\text{MPa}\sqrt{\text{m}}$ [48].

2.1.2 TiN

TiN is part of the group IV transition metal nitrides. It exhibits a number of favourable properties, which is why TiN is one of the most commonly chosen TMN for modern applications. TiN has high hardness [75], low friction coefficient and wear resistance, and slow bulk diffusion making it an excellent diffusion barrier and is a decent electric conductor ($250\,\mu\Omega\text{cm}$) [76]. With that, TiN finds its use as protective coatings for cutting tools or

other harsh environments [77, 78], in micro electric applications or fuel cells and batteries [79]. Due to its golden colour, TiN coatings offer themselves also as decorative coatings. The structure of TiN is the cubic rock-salt structure (B1, $Fm\bar{3}m$), whereas a wide range off-stoichiometric compositions, mostly due to N vacancies, is accessible. Coatings of TiN_x with x ranging between 0.67–1.3 were successfully synthesised. TiN coatings have a hardness of 20–30 GPa [75], a fracture toughness of 2–3 MPa$\sqrt{\text{m}}$ [80–82] and a Young's modulus of 320 GPa [83]. The wide spread can be attributed to the different concentrations of vacancies or microstructure in general in the different studies.

2.1.3 MoN

Compared to other TMNs, stoichiometric MoN is not an often investigated system. The reason for this is that MoN is neither mechanically nor dynamically stable in the cubic B1 structure but can be stabilised by the presents of vacancies. Non-stoichiometric MoN_x has a higher ductility compared to other brittle TMNs (TiN, ZrN and VN). Both theoretical[84, 85] and experimental [86, 87] studies showed that alloying other transition metal nitrides with Mo increases the ductility by softening of the elastic shear modulus while still maintaining high strength[]. The improvement in toughness is attributed to an increase in valence electrons due to a higher amount of the $4d$ orbitals. Bulk MoN exhibits a wide range of phases [89] dependent on the parameters and technique used for its deposition. MoN_x in its cubic B1 structure can have desired properties for ultraviolet optical applications, exhibiting negative or near-zero real permittivity paired with a low resistivity at room temperature [90]. The low friction coefficient and wear rate of MoN make it a good candidate for tribological coatings [91, 92]. The addition of Al in MoN is expected to have a positive effect on its oxidation resistance and mechanical properties. Similar behaviour was found for TiAlN and CrAlN. The use as a tribological coating is limited by the preferred formation of volatile molybdenum oxides at elevated temperatures [91]. Under a thermodynamic equilibrium, AlN was found not to be miscible with Mo [93]. However, with the high quenching rates of physical vapour deposition (PVD), it was possible to stabilise $Mo_xAl_{1-x}N_y$ showing that the Al stabilises the cubic phase of MoN up to an AlN mole fraction of $x = 0.57$, whereas a wurtzite phase was obtained for higher AlN contents [32]. The reported mechanical properties are not fully consistent. For example, Yang *et al.* [94] reported hardness values decrease from ≈ 30 GPa for $x = 0$ to below 20 GPa for $x = 0.33$. The same behaviour but with even greater changes was published by Xu *et al.*, with a change from 28.9 GPa at $x = 0$ to 12.3 GPa at $x = 0.35$. On the contrary, Klimashin, Euchner, and Mayrhofer [32] reported an increase in

hardness for the range $x = 0.20$–0.55 with a hardness plateau of $\approx 37\,\mathrm{GPa}$. The reported data for the elastic moduli span a range of 223–450 GPa for $x = 0.35$[32, 94]. All reported values were for coatings stabilised in the cubic phase, however, with different concentrations of both metal and nitrogen vacancies (and possibly also different microstructure).

2.2 AlN

AlN is not a transition metal nitride, but as a member of the group III-nitrides, it is sometimes classified as a post-transition metal nitride, following the notation of Al as a post transition metal. It is both chemically and radiation inert, it exhibits a high melting point (over 3200 K), high thermal conductivity ($55\,\mathrm{Wm^{-1}K^{-1}}$) [95] a Young's modulus of 273 GPa [95] and a hardness of 23 GPa [95]. This makes AlN suitable for many applications, including high-temperature resistors, heat sinks, LEDs, and optical sensors [96, 97]. The high thermal and mechanical stability allows AlN to be used in applications with high friction and wear [95]. AlN has both covalent and ionic bonding and is known in three structural configurations. The ground-state is the hexagonal wurtzite w-AlN (B4, $P6_3mc$) phase, which is valued for its piezoelectric properties and its use in the semiconductor industry. The metastable cubic phases rocksalt rs-AlN (B1, $Fm\bar{3}m$) and zincblende zb-AlN(B3, $F43m$), both exhibit high mechanical and good structural properties, making them desirable for protective coatings [96, 97]. The two cubic phases only differ in their coordination geometry, with an octahedral coordination for the B1 phase and a tetrahedral coordination for the B3 phase. DFT studies revealed that a uniaxial tension of zincblende AlN along the [110] direction leads to a phase transition to the rock-salt phase [98]. Similarly, the wurtzite (B4) to rocksalt (B1) phase transformation can be triggered by a uniaxial tension along the hexagonal $[\bar{1}2\bar{1}0]$ direction or by a shear in the $(10\bar{1}0)[\bar{1}2\bar{1}0]$ slip system [99].

Chapter 3

Computational methods

3.1 Density Functional Theory

Density functional theory (DFT) is a first principles (*ab initio*) method to compute quantum-mechanical (QM) interactions between atoms without the need of any prior knowledge. This allows, in principle, to study any composition and structure of interest. With the ever improving computational resources, *ab initio* simulations became a pillar of materials science. They allow for insight where experiments are either not possible or are too expensive; furthermore, they can predict the behaviour of not yet synthesised materials and guide the experiments towards the discovery of new materials. With density functional theory, it is possible to study a wide variety of phenomena ranging from band gaps to simple lattice constants. The section below provides a short explanation of the theoretical concepts behind DFT is given.

Many-Body problem

For any solid-state material, one has to consider many atoms or particles that interact with each other. Such systems are called *many-body problems*. For a QM system, this task is to solve the many-body Schrödinger equation:

$$\hat{H}\psi_i(\vec{x}_1, \vec{x}_2, \ldots, \vec{x}_N, \vec{R}_1, \vec{R}_2, \ldots, \vec{R}_M) = E_i\psi_i(\vec{x}_1, \vec{x}_2, \ldots, \vec{x}_N, \vec{R}_1, \vec{R}_2, \ldots, \vec{R}_M) \tag{3.1}$$

with the Hamiltonian $\hat{H}$ describing N electrons and M atoms in a state ψ_i with E_i as the total energy of the system. Without any external field and in the cgs unit system[1] $\hat{H}$ is:

$$\hat{H} = -\frac{1}{2}\sum_{i=1}^{N}\nabla_i^2 - \frac{1}{2}\sum_{A=1}^{M}\frac{1}{M_A}\nabla_A^2 - \sum_{i=1}^{N}\sum_{A=1}^{M}\frac{Z_A}{r_{iA}} + \sum_{i=1}^{N-1}\sum_{j>i}^{N}\frac{1}{r_{ij}} + \sum_{A=1}^{M-1}\sum_{B>A}^{M}\frac{Z_A Z_B}{R_{AB}}\ . \tag{3.2}$$

[1]The cgs unit system is a variant of the metric system, simplifying the equations. cgs Wikipedia

A and B are indices for different atomic cores, and i and j correspond to the electrons in the system. The first two terms describe the kinetic energy of the electrons and nuclei, respectively. The other three terms describe the electrostatic interactions between electrons with nuclei, electrons with electrons and nuclei with nuclei. The wave function ψ_i contains all possible information about the system. E_i is the energy of the state described by ψ_i.

It is possible to simplify the Schrödinger equation using the *Born-Oppenheimer approximation*. The approximation takes into consideration the large difference in mass between electrons and nuclei. Due to this difference, the electrons move much faster than the nuclei, and the atom cores can be considered stationary. Consequently, the kinetic and the electrostatic interaction of nuclei are separated as they constitute a constant value from the perspective of solving the electronic sub-system:

$$\hat{H}_{elec} = -\frac{1}{2}\sum_{i=1}^{N}\nabla_i^2 - \sum_{i=1}^{N}\sum_{A=1}^{M}\frac{Z_A}{r_{iA}} + \sum_{i=1}^{N}\sum_{j>i}^{N-1}\frac{1}{r_{ij}} = \hat{T} + \hat{V}_{Ne} + \hat{V}_{ee} \ . \tag{3.3}$$

Solving the Schrödinger equation with $\hat{H}_{elec}$ as the Hamiltonian delivers the electronic wave function, ψ_{elec}, and the electronic energy, E_{elec}.

$$\hat{H}_{elec}\psi_{elec} = E_{elec}\psi_{elec} \ . \tag{3.4}$$

The attractive potential V_{Ne} between the nuclei and the electrons is later on termed as V_{ext}, as it is the 'external' field for the electrons. The total energy, E_i, is the sum of E_{elec} and E_{nuc}:

$$E_i = E_{elec} + E_{nuc} \tag{3.5}$$

with

$$E_{nuc} = \sum_{A=1}^{M-1}\sum_{B>A}^{M}\frac{Z_A Z_B}{R_{AB}} + \hat{T}_{\mathrm{nuc}} \ . \tag{3.6}$$

With the assumption of stationary nuclei, there is no kinetic term for the nuclei. In the further explanation, the annotation 'elec' is left out since only the electronic sub-system is considered.

The square of the wave function represents the probability that the electrons $1, 2, \ldots, N$ are found in the infinitesimally small volumes at $\vec{x}_1$, $\vec{x}_2$,..,$\vec{x}_N$. Due to the fermionic nature of the electrons, $\psi(=\psi_{elec})$ must be antisymmetric, as requested by the *Pauli exclusion principle*:

$$\psi(\vec{x}_1, \vec{x}_2, \ldots, \vec{x}_i, \ldots, \vec{x}_j, \ldots, \vec{x}_N) = -\psi(\vec{x}_1, \vec{x}_2, \ldots, \vec{x}_j, \ldots, \vec{x}_i, \ldots, \vec{x}_N) \ . \tag{3.7}$$

The wave function ψ_0 which delivers the lowest energy of the system describes the ground state of the system. This energy is called the ground state energy E_0 and can be written as:

$$E_0 = \min_{\psi} E[\psi] = \min_{\psi} \langle \psi | \hat{T}_e + \hat{V}_{Ne} + \hat{V}_{ee} | \psi \rangle \ . \tag{3.8}$$

Theorems of Hohenberg and Kohn

The idea of Hohenberg and Kohn was to use the electron density, ρ, instead of the wave function to solve the N-electron problem. Thereby, the problem changes from a $3N$-dimensional to a 3-dimensional one. This leads to a reduction of the computational effort to solve the problem to a practical level. They formulated and proved two theorems that show that the electron density of the system is able to describe it fully [100].

The first theorem of Hohenberg and Kohn states that *"the external potential $V_{\text{ext}}(\vec{r})$ is (to within a constant) a unique functional of $\rho(\vec{r})$"*. Since in turn $V_{\text{ext}}(\vec{r})$ fixes $\hat{H}$, we see that the full many-particle ground state is uniquely determined by $\rho(\vec{r})$. This means that the state of a many-body system can be uniquely described by its charge density $\rho(\vec{r})$.

Hohenberg–Kohn's universal functional is defined as:

$$F[\rho(\vec{r})] = T[\rho(\vec{r})] + V_{\text{el}}[\rho(\vec{r})] \ , \tag{3.9}$$

where $T[\rho(\vec{r})]$ is the functional for the kinetic energy of electrons and $V_{\text{el}}[\rho(\vec{r})]$ is the functional for the electron-electron interaction. This functional is the essence of the density functional theory. If it were known exactly, one could have solved the many-body problem without any further approximation. Sadly, this is not the case and only the Coulomb term from $V_{\text{el}}[\rho(\vec{r})]$ can be extracted while all the quantum-mechanical interactions have to be approximated. The functional is completely independent from the calculated system. This universality allows it to be applied to hydrogen as well as large molecules such as DNA or a plethora of bulk systems.

The second theorem of Hohenberg and Kohn states that:

$$H[\rho(\vec{r})] = F[\rho(\vec{r})] + V_{\text{ext}}[\rho(\vec{r})] \qquad E_{\text{GS}} = H[\rho_0] \tag{3.10}$$

is minimised by and only by the true ground state density ρ_0. In the above equation, $F[\rho(\vec{r})]$ is the universal (H-K) functional of the electron density, V_{ext} is the external potential and E_{GS} is the ground state energy of the system corresponding to the ground state electron density ρ_0.

Kohn-Sham Approach

The H-K theorem is a variational approach and hence it is not well suited for practical solutions. Therefore, Kohn and Sham [101] proposed to construct ρ using one-electron orbitals ϕ_i corresponding to a fictitious system of non-interacting particles:

$$\rho(\vec{r}) = \sum_i |\phi_i(\vec{r})|^2 \ . \tag{3.11}$$

The Kohn-Sham approach combines the ideas of Hartree-Fock and Hohenberg-Kohn, and developed a non-interacting reference system in a way so that the majority of the kinetic energy can be calculated accurately [100]. The remaining part of the kinetic energy is put together with other interacting terms of the one-electron system into the exchange-correlation energy E_{XC}:

$$E_{\mathrm{XC}} = E_X + E_C^{\mathrm{int}} + E_{\mathrm{kin}}^{\mathrm{int}} \ . \tag{3.12}$$

Now, the total DFT energy can be written using the following terms:

$$E = F[\rho(\vec{r})] + E_{\mathrm{ext}} = E_{\mathrm{kin}}^{\mathrm{non}} + E_{\mathrm{ext}} + E_H + E_{\mathrm{XC}} \ . \tag{3.13}$$

The first three terms can be calculated easily, but the last one is subject to approximations. The corresponding Hamiltonian to the energy above can be expressed with the following equation:

$$\hat{H}_{\mathrm{KS}} = \hat{T}_{\mathrm{kin}}^{\mathrm{non}} + \hat{V}_{\mathrm{ext}} + \hat{V}_H + \hat{V}_{\mathrm{XC}} = -\frac{1}{2}\nabla^2 + \hat{V}_{\mathrm{eff}} \ . \tag{3.14}$$

where $\hat{V}_{\mathrm{eff}}$ is the effective potential of the non-interacting system with the electron density, which results in the solution of the interacting system. In the following, we take a brief look at the individual energy terms.

Kinetic Energy

The kinetic term in the non-interacting system can be expressed as:

$$E_{\mathrm{kin}}^{\mathrm{non}} = -\frac{1}{2}\sum_{i=1}^{N} \int \phi_i^*(\vec{r})\nabla^2\phi_i(\vec{r})d\vec{r} \tag{3.15}$$

Due to the Nabla operator, the electron density from Eq. (3.11) can not be used directly, and the kinetic energy is calculated using the KS orbitals as shown in (3.15).

External Energy

The external potential V_{ext} originates from the interaction of electrons with the nuclei. Its energy is determined by:

$$E_{\mathrm{ext}}[\rho(\vec{r})] = \sum_{i=1}^{N} \int \phi_i^*(\vec{r})V_{\mathrm{ext}}(\vec{r})\phi_i(\vec{r})d\vec{r} = \int V_{\mathrm{ext}}(\vec{r})\rho(\vec{r})d\vec{r} \ . \tag{3.16}$$

As one can see, the external energy is determined by the electron density.

Hartree Energy

In the non-interacting system, the Hartree potential describes the electrostatic interaction between a unit charge at $\vec{r}$ and the mean electron density at the position $\vec{r'}$:

$$V_H(\vec{r}) = \int \frac{\rho(\vec{r'})}{|\vec{r} - \vec{r'}|} d\vec{r'} \ , \tag{3.17}$$

which requires an integral over $\vec{r'}$ when evaluating $V_H(\vec{r})$.The Hartree energy can be expressed as:

$$E_H[\rho(\vec{r})] = \frac{1}{2} \int V_H(\vec{r})\rho(\vec{r}) d\vec{r} = \frac{1}{2} \iint \frac{\rho(\vec{r})\rho(\vec{r'})}{|\vec{r} - \vec{r'}|} d\vec{r} d\vec{r'} \ . \tag{3.18}$$

Thus the calculated energy is purely classical and of a coulombic nature. A convenient way to represent the potential through the electron density is, therefore, via the Poisson's equation:

$$\nabla^2 V_H(\vec{r}) = -4\pi\rho(\vec{r}) \ . \tag{3.19}$$

Exchange and Correlation Energy

The final term of the total energy is the XC energy. This term contains all the quantum-mechanical effects. The XC energy can be split into two terms, $E_{\mathrm{XC}} = E_X + E_C$. Here, E_X is the exchange term between electrons with the same spin due to the Pauli repulsion and E_C is the correlation term between electrons with opposite spins. The exchange term can be described as:

$$E_X = -\frac{1}{2} \sum_{i,j=1}^{N} \iint \frac{\phi_i^*(\vec{r})\phi_j^*(\vec{r'})\phi_i(\vec{r'})\phi_j(\vec{r})}{|\vec{r} - \vec{r'}|} d\vec{r} d\vec{r'} \tag{3.20}$$

In theory, E_X can be calculated exactly. If this is done, the DFT method becomes equivalent to the Hartree-Fock approximation, which scales poorly with the number of electrons. Therefore, E_X is approximated in DFT calculations. The exchange term, in general, leads to a reduced overlap of the electron orbitals. The same is true for the correlation term. Although the possibility of two electrons with opposite spins can occupy the same state, there is a repulsive force due to their charge. This part is the N-electron effect that was not included in the Hartree-Fock method and is also subject to an approximation. For typical materials, the correlation energy is small compared to the exchange term.

There are different approaches to approximate the XC energy. The two main approximations are Local Density Approximation (LDA) and various forms of Generalised Gradient

Approximation (GGA):

$$E_{XC}^{\mathrm{LDA}}[\rho(\vec{r})] = \int \rho(\vec{r})\epsilon_{XC}(\rho(\vec{r}))d\vec{r} \ , \tag{3.21}$$

$$E_{XC}^{\mathrm{GGA}}[\rho(\vec{r})] = \int \rho(\vec{r})\epsilon_{XC}(\rho(\vec{r}), \nabla\rho(\vec{r}))d\vec{r} \ . \tag{3.22}$$

$\epsilon_{XC} = \epsilon_X + \epsilon_C c$ is the exchange-correlation energy density. ϵ_X can be calculated rather accurately using quantum Monte Carlo simulations [102]. Nevertheless, the exchange energy is just an approximation and not an analytical value (available only in special cases such as a jellium model).

Out of those two, LDA overestimates the binding energy, whereas GGA underestimates it. When comparing all the energy terms in regard to their contribution, the XC energy contributes about 8 % with the correlation energy only contributing about 0.03 % [103]. However, this small part decides, e.g., if a bbc or an fcc structure is stable or at which position an adatom prefers to bond [103].

Now that all terms of the total energy are known, it is possible to search for its minimum. To do so, we need the XC potential defined as a functional derivative of XC energy:

$$V_{XC}[\rho(\vec{r})] = \frac{\partial E_{XC}[\rho(\vec{r})]}{\partial\rho(\vec{r})} \ . \tag{3.23}$$

This relation is used to define the Hamiltonian in the Kohn-Sham equation:

$$\hat{H}_{\mathrm{KS}}\phi_i = \epsilon_i\phi_i \ . \tag{3.24}$$

The K-S equation is solved self-consistently. From a starting electron density ρ_{start} the different potentials are calculated. With these potentials, the Kohn-Sham equation is solved, yielding a set of eigenvalues, e_i, and eigenfunctions, ϕ_i, of the K-S Hamilton operator. The new eigenfunctions allow to calculate a new electron density. If the electron density is the same as the one at the beginning of the cycle, we call it *converged* and the calculation process is stopped. Thereby, a self-consistent electron density of the crystal is found. This scheme is sketched in Fig. 3.1.

Once convergence is reached, the forces on the atoms are calculated using the Hellmann-Feynman theorem and their positions can be updated until an equilibrium is reached.

Pseudopotentials

For solids, a pseudopotential approach is often used instead of a real (all-electron) potential. The electrons of the material are separated into two groups, core electrons that are frozen

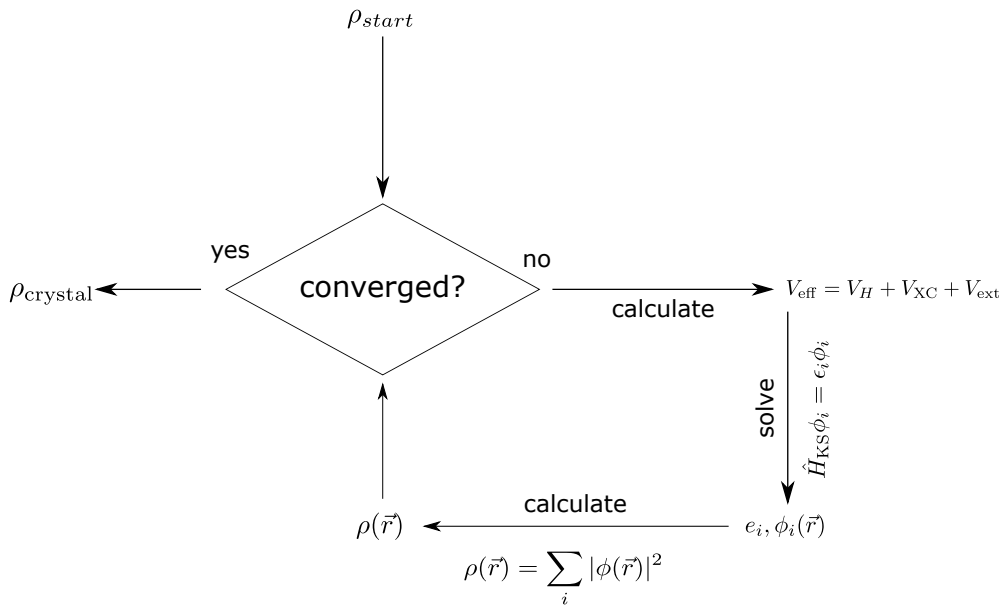

Figure 3.1: Scheme of a self-consistent cycle for calculating electron density. From a starting density, ρ_{start}, the eigenvalues and the eigenfunctions of the Kohn-Sham equation are calculated until the resulting electron density is obtained from the eigenfunctions converges.

together with nuclei into the pseudopotential, and the valence electrons which are described with pseudo wave functions. For a material with a periodic crystalline structure, the Bloch's theorem is conveniently employed. The theorem states that the solutions $\phi_{n,\vec{k}}$ of the K-S equation with a periodic potential can be chosen to have a form of a plane wave times a function with the lattice periodicity:

$$\phi_{n,\vec{k}}(\vec{r}) = e^{i\vec{k}\vec{r}}u_{n,\vec{k}}(\vec{r}), \qquad u_{n,\vec{k}}(\vec{r}+\vec{R}) = u_{n,\vec{k}}(\vec{r}) \tag{3.25}$$

for $\vec{R}$ being a lattice vector; n labels different solutions for the same $\vec{k}$. The periodic part can be further decomposed into a linear combination of basis set functions $\psi_j(\vec{r})$:

$$u_{n,\vec{k}}(\vec{r}) = \sum_j c_j^n(\vec{k})\psi_j(\vec{r}) \ , \tag{3.26}$$

where the coefficients $c_j^n(\vec{k})$ are to be estimated. The pseudopotential does not diverge at the atomic cores, where it is weaker than the real potential. The problem is the different requirements on the basis set for different parts of the crystal. For the nuclear region, atomic wave functions are ideal to fit the deep potential. For the interstitial region with only slight potential changes, plane waves are best suited.

Projector-augmented wave (PAW) potentials separate the core (ψ_{core}) and valence (ψ_{inter}) wave function into two parts and introduce an additional wave function which trims the overlapping part off (ψ_{net}):

$$\psi_{\mathrm{PAW}} = \psi_{\mathrm{inter}} + \psi_{\mathrm{core}} + \psi_{\mathrm{net}} \ . \tag{3.27}$$

To reduce the calculation size further, the problem can be transformed into the reciprocal space where it is easier to handle the wave functions due to the application of Bloch's theorem. In the reciprocal space, the first Brillouin zone (BZ) is the equivalent of the unit cell in the real space. With symmetry operations, it is possible to reduce the BZ further to an irreducible wedge of the Brillouin zone. This zone is then mapped by a discrete mesh of k-points, and all quantities can be obtained by integration, summation or extrapolation of values known at these points.

For an exact representation of a wave function, the plane wave basis set has to be infinite. However, the lower energy plane waves play the main role in describing the valence charge density. This allows for an introduction of a cut-off energy, E_{cut}, which defines the upper limit of the kinetic energy corresponding to the plane wave functions included in the calculations and reduces the number of wave functions to a finite amount.

Software tool

The DFT calculations in this thesis were performed with the Vienna Ab initio Simulation Package (VAPS), a widely used DFT code developed by Georg Kresse *et al.* at the University of Vienna [104, 105]. More in-depth explanations of the calculation details are given later on in the thesis.

3.2 Molecular Dynamics

Classical Molecular Dynamics (MD) is an atomistic simulation technique to solve many body problems for large numbers of atoms or molecules. The behaviour of the system is defined by its Hamiltonian ($\mathcal{H}$) Hamilton's equations of motion,

$$\frac{\partial \vec{p}}{\partial t} = \frac{\partial \mathcal{H}}{\partial \vec{r}_i} \ , \qquad \frac{\partial \vec{r}}{\partial t} = \frac{\partial \mathcal{H}}{\partial \vec{p}_i} \ . \tag{3.28}$$

are integrated to calculate the new positions of the atoms and the new velocities at these positions.

To perform MD simulations, one needs three ingredients: I) a way to describe the interactions between the atoms or molecules in the system. In many cases, pair-wise interactions are considered, which significantly reduce the computational effort. Many-body interactions are, however, more and more used since they allow for more accurate descriptions. II) an integrator which updates the positions and velocities of the particles from time t to $t+\delta t$. III)

a statistical ensemble which describes the thermodynamical properties such as temperature, pressure or the number of atoms. The microcanonical ensemble (NVE) is the most natural choice for MD simulations since, without any external potentials, the MD Hamiltonian is a conserved quantity.

With these three components, one can, in principle, model a system in an exact manner. However, for the practical numerical implementations, the results are only correct (precise) in the scope allowed by the parameters which enter the simulation. These parameters have to be tested against real-world results such as experimental data or first principles calculations.

The big advantage of classical MD compared to DFT is that it offers access to larger scales in both time and length. The length-scale can reach up to the µm domain, whereas the time can reach up to µs. This allows for applications in a wide range of topics, including mechanical properties in bulk materials, diffusion, or folding of proteins and drug delivery, to name a few. A number of different software packages are available to run MD simulations; all MD simulations in this thesis were performed with the LAMMPS code [106].

3.2.1 Particle Interaction

Regarding the component I related to the particle interactions, it is necessary to have a closer look at the Hamiltonian $\mathcal{H}$ that describes the system completely. For the convenience, we express it as composed of two terms, $\mathcal{H} = \mathcal{H}_1 + \mathcal{H}_0$.

$$\mathcal{H}_0 = \sum_{i=1}^{N} \frac{\vec{p}_i^2}{2m_i} + \sum_{i<j}^{N} u(\vec{r}_i, \vec{r}_j) + \sum_{i<j<k}^{N} u^{(3)}(\vec{r}_i, \vec{r}_j, \vec{r}_k) + \dots \tag{3.29}$$

where $\vec{p}_i$ is the momentum and m_i the mass of atom i. The pair-wise and three-particle interactions are described by u and $u^{(3)}$, respectively. $\mathcal{H}_1$ then contains any external forces or other time dependent effects. The forces on each particle can are then given by $\vec{F} = -\nabla U$, where U is the total potential energy corresponding to $\mathcal{H}$.

Different types of potentials are available to describe u and $u^{(3)}$. The most important distinction is between pair-wise potentials, such as the Lennard-Jones potential, and many-body potentials, such as the embedded atom method (EAM) and the modified embedded atom method (MEAM) potentials.

EAM are semi-empirical many-body potentials also reflecting the electron density to describe the atom interactions. They are suitable for describing metals and other bulk systems due to their capability to model the (delocalised) metallic bonding [107]. The modified

EAM (MEAM) adds a better description of the materials allowing for the possibility of also describing different structures (fcc, bcc, hex) using a single potential [108, 109].

In the framework of this thesis, a MEAM potential was used; hence only this type of interatomic potential is considered from here on.

3.2.2 Integrator

This part of the MD simulation code is responsible for updating the velocities and positions of the particles in the system. Again, there are several approaches to do so, such as Verlet or Runge-Kutta integration or Beeman's algorithm. A popular choice is the velocity-Verlet (VV) algorithm, which is the default option to describe the time evolution in the LAMMPS code. The algorithm is described by the following equations [110, 111]: First, calculate

$$\vec{v}(t + \frac{\delta t}{2}) = \vec{v}(t) + \frac{1}{2}\delta t \vec{a}(t) \tag{3.30}$$

then calculate the new positions at timestep $t + \delta t$.

$$\vec{r}(t + \delta t) = \vec{r}(t) + \vec{v}(t + \frac{1}{2}\delta t)\delta t \tag{3.31}$$

Calculate the forces on the atoms at the positions $r(t + \delta t)$ from the potential energy to get $\vec{a}(t + \delta t)$. And finally calculate the velocities at $t + \delta t$:

$$\vec{v}(t + \delta t) = \vec{v}(t + \frac{1}{2}\delta t) + \frac{1}{2}\vec{a}(t + \delta t)\delta t \tag{3.32}$$

At this step, the kinetic energy of the system (E_{kin}) can be calculated.

3.2.3 Ensembles and thermostats

Similar to the interatomic potentials and the integrator, there is again a range of ensembles to choose from for MD simulations. As stated before, the microcanonical ensemble (N,V,E) can be seen as the natural choice for MD simulations. If the system is not exposed to any time dependent external potential, the system's total energy remains constant. The microcanonical ensemble can be easily extended to the canonical ensemble with a constant number of particles, volume and temperature. Out of these three parameters, only temperature is

an intensive parameter, with the kinetic energy being its extensive counterpart. The kinetic energy is linked to the average temperature by:

$$E_{\text{kin}} = \frac{3}{2} N k_B T \ . \tag{3.33}$$

To keep the temperature at a fixed value during the simulation, different thermostats are available. Two commonly applied thermostats are the Langevin and Nosé–Hoover thermostats.

The Langevin thermostat is of stochastic nature. It introduces friction to the system by allowing all or a subset of the degrees of freedom to collide with *virtual* particles. The equation to calculate the force acting on a particle i changes to:

$$\frac{\partial \vec{p}_i}{\partial t} = \frac{\partial U}{\partial \vec{r}_i} - \gamma \vec{p}_i + \vec{F}^+ \ , \tag{3.34}$$

where γ is a friction constant and $\vec{F}^+$ a Gaussian random force. Large γ values result in increased thermal fluctuations, whereas $\gamma = 0$ would reduce the canonical ensemble to the microcanonical one.

In contrast, The Nosé–Hoover thermostat introduces additional degrees of freedom to the system. The idea is to describe the effect of an external system acting as a heat bath to one additional degree of freedom. The velocities of the particles in the system change due to the interaction between them and the heat bath. This can be described as a re-scaling of velocities. To do so, two sets of variables were introduced by Nosé: real and virtual. τ is introduced as a virtual time, while s is a scaling factor which results from $d\tau/dt = s$. For the real $(p_i, \vec{r}_i)$ and virtual $(\vec{\pi}_i, \vec{\rho}_i)$ variables have now the relation:

$$\vec{p}_i = \vec{\pi}_i, \qquad \vec{r}_i = \vec{\rho}_i. \tag{3.35}$$

With an introduction of the effective mass, M_s, the added degree of freedom can be connected to a momentum. These additions result in the following Hamiltonian expressed in virtual coordinates, $\vec{\rho}$:

$$\mathcal{H}^* = \sum_{i=1}^{N} \frac{\vec{\pi}_i^2}{2 m_i s^2} + U(\{\vec{\rho}_i\}) + \frac{\pi_s^2}{2 M_s} + g k_B T \ln s \ , \tag{3.36}$$

with g as the number of degrees of freedom ($g = 3N + 1$) in the system with N particles.

The equations for motion corresponding to this Hamiltonian can now be derived:

$$\frac{\partial \vec{\rho}_i}{\partial \tau} = \frac{\vec{\pi}_i}{s^2} \ , \tag{3.37}$$

$$\frac{\partial \vec{\pi}_i}{\partial \tau} = -\frac{\partial U(\{\vec{\rho}_i\})}{\partial \vec{\rho}_i} \ , \tag{3.38}$$

$$\frac{\partial s}{\partial \tau} = \frac{\pi_s}{M_s} \ , \tag{3.39}$$

$$\frac{\partial \pi_s}{\partial \tau} = \frac{1}{s^3} \sum_{i=1}^{N} \frac{\vec{\pi}_i^{\,2}}{m_i} - \frac{g k_B T}{s} \ . \tag{3.40}$$

The equations above are still in virtual coordinates but can be transformed back to real ones and simplified by introducing $\zeta = \partial s / \partial t = s p_s / M_s$ (p_s is the real momentum considering the connection to the heath bath). The following equations describe the Nosé–Hoover thermostat:

$$\frac{\partial \vec{r}_i}{\partial t} = \frac{\vec{p}_i}{m_i} \ , \tag{3.41}$$

$$\frac{\partial \vec{p}_i}{\partial t} = -\frac{\partial U(\{\vec{r}_i\})}{\partial \vec{r}_i} - \zeta \vec{r}_i \ , \tag{3.42}$$

$$\frac{\partial \ln s}{\partial t} = \zeta \ , \tag{3.43}$$

$$\frac{\partial \zeta}{\partial t} = \frac{1}{M_s} \left(\sum_{i=1}^{N} \frac{\vec{p}_i^{\,2}}{m_i} - g k_B T \right) \ . \tag{3.44}$$

3.3 Calculation Setups

3.3.1 Elastic Constants

The elasticity of a material is one of the most important properties when assessing its mechanical response. It describes the relation between the applied force and the resulting elastic deformation of the material. In the simple one dimensional case, this relation can be described by Hooke's law in the form of

$$\sigma = E \epsilon \ , \tag{3.45}$$

where E is the Young's modulus, and σ and ϵ are the stress and strain, respectively. To describe the relation between strains and stresses in three dimensions, the stiffness tensor $\mathbf{C} = (C_{ijkl})$ is used. $\mathbf{C}$ is a fourth rank tensor with 81 independent components. However, due to symmetry considerations, this can be reduced to 21 independent components at most.

The Voigt's notation maps a pair of indices to a single digit as:

$$11 \Rightarrow 1 \; ; \quad 22 \Rightarrow 2 \; ; \quad 33 \Rightarrow 3 \; ; \quad 23 \Rightarrow 4 \; ; \quad 13 \Rightarrow 5 \; ; \quad 12 \Rightarrow 6 \; . \tag{3.46}$$

With that, the stiffness tensor becomes a 6×6 matrix $\mathbf{C} = (C_{ij})$. Dependent on the crystallographic structure, the number of independent components can reduce further, with cubic materials exhibiting only three independent entires. Within the Voigt's notation, the relation between strain and stresses (the Hooke's law) can be written as follows:

$$\sigma_i = \sum_{j=1}^{6} C_{ij}\epsilon_j \; , \quad (i = 1, 2, \ldots, 6) \tag{3.47}$$

with σ_i and ϵ_j being the stress and strain tensors, respectively, again represented in the Voigt's notation as 6×1 vectors. Knowing both the strains and the corresponding stresses, it is easy to calculate $\mathbf{C}$.

DFT allows to calculate the stiffness tensor without any prior knowledge of the material. In the framework of this thesis, the C_{ij} was calculated with a so-called stress-strain method. The principle behind this method is to deform a previously relaxed cell by known strains, with the help of DFT, calculate corresponding stresses, and then solve Eq. (3.47). For simple symmetries, it is easy to find independent strains for the deformation. For more complex systems, it becomes much more involved. A simple solution was proposed by Yu, Zhu, and Ye [112]. They introduced a set of universal linear-independent coupling strains (ULICS) which significantly reduce the required amount of calculations for $\mathbf{C}$. Depending on the crystal system, as few as between one and six calculations are needed to get the full stiffness tensor.

As the theory is based on linear elasticity, whereas DFT, in general, and VASP, in particular, deliver non-linear results for large deformations, one has to be conscious about the magnitude of the applied strains. For the systems in this thesis $\epsilon_{\max} = 0.02$ proofed to be a robust choice.

Knowing the stiffness tensor, other mechanical properties can be calculated. Using Hill's scheme [113], polycrystalline Young's, bulk and shear moduli, as well as the Poisson's ratio can be determined. In some cases, it is desired to know Young's modulus E along a specific crystallographic direction. The directional Youngs's moduli were calculated using the equations derived in Ref. [114] for the cubic and orthorhombic systems:

$$\frac{1}{E^{\text{cub}}_{hkl}} = S_{11} - 2\left(S_{11} - S_{12} - \frac{1}{2}S_{44}\right)(\bar{h}^2\bar{k}^2 + \bar{k}^2\bar{l}^2 + \bar{h}^2\bar{l}^2) \; , \tag{3.48}$$

$$\frac{1}{E^{\text{ortho}}_{hkl}} = \bar{h}^4 S_{11} + 2\bar{h}^2\bar{k}^2 S_{12} + 2\bar{h}^2\bar{l}^2 S_{13} + \bar{k}^4 S_{22} + 2\bar{k}^2\bar{l}^2 S_{23} + \bar{l}^4 S_{33} + \bar{k}^2\bar{l}^2 S_{44} + \bar{h}^2\bar{l}^2 S_{55} + \bar{h}^2\bar{k}^2 S_{66} \; , \tag{3.49}$$

were $[\bar{h}\,\bar{k}\,\bar{l}]$ is a normalized vector in the crystallographic direction $[hkl]$.

To classify the TMNs into more brittle/ductile materials and with thereby more covalent/metallic bonding, Pugh [115] and Pettifor [116] introduced empirical indicators. These are the ratio between the shear and the bulk moduli, G/B, and the Cauchy pressure (P_{Cauchy}), which uses components of the stiffness tensor depending on the symmetry of the crystal. A material is categorized as ductile when $G/B \lessapprox 0.57$ and $P_{\text{Cauchy}} > 0$.

3.3.2 Tensile strength

To determine the tensile strength, supercell configurations were cleaved at specific planes of interest. This was done by introducing a vacuum with a gradually increasing thickness between two surfaces until the atoms in the so-created (rigid) blocks had no interaction, i.e. the total energy of the system was constant. The resulting energy curve Eq. (3.50) was fitted with the Rose's universal binding relation [117, 118]:

$$\Delta E(x) = E(x) - E_0 = E_c \left[1 - \left(1 + \frac{x}{l_{\text{crit}}}\right) \exp\left(-\frac{x}{l_{\text{crit}}}\right)\right] , \tag{3.50}$$

where x is the induced separation (vacuum) between the cleaved planes and E_0 is the ground state total energy. Cleavage energy, E_c, and critical length, l_{crit}, are two fitting parameters describing the cleavage properties to be determined. Deriving Eq. (3.50) yields the critical stress, σ_{crit}:

$$\sigma_{\text{crit}} = \left.\frac{dE(x)}{dx}\right|_{x=l_{\text{crit}}} = \frac{E_c}{l_{\text{crit}}} . \tag{3.51}$$

The cleavage energy is the energy required to separate the cell into two rigid blocks along the given plane. The critical length and stress are two values to determine the actual strength of the plane: the maximum stress the system can withstand in tension is σ_{crit}, and it corresponds to the separation l_c. To ensure no interaction of the interface with itself, a certain cell size is needed. Tests have shown that a supercell composed of 12 planes parallel to the cleavage plane was sufficient for the two surfaces to not interact with each other over the periodic boundary conditions. The maximum separation of 10Å was considered; the total energy changes for larger separations were negligible.

3.3.3 Fracture toughness

The fracture toughness, K_{IC}, was determined from the calculated cleavage energy, E_c, supercell cross-section area along the cleavage plane, A, and the directional Young's modulus,

E_{hkl}, in a direction perpendicular to the cleavage plane, following the formula from [119]:

$$K_{\mathrm{IC}} = \sqrt{4\frac{E_c}{A}E_{hkl}} \ . \tag{3.52}$$

In the original formula, the term E_c/A was represented by surface energy, γ. Tests on the present systems showed that γ can be well approximated by the cleavage energy, which is, in fact, unrelaxed surface energy

Chapter 4

Influence of point defects in MoAlN

This section is partly based on the publication *Structure, stress, and mechanical properties of Mo-Al-N thin films deposited by dc reactive magnetron cosputtering: Role of point defects* [33]. The experimental values used in the discussion were published in that reference if not indicated otherwise.

4.1 Motivation

Compared to the other brittle transition metal nitrides, i.e. TiN and ZrN, MoNx shows a higher ductility. It was also shown both experimentally [86, 87] and theoretically [84, 85] that alloying TMNs with Mo increases their ductile character further. This is a result of shear elastic softening while maintaining high strength. The alloying leads to a higher electronic population of the $4d$ electronic orbitals of TMs, explaining the increase in toughness[85, 120]. Stoichiometric MoN is both mechanically and dynamically unstable in the cubic B1 structure [88, 121, 122]. At the same time, the Mo-N phase diagram exhibits a lot of different phases over the whole composition range. This sparked interest in how the phase stability depends on the deposition parameters as well as on the influence of point defects. Epitaxial cubic MoNx films are interesting due to their optical properties for ultraviolet applications with resistivity as low as $250\,\mu\Omega$cm and a negative and near-zero real permittivity [89]. Finally, MoN is also a good candidate for tribological coatings with a low friction coefficient and wear rate at moderate temperatures below 500 °C [91, 92]. The addition of Al, similar to the Ti-Al-N and Cr-Al-N systems, has been speculated to have beneficial effects on oxidation behaviour and mechanical properties. Especially improving the oxidation resistance is of great interest as MoN coatings deteriorate at elevated temperatures by the formation of volatile molybdenum oxides.

The ternary MoAlN system could not be synthesised by powder metallurgy methods, thus concluding that Mo has no solubility in AlN [93]. In the thermodynamically far form the equilibrium environment of PVD depositions, it was, however, possible to synthesise $Mo_xAl_{1-x}N_y$ solid solutions [32]. It was shown that the addition of Al stabilises the cubic phase for Al fractions of up to $x = 0.57$. Above that, the formation of the wurtzite phase is more favourable, along with a significant decrease in both hardness and elastic modulus [32]. The reported mechanical properties vary a lot leaving a not yet clear understanding of the actual cause. Yang *et. al* [94] report decrease in hardness form 30 GPa at $x = 0$ down to under 20 GPa at $x = 0.33$. A similar trend was found by Xu *et. al* [123] with a hardness of 28.9 GPa for $x = 0$ and 12.3 GPa for $x = 0.33$ the decrease is even bigger. Klimashin *et. al* [32] on the other hand reported an increase in hardness and a plateau at around 37 GPa for $x = 0.20$–0.55. For the Young's modulus, the results differ from each other as well. For example, the reported elastic modulus for $x = 0.35$ ranges from 450 [32] to 280 GPa [94]. All these coatings were reported to have the cubic B1 phase. They differ, however, in their nitrogen content, y, which points towards the significant effect vacancies on both the metal and nitrogen sublattice can have on the mechanical properties.

The study presented in this section aims to investigate the influence of point defects in cubic $Mo_xAl_{1-x}N_y$.

4.2 Simulation details

To determine how point defects alter the properties in cubic $Mo_xAl_{1-x}N_y$, DFT simulations were performed with the help of the Vienna *Ab initio* Simulation Package [104]. The used pseudo-potentials utilised the projector augmented wave method [105] and the generalised gradient approximation for the exchange and correlation effects. The simulations were run with a cutoff energy of 600 eV and a $9 \times 9 \times 9$ k-point mesh and were considered converged for total energy changes smaller than 10^{-5} eV and changes in force smaller than 0.01 eV/Å.

The cells for the simulations were created to be as close as possible to the observed N/Me ratio in the experiments [33]. Besides the perfect systems without any defects, different compositions with vacancies[1] on either the metal (V_{Me}) or on the nitrogen sublattice (V_N) were looked into. Additionally, MoAlN with Schottky defects, Frenkel pairs and N atoms at the metal sublattice (N anti-sites, N_{Me}) were also considered. Finally, Mo_2N was also calculated. The supercells for the calculations were $2 \times 2 \times 2$ expanded rock-salt unit cells

[1] "V" in this section stands for vacancy and should not be confused with vanadium.

totalling to 64 atoms. The metal sublattice was populated with Mo and Al atoms for the different compositions with the special quasi-random structure (SQS) approach [124]. The vacancies on both sublattices were created with this method as well, in which the metal vacancies were distributed between Al and Mo sites to get the desired composition. A consequence of the size of the cell (64 atoms) is that the composition could only be changed by 1.56 % for the whole cell and 3.12 % for each sublattice. This was a trade-off between the accuracy in composition and computational resources. The exact composition for each cell can be seen in Tab. 4.1.

For all the compositions, the relaxed lattice parameters were calculated from the relaxed volume assuming a cubic lattice. The full stiffness tensor (C_{ij}) was calculated with the strain/stress method. To do so, the cells were deformed by a small amount using strains represented in the Voight's notation by six linearly independent vectors and their negatives, and the resulting stresses were calculated. Employing the Hooke's law, $\sigma_i = C_{ij}\epsilon_j$, the matrix of stiffness constants, C_{ij}, can be determined with the applied strain and the calculated stresses. The resulting stiffness tensor was then projected onto the cubic symmetry of the system, following Moakher and Norris [125]. The polycrystalline Young's modulus was calculated following the Voigt-Reuss homogenization. More details can be found in Sec. 3.3.1.

4.3 Results

4.3.1 Phase stability

To determine which composition and defect type are the most favourable form a thermodynamics standpoint, the energy of formation, E_f, was calculated:

$$E_f = \frac{E_{\text{bulk}} - \sum_i E_i n_i}{\sum_i n_i} \ , \tag{4.1}$$

with E_{bulk} as the ground state energy of the SQS cell, E_i as the energy of constituent i with n_i atoms in the SQS cell. E_f for all calculated cells is plotted in Fig. 4.1. Perfect (blue dots) MoN in the rock-salt structure is the only composition with a positive E_f with $0.214\,\text{eV/at}$. From a thermodynamics standpoint, nitrogen vacancies are required to stabilise the cubic phase. Introducing 10 % V_N (orange squares) decreases the energy of formation down to $-0.079\,\text{eV/at}$. For low Al concentrations, E_f differs only marginally from the perfect systems when vacancies on the metal or nitrogen sublattice are considered. At around a 10 % of Al on the metal sublattice, the defect-free system with $E_f = -0.168\,\text{eV/at}$, V_N with $-0.173\,\text{eV/at}$, V_{Me} (green squares) with $-0.169\,\text{eV/at}$ and Schottky defect (purple

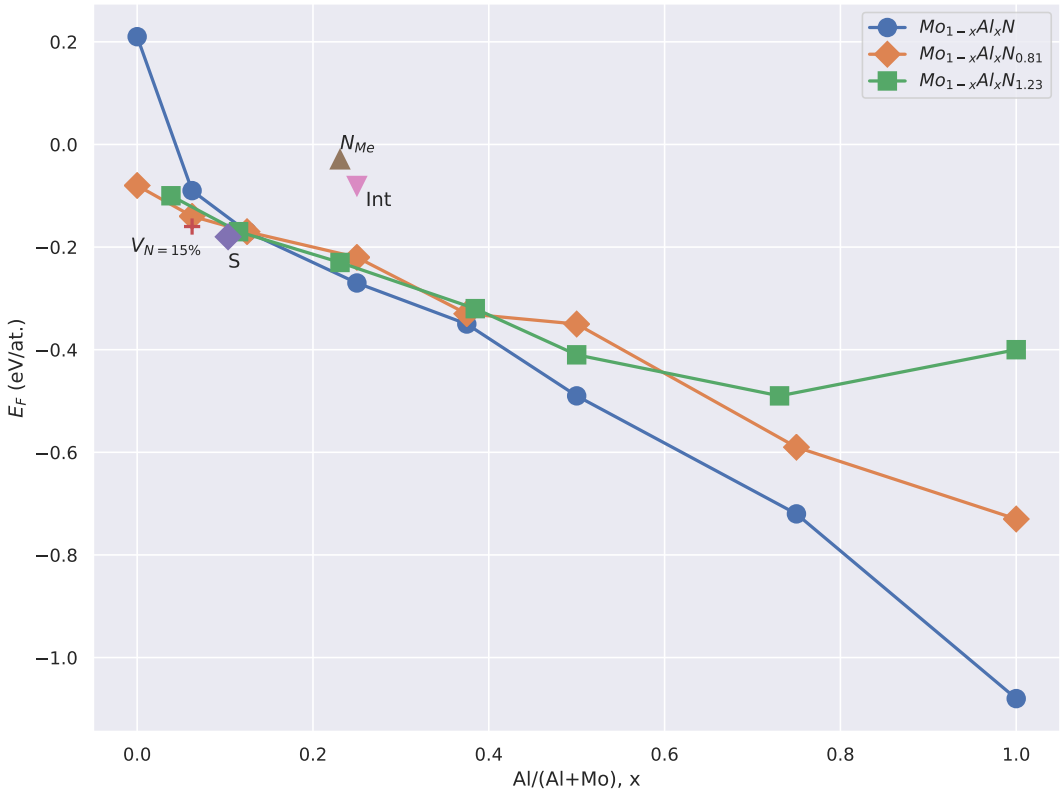

Figure 4.1: Energy of formation, E_F, for the different $Mo_xAl_{1-x}N_y$ systems as a function of the Al concentration on the metal sublattice. The perfect systems (blue circles) and the ones with 10 % vacancies (V_N ($y < 1$): orange square; V_{Me} ($y > 1$): green squares) cover the whole composition range. The systems (15 % N vacancies (red cross), Schottky defect (purple square), interstitial N (pink triangle) and N at the metal sublattice (brown triangle)) with other defected types were considered only for compositions close to those experimentally studied.

square) with $-0.179\,\mathrm{eV/at}$ exhibit all similar values. Increasing the Al concentration further, the addition of vacancies becomes unfavourable. Regarding the V_N and V_{Me}, the nitrogen vacancies are slightly less favourable for $x = 0.2 - 0.5$ for even higher Al concentrations, the Al vacancies at the metal sublattice become less favourable compared to the nitrogen vacancies. From $x = 0.5$ on, however, the perfect systems are clearly favoured. A higher V_N concentration ($x = 0.15$) (red cross) and Schottky defect with $x = 0.0625$ and 0.103 respectively result in slightly lower E_f values compared to other systems with similar Al concentrations. The other two systems with N at the metal sublattice (brown triangle) and as an interstitial (pink triangle) both show elevated energies of formations than the other systems at those Al concentrations.

4.3.2 Structural properties

The introduction of vacancies and the changing composition have both a noticeable influence on the lattice constant, a. With increasing Al content, the lattice constant reduces from 4.357 Å for c-MoN to 4.069 Å for AlN. As expected, the introduction of vacancies decreases the lattice constant. Over most of the composition range, metal vacancies result in slightly smaller lattice constants compared to nitrogen vacancies. For $x \approx 0.75$ this behaviour reverts as binary AlN nitrogen vacancies result in a bigger lattice constant than the perfect systems. This is consistent with previous results [126]. Looking at the other defects, the interstitial nitrogen ($x = 0.25$) stands out with the largest lattice constant of all calculations with 4.456 Å. Increasing the amount of N vacancies lowers a further to 4.264 Å for $x = 0.06$, Schottky defects are comparable to the metal vacancies; nitrogen vacancies yield the lattice constants between the values for systems with metal vacancies and the defect-free systems.

The mass density, ρ, is plotted in Fig. 4.3. The mass density decreases with increasing Al content, from 8.82 g/cm^3 for cubic MoN down to 4.04 g/cm^3 for cubic AlN; between these compositions, the trend for $Mo_xAl_{1-x}N_y$ is linear. The introduction of nitrogen vacancies (light element) has a much smaller impact compared with metal ones, as can be seen in Fig. 4.3.

4.3.3 Elastic Constants

The elastic constants of the different systems are represented by the polycrystalline Young's modulus, E, in Fig. 4.4 and C_{44} in Fig. 4.5. Compared to the energy of formation and the lattice constants, the behaviour with increasing Al fraction is not as uniform. Looking at the Young's modulus in Fig. ,4.4 one can see that the perfect MoN is missing from the graph. As the positive E_f suggests chemical instability (Fig. 4.1), and the calculated stiffness tensor delivers a negative Young's modulus, pointing to its mechanical instability. The presence of nitrogen vacancies in the cubic MoN, however, results in its stabilisation and a Young's modulus of 217 GPa. Increasing the Al content to $\approx 5\,\%$ the Young's modulus becomes positive, 7 GPa, even for the defect-free $Mo_xAl_{1-x}N_y$, but still pointing towards an unstable configuration. The introduction of vacancies for these compositions increases the Young's modulus to around 100 GPa. Going towards slightly higher Al concentrations ($x \approx$12 %) increases E to 280–310 GPa almost independent from defect concentrations. For systems with either V_N or V_{Me}, the Young's modulus stays within this range. The defect-free systems show a different behaviour: from Al concentrations of $x = 0.12 - 0.25$ they stay at

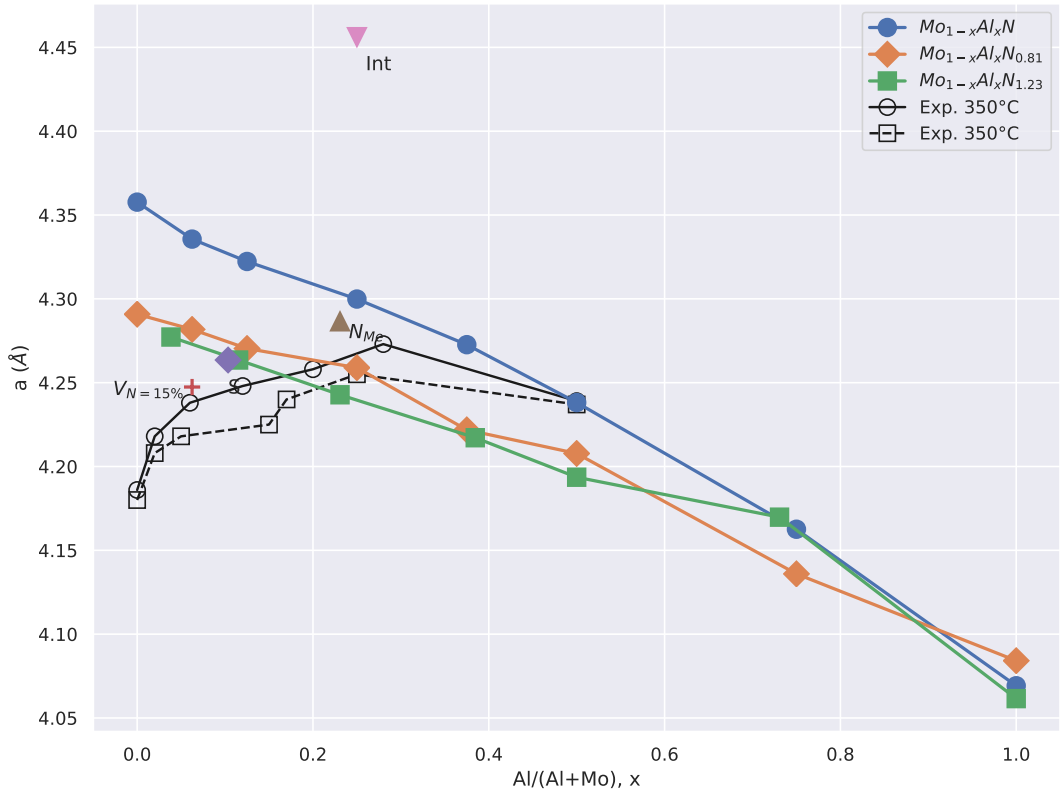

Figure 4.2: Lattice constant, a, for the different $Mo_xAl_{1-x}N_y$ systems over the Al concentration. The perfect systems (blue circles) and the ones with 10 % vacancies (V_N ($y < 1$): orange square; V_{Me} ($y > 1$): green squares) cover the whole composition range. The other defected systems (15 % N vacancies (red cross), Schottky defect (purple square), interstitial N (pink triangle) and N at the metal sublattice (brown triangle)) are around the experimentally observed compositions. The black curves are experimental results with deposition temperatures of 350 °C (circles) and 400 °C [33].

300 GPa, then dropping to 200 GPa (probably and outlier) before increasing to 400 GPa. In the Al-rich region, the defect-free systems exhibit clearly higher Young's moduli than the defected ones. For the binary cubic AlN, E rises to 500 GPa, whereas AlN with V_N and V_{Me} show much smaller values with 280 and 227 GPa, respectively.

The shear elastic constant C_{44} exhibits similar behaviour as the polycrystalline Young's modulus. For low concentrations of Al, the values are small, with even $C_{44} < 50$ GPa. Increasing Al content leads to a sharp increase of C_{44} to around 100 GPa for the defect-free systems as well as those with V_N, V_{Me} and Schottky defects. The defect-free $Mo_xAl_{1-x}N_y$ shows an increase to 308 GPa for the binary AlN. The systems with vacancies exhibit rising values as well up to 153 GPa at $x = 0.75$, followed by a slight decrease for cubic AlN.

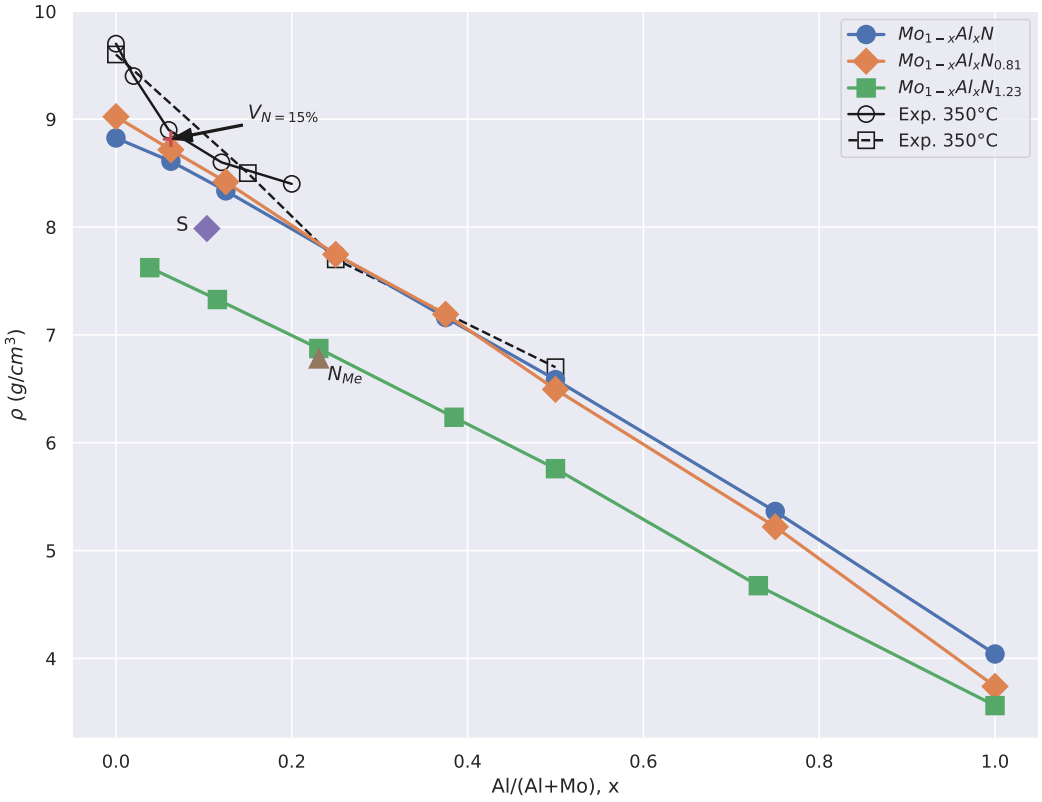

Figure 4.3: Mass density, ρ, for the different $Mo_xAl_{1-x}N_y$ systems over the Al concentration. The perfect systems (blue circles) and the ones with 10 % vacancies (V_N ($y < 1$): orange square; V_{Me} ($y > 1$): green squares) cover the whole composition range. The other defected systems (15 % N vacancies (red cross), Schottky defect (purple square), interstitial N (pink triangle) and N at the metal sublattice (brown triangle)) are around the experimentally observed compositions. The black curves are experimental results with deposition temperatures of 350 °C (circles) and 400 °C [33].

4.3.4 Values

Table 4.1 summarises the calculated values for all compositions.

4.4 Discussion and comparison with experiments

4.4.1 Phase stability and structure

The addition of Al in the cubic MoN lowers the energy of formation and therefore stabilises the lattice thermodynamically. This trend was also reported by Klimashin, Euchner, and Mayrhofer [32]. In contrast to their results, however, we discovered that the type of defect

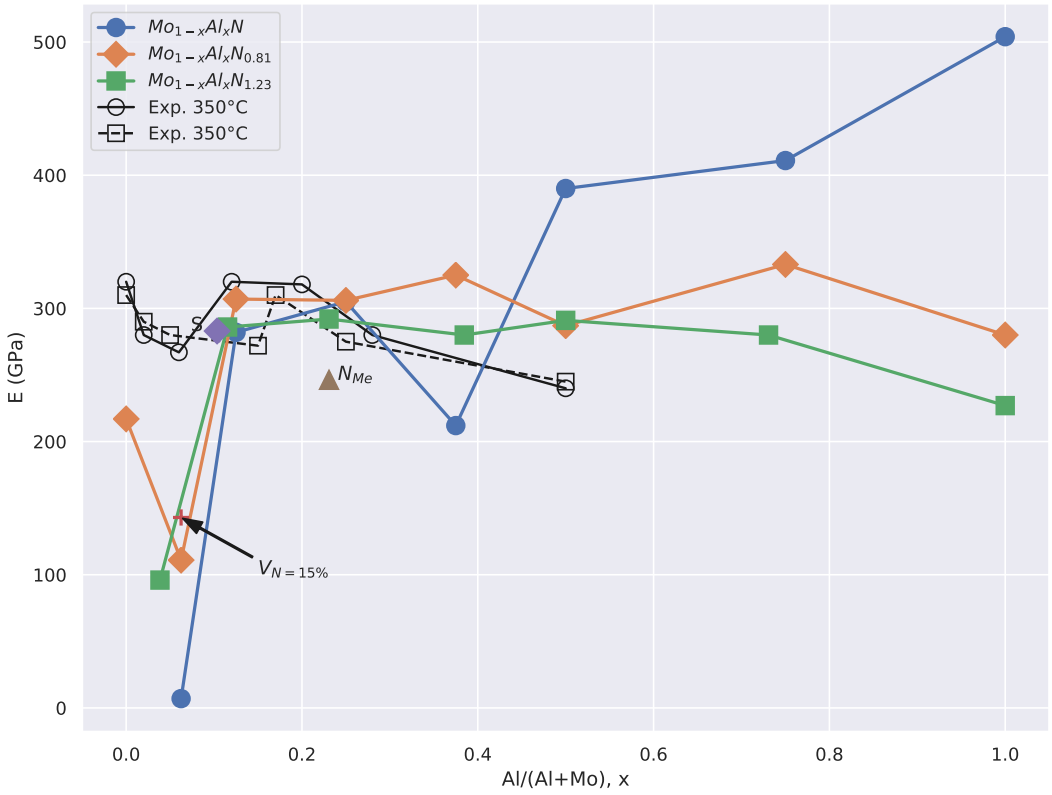

Figure 4.4: Young's modulus, E, for the different $Mo_xAl_{1-x}N_y$ systems as a function of the Al concentration. The perfect systems (blue circles) and the ones with 10 % vacancies (V_N ($y < 1$): orange square; V_{Me} ($y > 1$): green squares) cover the whole composition range. The other defected systems (15 % N vacancies (red cross), Schottky defect (purple square), interstitial N (pink triangle) and N at the metal sublattice (brown triangle)) are around the experimentally observed compositions. The black curves are experimental results with deposition temperatures of 350 °C (circles) and 400 °C [33].

which is preferred depends on x. In the experiments, the binary MoN had a composition of $Mo_{56}N_{44}$ and $Mo_{57}N_{43}$, which hints at the presents of N vacancies or metal interstitials. This fits well with the calculations predicting that vacancies are needed to thermodynamically stabilise the cubic MoN. Increasing Al content, the N content is found to increase from understochiometric ($y \sim 0.75$) to overstochiometric ($y \sim 1.38$) at $x = 21\,\%$. At this composition, the calculations predict the formation of V_{Me} over V_N as well, although they are preferred only slightly and are not as favourable as a the defect-free system itself. Both interstitial nitrogen and nitrogen on the metal sublattice are thermodynamically not favourable compared to N vacancies or the defect-free system.

The calculated lattice constants for MoN are much larger than what was found in the experiments, as one can see from Fig. 4.2. The experimental values actually fit much better to

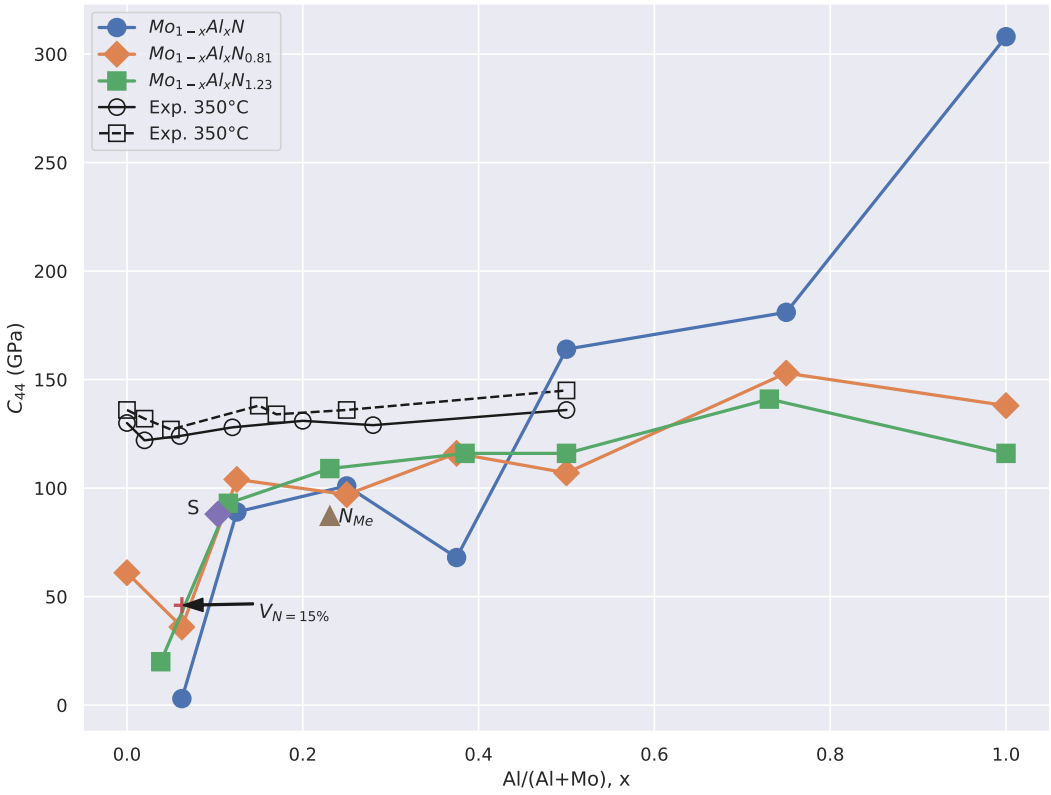

Figure 4.5: Shear elastic constant, C_{44} for the different $Mo_xAl_{1-x}N_y$ systems over the Al concentration. The perfect systems (blue circles) and the ones with 10 % vacancies (V_N ($y < 1$): orange square; V_{Me} ($y > 1$): green squares) cover the whole composition range. The other defected systems are around the experimentally observed compositions. The black curves are experimental results with deposition temperatures of 350 °C (circles) and 400 °C [33].

γ-Mo_2N and cubic MoN_2 [127], which points to the presence of either of these phases. For a higher Al content, the calculated lattice constants become comparable to the experimental ones. For the coatings with the highest Al concentration ($x = 50\,\%$), the experimentally determined lattice constant of $a = 4.238\,\text{Å}$ well agrees with the predicted value for the the defect-free system.

Regarding the mass density of the calculated cells with the experimental compositions, experiments show slightly higher values for low Al concentrations. This would support the presence of V_N for the lower concentrations, the calculations show slightly higher values compared to the defect-free system as well. For $x \gtrapprox 25\,\%$ the experimental and the calculated mass density of the defect-free systems follow closely together. This agrees with the findings that less defective $Mo_xAl_{1-x}N_y$ is experimentally synthesised for higher Al content.

x	E_f (eV/at.)	a (Å)	E (GPa)	C_{44} (GPa)	Mo (1)	Al (1)	N (1)	ρ (g/cm^3)	v_T (m/s)
0.000	0.214	4.357	–	–	4	0	4	8.82	–
0.000	−0.079	4.290	217.0	61.0	32	0	26	9.02	2599
0.038	−0.096	4.277	96.0	20.0	25	1	32	7.62	1619
0.062	−0.086	4.335	7.0	3.0	30	2	32	8.60	590
0.062	−0.135	4.281	111.0	36.0	30	2	26	8.71	2032
0.062	−0.164	4.247	143.0	46.0	30	2	23	8.81	2284
0.103	−0.179	4.263	283.0	88.0	26	3	29	7.98	3319
0.125	−0.173	4.270	307.0	104.0	28	4	26	8.41	3514
0.125	−0.168	4.322	282.0	89.0	28	4	32	8.33	3267
0.115	−0.169	4.263	286.0	93.0	23	3	32	7.32	3562
0.230	−0.032	4.286	246.0	87.0	20	6	35	6.77	3582
0.230	−0.226	4.242	292.0	109.0	20	6	32	6.87	3982
0.250	−0.083	4.456	–	–	24	8	38	7.15	–
0.250	−0.268	4.299	305.0	101.0	24	8	32	7.74	3610
0.250	−0.216	4.258	306.0	97.0	24	8	26	7.74	3538
0.375	−0.327	4.221	325.0	116.0	20	12	26	7.19	4016
0.375	−0.354	4.272	212.0	68.0	20	12	32	7.16	3081
0.384	−0.320	4.217	280.0	116.0	16	10	32	6.23	4312
0.500	−0.352	4.207	287.0	107.0	16	16	26	6.49	4058
0.500	−0.413	4.193	291.0	116.0	13	13	32	5.75	4487
0.500	−0.486	4.238	390.0	164.0	16	16	32	6.58	4990
0.750	−0.592	4.135	333.0	153.0	8	24	26	5.22	5413
0.730	−0.493	4.169	280.0	141.0	7	19	32	4.67	5492
0.750	−0.719	4.162	411.0	181.0	8	24	32	5.36	5809
1.000	−0.404	4.061	227.0	116.0	0	26	32	3.56	5706
1.000	−0.729	4.084	280.0	138.0	0	32	26	3.74	6074
1.000	−1.083	4.069	504.0	308.0	0	4	4	4.04	8730

Table 4.1: Selected calculated values for all considered compositions. The base amount of atoms in each cell is 64 except for the first and last line, in which it is 8 and cell with N interstitials (70). If no elastic constants could be determined, they and the values stemming from them were omitted (–).

4.4.2 Mechanical Properties

The calculated Young's modulus and C_{44} differ a lot from the experimental values for $x \leq 6\,\%$. Above this value, the experiments and simulations come to an agreement. In both cases, a slight continuous increase of C_{44} was found up to $x = 50\,\%$. Our predictions compare well also to DFT studies on γ-Mo_2N ,[127] which show a decrease for all elastic constants when V_N and V_{Me} are introduced. The behaviour of C_{44} in our calculations is more complex and dependent on the Al concentration. Similarly, complicated behaviour was also reported for vanadium-aluminium nitrides, $V_{1-x}Al_xN_y$ [128].

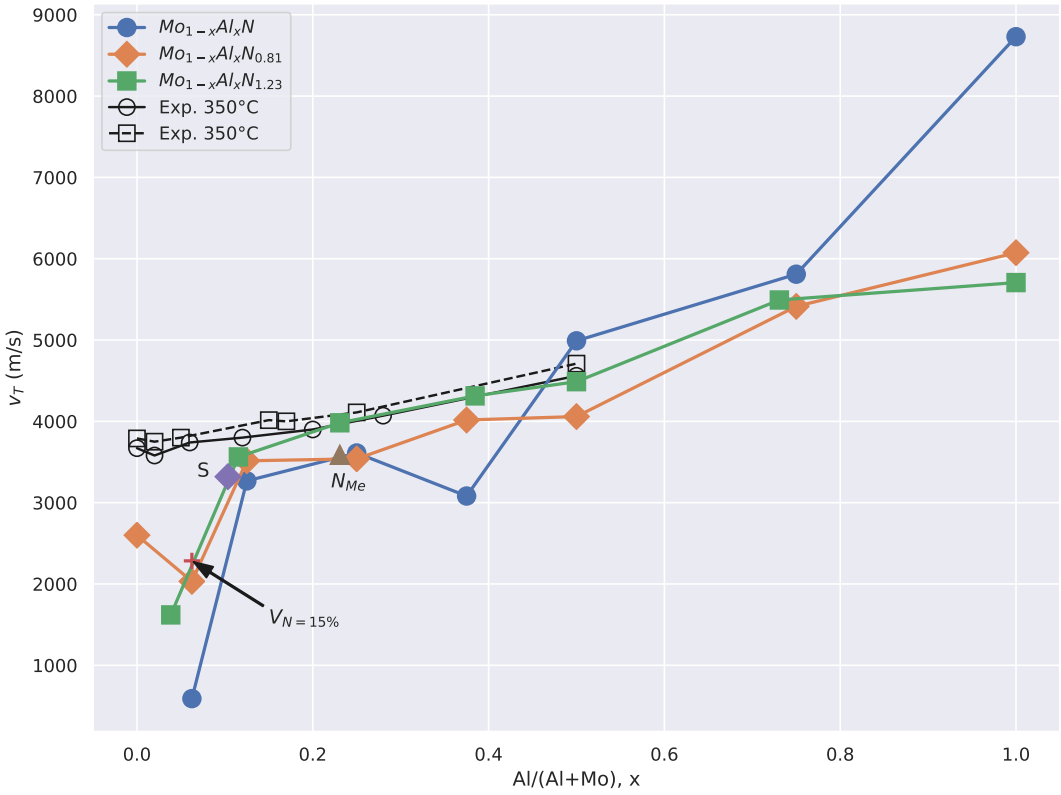

Figure 4.6: Transversal sound velocity, v_T, for the different $Mo_xAl_{1-x}N_y$ systems over the Al concentration. The perfect systems (blue circles) and the ones with 10 % vacancies (V_N ($y < 1$): orange square; V_{Me} ($y > 1$): green squares) cover the whole composition range. The other defected systems are around the experimentally observed compositions. The black curves are experimental results with deposition temperatures of 350 °C (circles) and 400 °C [33].

The transverse sound velocity, v_T, was calculated as

$$v_T = (C_{44}/\rho)^{1/2} \ . \tag{4.2}$$

As demonstrated in Fig. 4.6, the calculated values show the same continuous increase as the experiments. The absolute numerical agreement is much better than for C_{44} and E.

Finally, the influence of vacancies and the Al concentration on ductility can be examined. Fig. 4.7 shows the ratio between bulk modulus, B, and shear modulus, G, plotted against the Cauchy pressure ($c = C_{12} - C_{44}$). Pugh's [115] and Pettifor's [116] criteria serve as a basis for discussing brittle ($G/B > 0.57$ and $c < 0$) and ductile ($G/B \leq 0.57$ and $c > 0$ response [129]. One can see that the MoN_y structures fall in the ductile regime, as was already stated in the introduction. The incorporation of up to 50 % Al does not have a big

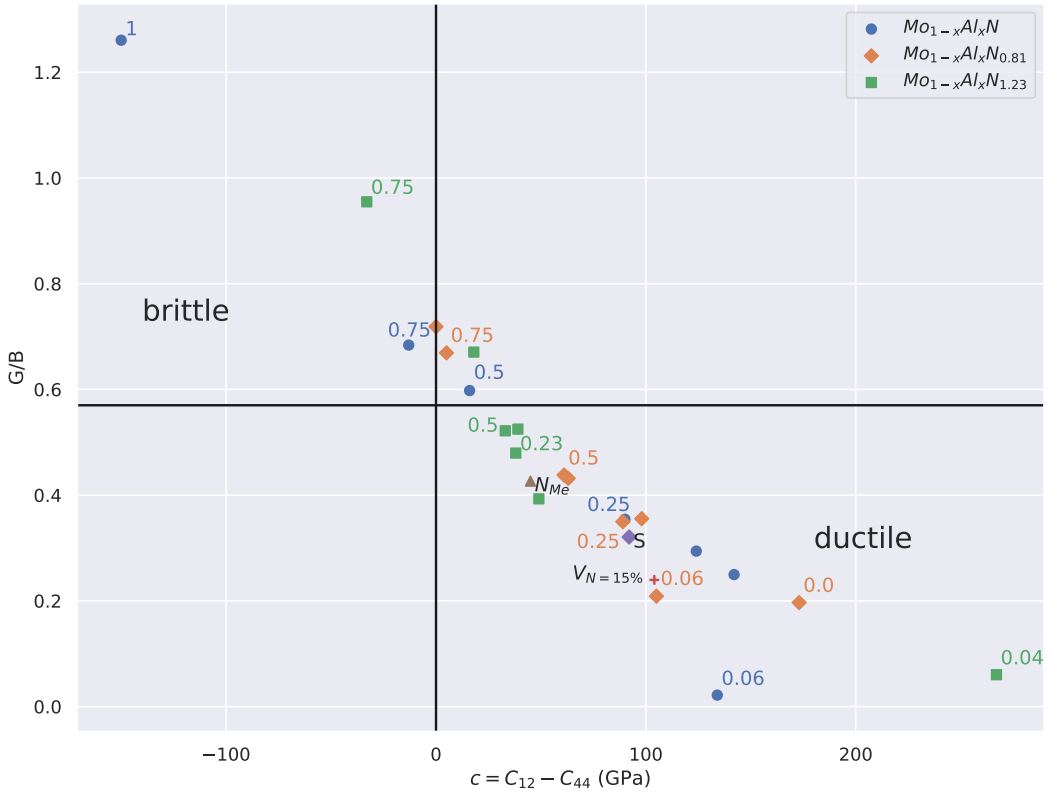

Figure 4.7: G/B over Cauchy pressure, c, for the different $Mo_xAl_{1-x}N_y$ systems over the Al concentration. The perfect systems (blue circles) and the ones with 10 % vacancies (V_N ($y < 1$): orange square; V_{Me} ($y > 1$): green squares) cover the whole composition range.

influence on ductility. Further, one can conclude that the presents of V_N is more beneficial to keep the ductile behaviour of $Mo_xAl_{1-x}N_y$ systems than the metal vacancies.

4.5 Summary

The performed simulations were coupled with experiments to study the influence of Al and vacancies on the structure and mechanical properties of cubic Mo-Al-N. The results show that point defects play a key role in the compositional trends of lattice constants, Young's modulus and C_{44}. This holds particularly true for nitrogen vacancies for Al fractions below $x = 0.12$ and for metal vacancies with at $x \gtrapprox 0.12$. This partly explains the widespread of the E (223–450 GPa) found in the literature. From simulations, it was found that nitrogen vacancies are favoured for Al content of $x \lessapprox 0.12$ and contribute to a large increase of E and C_{44}. The comparison of experimental and theoretical E suggest the preference of metal

vacancies for $x \gtrapprox 0.12$.

In summary, the simulated results, together with the experimental findings, show the importance of point defects for the stabilisation and the elastic properties of the metastable cubic MoN systems. The results of this study help in knowledge-based design directed towards increasing strength of Mo-Al-N coatings and may inspire works on stabilisation of other Me-A-N coatings by tuning both the elemental composition and the point-defects in the system.

Chapter 5

Impact of magnetism on mechanical properties of superlattices

This section is based on the publication L. Löfler, R. Hahn, P.H. Mayrhofer, M. Bartosik, D. Holec: *Mechanical properties of CrN-based superlattices: Impact of magnetism* Acta Mater., 218 (2021) 117095 [130].

5.1 Motivation

The work in this chapter aims to explore mechanical properties and magnetism in superlattice coatings containing CrN with the help of quantum mechanical calculations. Tensile strength of nitride superlattices has been previously studied theoretically for TiN/VN [118, 131], AlN/VN [131], TiN/AlN [131, 132] (including the wurtzite phase of AlN), and MoN/TaN [20, 133] (including the impact of point defects). These studies also included a discussion on the structural and mechanical properties of superlattices. A systematic exploration of nitride-based superlattices was presented by Wang *et al.* [134].

None of the above mentioned theoretical papers, however, dealt with CrN, which is another commonly used system for hard coatings. It exhibits structural compatibility with TiN (and B1 cubic AlN), good hardness and oxidation resistance. CrN exhibits different magnetic configurations depending on temperature: it has an anti-ferromagnetic (afm) order with (110) double-planes of alternating spins in its ground state [135], enforcing the structure to be orthorhombic with lattice constants of 5.71, 2.99 and 4.07 Å. Above the Neél temperature of $\approx 280\,\mathrm{K}$, CrN undergoes a phase transformation to a paramagnetic (pm) state with the rock-salt B1 structure [136]. Zhou *et al.* [136] also suggested that an artificial ferromagnetic (fm) state of CrN is a reasonable approximation to computationally very expensive pm-CrN

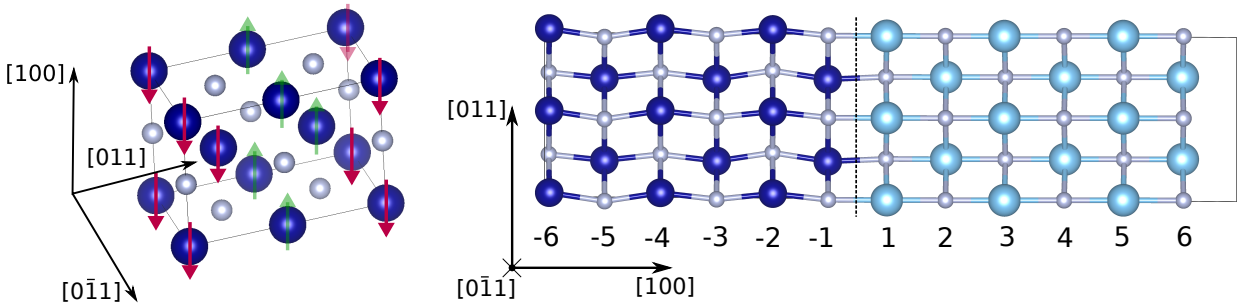

Figure 5.1: The left-hand panel shows anti-ferromagnetic CrN in its orthorhombic cell, the spin distribution on the Cr atoms is indicated by the coloured arrows. The right-hand panel shows one of the used supercells, in this case, CrN/TiN, with a 100 interface. The numbers below indicate the plane-indexing used throughout this chapter. The structures were visualised using the VESTA3 software [140].

regarding its mechanical properties. Structural properties of CrN/AlN superlattices were reported by Zhang *et al.* [55], whereas Friák *et al.* [27] focused on elastic properties; both works showed a favourable comparison with experiment.

However, a systematic study on the interface-related properties in CrN-based superlattices are missing. In this work, we investigate the influence of different interface orientations and magnetic states on the mechanical properties , including the tensile strength and fracture toughness of CrN/AlN and CrN/TiN superlattices. All three nitrides (CrN, AlN, TiN) are already commonly used in coatings, making them prime candidates for pairing them together. TiN and pm-CrN are naturally crystallising in the cubic B1 rock-salt structure, AlN has a B4 hexagonal wurtzite structure in its ground state. In combination with other nitrides, however, AlN can be stabilised in the B1 structure in multilayers for thin layer thicknesses [26, 28, 38]. The cubic lattice parameters are $a_{\mathrm{AlN}} = 4.07$Å [137], $a_{\mathrm{CrN}} = 4.14$Å [138] and $a_{\mathrm{TiN}} = 4.24$Å [139], hence probing also different in-plane stress states in CrN in the superlattices: tensile in CrN/TiN and compressive in CrN/AlN. Our primary tool was the Density Functional Theory (DFT), and the theoretical results have been corroborated by experimental results and are discussed in the light of existing literature data.

5.2 Simulation details

The DFT calculations were performed using the Vienna Ab initio Simulation Package (VASP), applying a plane wave basis set [104, 105] using the generalized gradient approximation (GGA) for the exchange-correction effects. The cutoff energy was set to 600 eV, and an 11 x 21 x 3 k-point mesh was used. As the convergence criteria, an energy difference of 10^{-5} eV (per simulation box) and atomic forces less than 10^{-4}eV/Å were employed. The starting magnetic moments of the Cr atoms were set to 2.3 μ_{b}. The paramagnetic (pm) state of CrN

was modelled with a Special Quasi-random Structure (SQS) [141], distributing the positive and negative spins in a $2 \times 2 \times 2$ supercell. The afm nature of CrN changes the unit cell from cubic to orthorhombic as described in [135]. Consequently, the sides of the cell differ not only structurally but also magnetically. The used unit cell can be seen in Fig. 5.1. For the paramagnetic superlattice, $2 \times 2 \times 4$ supercells containing 160 atoms were used, whereas $1 \times 1 \times 4$ supercells were used for the afm and fm configurations. The fm state of CrN was considered as a computationally cheaper alternative for representing the pm cells [136], which is to be tested for its applicability in superlattice configurations.

To calculate the elastic response of the different structures, the strain-stress method was used [112], see Sec. 3.3.1. The resulting general stiffness tensor was subsequently projected onto the crystal symmetry of the structure following the formalism described by Moakher and Norris [125]. The Voigt-Reuss scheme as implemented in SC-EMA [142, 143] was used for homogenization to get values comparable with experiments. In addition, stiffness constants of the binary nitrides were used to approximate those of the superlattices with the approach of Grimsditsch and Nizzoli (G&N) [144].

The tensile strength was calculated using the rigid displacement method as described in Sec. 3.3.2. To ensure no interaction of the interface with itself, a certain cell size is needed. Tests have shown that a supercell composed of 12 planes parallel to the cleavage plane is sufficient for the two surfaces to not interact with each other over the periodic boundary conditions. Consequently, each material is represented by six planes. The maximum separation of 10Å was considered; the total energy changes for larger separations were negligible.

The fracture toughness (K_{IC}) was determined according to the methodology in Sec. 3.3.3. Using the Voigt's notation for C_{ij} being the matrix representation of the elastic constants tensor c_{ijkl}, the compliance matrix, S_{ij} is calculated as inverse of the C_{ij} matrix. The directional Youngs's moduli were calculated using the equations derived in Ref. [114] for cubic and orthorhombic systems:

$$\frac{1}{E^{\mathrm{cub}}_{hkl}} = S_{11} - 2\left(S_{11} - S_{12} - \frac{1}{2}S_{44}\right)\left(\bar{h}^2\bar{k}^2 + \bar{k}^2\bar{l}^2 + \bar{h}^2\bar{l}^2\right) , \tag{5.1}$$

$$\frac{1}{E^{\mathrm{ortho}}_{hkl}} = \bar{h}^4 S_{11} + 2\bar{h}^2\bar{k}^2 S_{12} + 2\bar{h}^2\bar{l}^2 S_{13} + \bar{k}^4 S_{22} + 2\bar{k}^2\bar{l}^2 S_{23} + \bar{l}^4 S_{33} + \bar{k}^2\bar{l}^2 S_{44} + \bar{h}^2\bar{l}^2 S_{55} + \bar{h}^2\bar{k}^2 S_{66} , \tag{5.2}$$

were $[\bar{h}\,\bar{k}\,\bar{l}]$ is a normalized vector in the crystallographic direction $[hkl]$.

Finally, Table 5.1 gives an overview of the different superlattice configurations considered in this chapter, namely, superlattices with interfaces parallel to crystallographic (100) and

(011) planes. The former yields afm planes (in CrN) with a total spin $0\,\mu_B$ parallel to the interface, whereas the latter case leads to magnetically polarised planes.

5.3 Results

5.3.1 Structural characterisation and magnetic behaviour

The superlattice configurations result in the atoms to slightly change their positions, and consequently, also other properties change compared with the parent binary bulk phases. Figures 5.2 and 5.3 show the mean of the absolute values of magnetic moments (per metal atom, blue solid lines), the mean magnetic moments (per metal atom, blue dash-dotted lines) for each individual plane, as well as the interplanar spacing between the planes (green lines). Clearly, AlN and TiN exhibit no magnetism (only negligibly small magnetic moments near the interfaces with adjacent CrN). The mean absolute magnetic moments per Cr atom in the CrN planes are $\approx 2.30\,\mu_B$ and $\approx 2.35\,\mu_B$ for (100) and (110) interfaces, respectively, which is somewhat lower than what was reported for bulk pm-CrN ($2.48\,\mu_B$ in Ref. [136]) and a little higher than the values calculated here for the bulk afm-CrN ($2.27\,\mu_B$). Moreover, the magnitude of the magnetic moment seems to be independent of the chosen magnetic ordering, either fm or afm. N atoms in CrN layers do show negligibly small magnetic moments of $\approx 0.05\,\mu_B$, and are hence considered also non-magnetic. It is worth noting that while the magnitude of the magnetic moment is almost constant in the case of the afm configuration, it shows a depth profile for the fm ordering. This behaviour is the same for TiN/CrN as well as for AlN/CrN, and also for different interface orientations (100) in Fig. 5.2 and (011) in Fig. 5.3. However, while the magnetic moment is higher at the (100) interface than in the middle of the fm-CrN layer, the (110) interface has a slightly lower magnetic moment than the bulk of the fm-CrN layer. The profile of the magnitude of magnetic moments is

material	interface	magnetic conf. (CrN)
CrN/TiN	(100)	pm ($\perp$), fm, afm
CrN/TiN	(011)	fm, afm
CrN/AlN	(100)	fm, afm
CrN/AlN	(011)	fm, afm

Table 5.1: Overview of the different systems investigated in this study. CrN was paired either with TiN or AlN and investigated for different interface orientations as well as magnetic configurations. $\perp$ indicates that only the direction perpendicular to the interface was investigated.

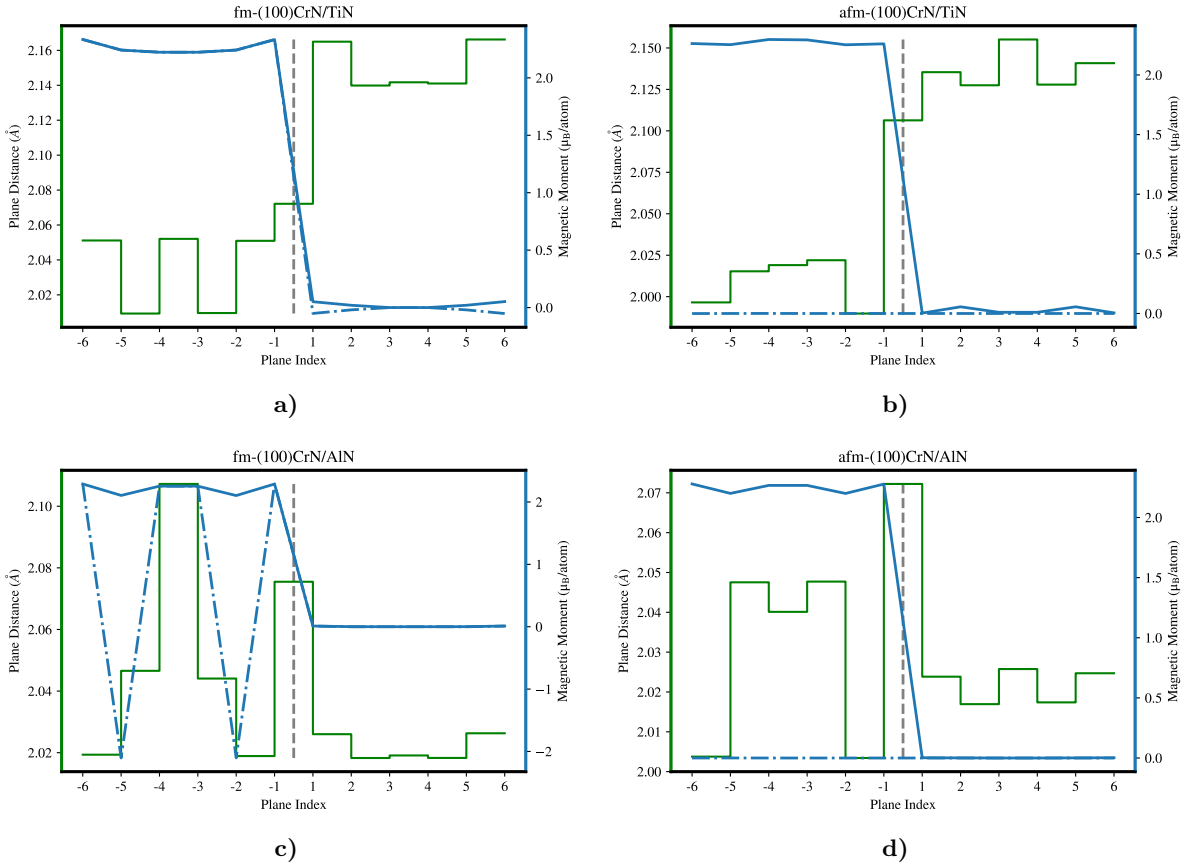

Figure 5.2: Mean values of the absolute values of the magnetic moments in each plane (per metal atom, blue solid lines), the mean magnetic moment in a plane (per atom, dash-dotted blue line) and interplanar spacing (green lines) for superlattices with (100) interfaces: a) fm-CrN/TiN, b) afm-CrN/TiN, c) fm-CrN/AlN, d) afm-CrN/AlN.

symmetrical with respect to the centre of the CrN layers. The mean absolute value of the magnetic moment of Cr atoms is slightly higher in the fm state than in the afm state in the case of (100) interfaces, while the opposite holds for the (011) orientation. Nevertheless, the differences are below $0.04\,\mu_B$/at., a value which is negligibly small. Therefore we can conclude that the magnitude of the magnetic moment is independent of the actual magnetic ordering (fm or afm).

An interesting behaviour is nonetheless revealed when inspecting the mean value of the magnetic moment (dash-dotted lines in Figs. 5.2 and 5.3). Considering the spin arrangement in (100) planes (right-hand panel of Fig. 5.1), the mean value of the spin in the (100) plane is 0 in the case of the afm state and non-zero in the case of the fm state where both Cr atoms are symmetry-equivalent and thus yield the same spin. While the fm-(100)CrN/TiN shows the expected behaviour, in which all spins have the same orientation, the mean value of the (100) planes in fm-(100)CrN/AlN alternates between positive and negative values.

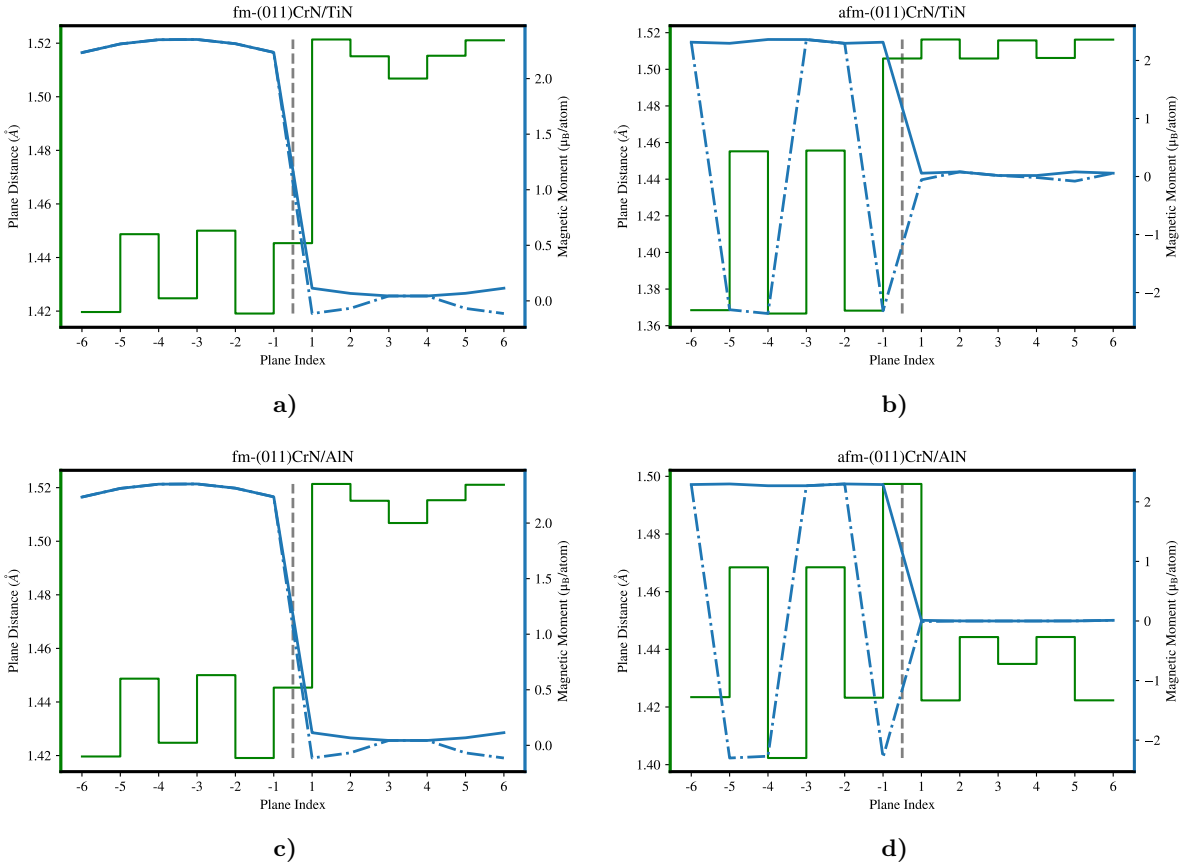

Figure 5.3: Mean values of the absolute values of magnetic moments in each plane (per metal atom, blue solid lines), mean magnetic moment in plane (per atom, dash-dotted blue line) and interplanar spacing (green lines) for superlattices with (011) interfaces: a) fm-CrN/TiN, b) afm-CrN/TiN, c) fm-CrN/AlN, d) afm-CrN/AlN.

This result implies that the final magnetic state consists of (100) planes with alternating spins, i.e. some kind of an anti-ferromagnetic order. We note that this afm-(100) state is different from the CrN afm ground state with double-(011) planes. The meta-stability of the false afm state (denoted as fm in this chapter) is further underlined by the formation energy being 24 meV/at. higher than the (100)CrN/AlN superlattice with the true afm state (Fig. 5.2d).

In conclusion, the presence of the (100) interface between CrN and AlN induces a perturbation to the system strong enough to lead to a spontaneous flipping of the magnetic moment on some Cr atoms and hence inducing a false afm configuration. We speculate that this is driven by CrN trying to rearranging its magnetic order to be "closer" to its true afm ground state [135].

The interplanar spacings follow a similar picture as the magnetic moments in the sense that they exhibit symmetrical behaviour in most of the cases. The small asymmetry of afm-

(100)CrN/TiN can be attributed to numerical errors, the values of interplanar distances between CrN (100) planes number 2 and 3, and 4 and 5 are identical within the accuracy of our calculations (Fig. 5.2a). In general, the oscillations of interplanar spacings are smaller in AlN than in CrN, in agreement with experimental observations and explicit calculations on pm-CrN/AlN [55]. Such behaviour was explained by the different extend of Friedel oscillations in metallic and semiconducting system [55, 131, 132]. Regarding the CrN/TiN superlattices, the variations of the interplanar spacings are more pronounced in the case of CrN than TiN, and in the case of (011) than (100) interfaces. Importantly, the minima of the interplanar distances often correlate with the adjacent planes being spin-polarized and having opposite mean spins (e.g., fm-(100)CrN/AlN or afm-(001)CrN/TiN or afm-(001)CrN/AlN). This points towards a strong magnetic interaction and an interplay between the magnetic and structural properties of CrN.

Overall we can conclude that, despite some differences depending on the actual magnetic order, the *structural properties* of both magnetic configurations (nominally fm and afm) for both systems and each of the both interface orientations are rather similar.

5.3.2 Elastic constants

The stiffness constants calculated using the strain/stress method are listed in Tab. 5.2 for the different configurations. For the superlattices, the axis '1' is perpendicular to the interface, i.e., C_{11} relates $\sigma_{\perp\perp}$ and $\epsilon_{\perp\perp}$, and $\perp$= [100] and $\perp$= [011] directions in the conventional cubic reference frame in the case of (100) and (011) interfaces, respectively. The other two axes '2' and '3' coincide with the (orthogonal) sides of the simulation box. The orthorhombic nature of the afm-CrN is reflected in the orthorhombic symmetry[1] of the stiffness tensor, while those of AlN and TiN keep the cubic symmetry. The results for TiN and AlN are in agreement with with other studies [145, 146]; also C_{ij} of afm-CrN are similar to the ones reported by Zhou *et al.* [136], Mayrhofer *et al.* [147]. We note that C_{ij} of afm-CrN is also expressed in the coordination frame connected with the underlying conventional cubic system of the rock-salt structure; elastic constants in the orthorhombic system (as used, e.g. by [136], see Fig. 5.1a) correspond to those listed for the (100) and (0$\bar{1}$1) interfaces.

There is a principal difference between the CrN/TiN and CrN/AlN superlattices, stemming from the elastic symmetry of its binary compounds, as visualised using directional Young's modulus E_{hkl}. While TiN exhibits the maximum of E_{hkl} for the [100] direction (and minimum for the [111] direction), AlN shows exactly the opposite trend. The three $\langle 100 \rangle$ directions

[1]The apparent tetragonal symmetry of the stiffness tensor matrix is due to rounding the values to GPa.

System	C_{11}	C_{22}	C_{33}	C_{44}	C_{55}	C_{66}	C_{12}	C_{13}	C_{23}
					(GPa)				
conventional coordinate system 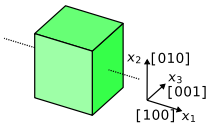									
TiN	608	-	-	159	-	-	143	-	-
afm-CrN	481	560	560	137	99	99	118	118	145
AlN	416	-	-	308	-	-	158	-	-
(100) interface 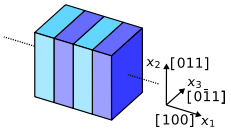									
TiN	608	534	534	232	159	159	143	143	215
afm-CrN/TiN	564	483	428	188	114	138	131	144	171
afm-CrN/TiN G&N	537	540	484	220	112	132	129	129	215
fm-CrN/TiN	450	430	430	177	111	111	256	256	191
pm-CrN/TiN	540	478	478	191	121	121	266	266	209
afm-CrN	481	546	434	207	86	113	118	118	215
afm-CrN/AlN	474	549	486	162	151	175	141	149	98
afm-CrN/AlN G&N	447	570	514	168	134	165	140	140	97
fm-CrN/AlN	440	480	480	133	112	112	307	307	106
AlN	416	596	596	129	308	308	158	158	-21
(011) interface 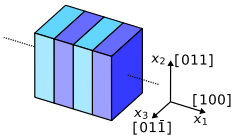									
TiN	534	534	608	159	159	232	215	143	143
afm-CrN/TiN	467	518	535	136	104	205	190	144	153
afm-CrN/TiN G&N	540	484	544	123	132	219	215	131	131
fm-CrN/TiN	426	476	490	125	111	166	175	126	135
afm-CrN	546	434	481	86	113	207	215	118	118
afm-CrN/AlN	505	511	477	202	96	148	118	146	146
afm-CrN/AlN G&N	502	544	448	210	134	159	116	135	143
fm-CrN/AlN	427	412	334	181	134	127	113	326	139
AlN	596	596	416	308	308	129	-21	158	158

Table 5.2: Stiffness constants of the supercells for (100) and (110) interface as well as those of relevant binary nitrides. They were calculated using the strain/stress method. In addition, the stiffness constants of the binaries were used to calculate the elastic constants of the supercells using the Grimsditsch and Nizzoli approach (marked with G&N in the table).

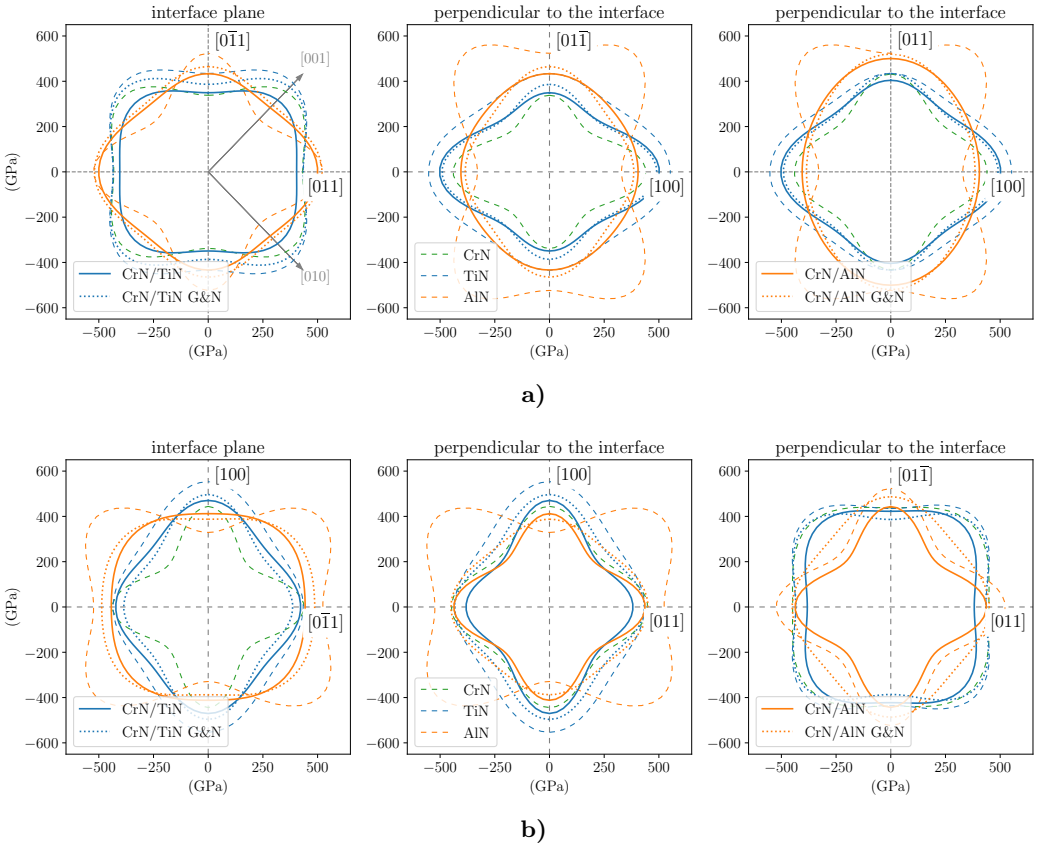

Figure 5.4: Directional Young's modulus for the three main projection planes of afm-CrN/TiN and afm-CrN/AlN with (a) (100) and (b) (011) interfaces.

are not all equivalent in the case of CrN due to the anti-ferromagnetic order, however, also , in this case, the $E_{[100]}$ is larger than $E_{[0\bar{1}1]}$ and $E_{[011]}$, i.e. shows similar behaviour as TiN. These trends are visualised by the dashed lines in Fig. 5.4 for all three binaries and different projections.

The directional dependence of a superlattice-effective Young's modulus is shown with the thick solid lines. It turns out, that afm-CrN/TiN elastic response is mostly "in-between" of afm-CrN and TiN (the solid blue line is between the blue and green dashed lines in Fig. 5.4). This holds true for both interface orientations. However, it is worthwhile noting some exceptions to the above described behaviour. Notably, the [011] direction (i.e. the direction along which Cr planes with constant spin are alternating, see Fig. 5.1) in the SL is softer than any of the binary TiN (435 GPa) and afm-CrN (432 GPa). Moreover, in the case of (100) interface, the SL [010] and [001] directions (diagonal directions in the panel labelled "interface plane") are also clearly softer than both binary constituents. Nevertheless, there are no directions in which the SL Young's modulus outperforms both TiN and afm-CrN at the same time.

The situation is slightly more complicated for the case of afm-CrN/AlN SL due to different elastic response. Consequently, the SL Young's modulus is much more isotropic (less directional) than each of the constituents, as well as in comparison to the afm-CrN/TiN SL (compare the solid orange and blue lines for the (100) interface).

Lastly, the Grimsditsch&Nizzoli's approach [148] was applied to estimate the elastic constants of the superlattices, in addition to the explicit strain/stress method. The G&N method is very fast since it works only with the elastic constants of the constituents as inputs. The resulting values are provided in Tab. 5.2 along with the properly rotated C_{ij} of binaries and respective SLs. Despite the fact that the individual C_{ij} from the G&N and the stress-strain method differ by up to $\approx 20\%$ in extreme cases (see, e.g., C_{23} for afm-CrN/TiN), the resulting directional dependence of Young's modulus seems to satisfactorily agree (compare dotted and solid lines in Fig. 5.4). The agreement is particularly good for the afm-(100)CrN/AlN system, which has been already reported before: Friák *et al.* [27] showed not only excellent agreement between the two theoretical approaches, but also a quantitative agreement with indentation modulus of highly orientated coherent CrN/AlN superlattices. Nevertheless, the present comparison also points out deficiencies of the G&N method. Firstly, the resulting $E_{hkl}^{\mathrm{G\&N}}$ is always "in-between" the values of the constituting binaries. Therefore, it fails to reproduce the SL softening in some directions (e.g., [010] or [001] of afm-CrN/TiN), or slightly superior stiffness of the SL compared with the constituents (e.g., direction tilted by $\approx 20^\circ$ away from the [100] direction towards the $[0\bar{1}1]$ direction in the afm-(100)CrN/AlN SL, see Fig. 5.4a, middle panel). We conclude that such effects stem from the interfaces, which are explicitly included in the stress-strain method but ignored by the G&N method. Consequently, the G&N method should be applied with great care in the case of small bilayer period (high density of interfaces).

Young's modulus of different magnetic orderings in CrN/TiN and CrN/AlN SLs are plotted in Fig. 5.5 for both considered configurations. The motivation for this investigation was a suggestive conclusion of Ref. [136], which showed that fm-CrN is dynamically stable and hence may serve as an approximation of cubic pm-CrN. Comparing the elastic properties visualised using the Young's modulus, several conclusions can be drawn. Firstly, the pm-CrN/TiN is elastically "between" afm-CrN/TiN and fm-CrN/TiN (100)-orientated SL, with the afm (fm) configuration being systematically stiffer (softer) than the pm state. Secondly, the fm-CrN/AlN configuration shows significant anisotropy, which could point towards reduced mechanical stability (very small values of Young's modulus in some directions). This is the case, particularly for the (011) interface in which the fm state was stabilised (see Fig. 5.3c). Nevertheless, since fm-CrN/TiN does not exhibit any significant elastic insta-

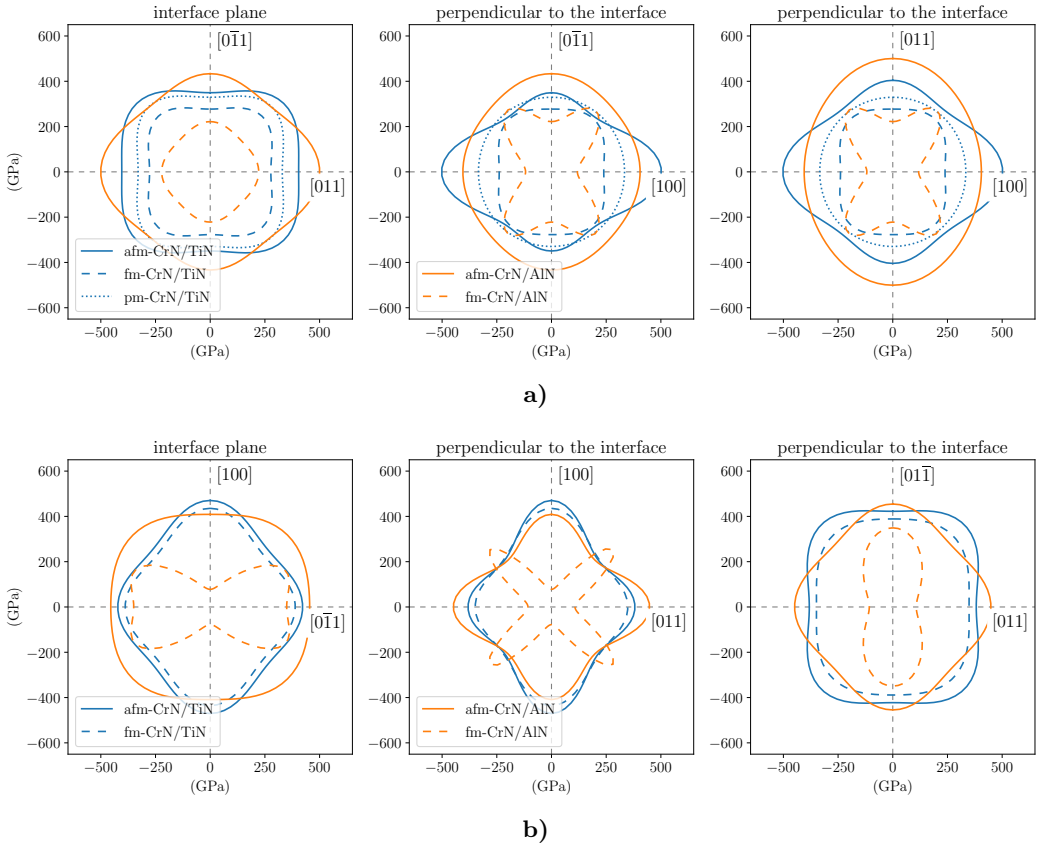

Figure 5.5: Directional Young's modulus for the three main projection planes of CrN/TiN and CrN/AlN with (a) (100) and (b) (011) interfaces. Various magnetic states were considered: solid, dashed and dotted lines represent afm-, fm-, and pm-CrN configuration, respectively.

bility, it is not purely the magnetic state but rather the magnetic state together with the interface, which results in high elastic anisotropy. Finally, we note that a decent agreement between C_{ij} of pm-CrN and fm-CrN was obtained only in the case of the GGA+U approach; the pure GGA exchange-correlation potential yielded largely different tensor of elastic stiffnesses [136].

5.3.3 Interface strength

The strength of the interfaces was derived from the cleavage calculations. These were performed for the cleavage plane perpendicular to the considered interface (see Fig. 5.6d), as well as along the interface planes, considering different interface orientations. In addition to the interface itself, other planes in the superlattice parallel to the interface were also considered. Examples of the excess energy $\Delta E(x)$ (fitted with Eq. 3.50) and corresponding applied stress $\sigma(x) = d\Delta E(x)/dx$ as a function of the separation x are shown in Figs. 5.6a–c for the case of cleaving perpendicular to the interface for different magnetic states of CrN in

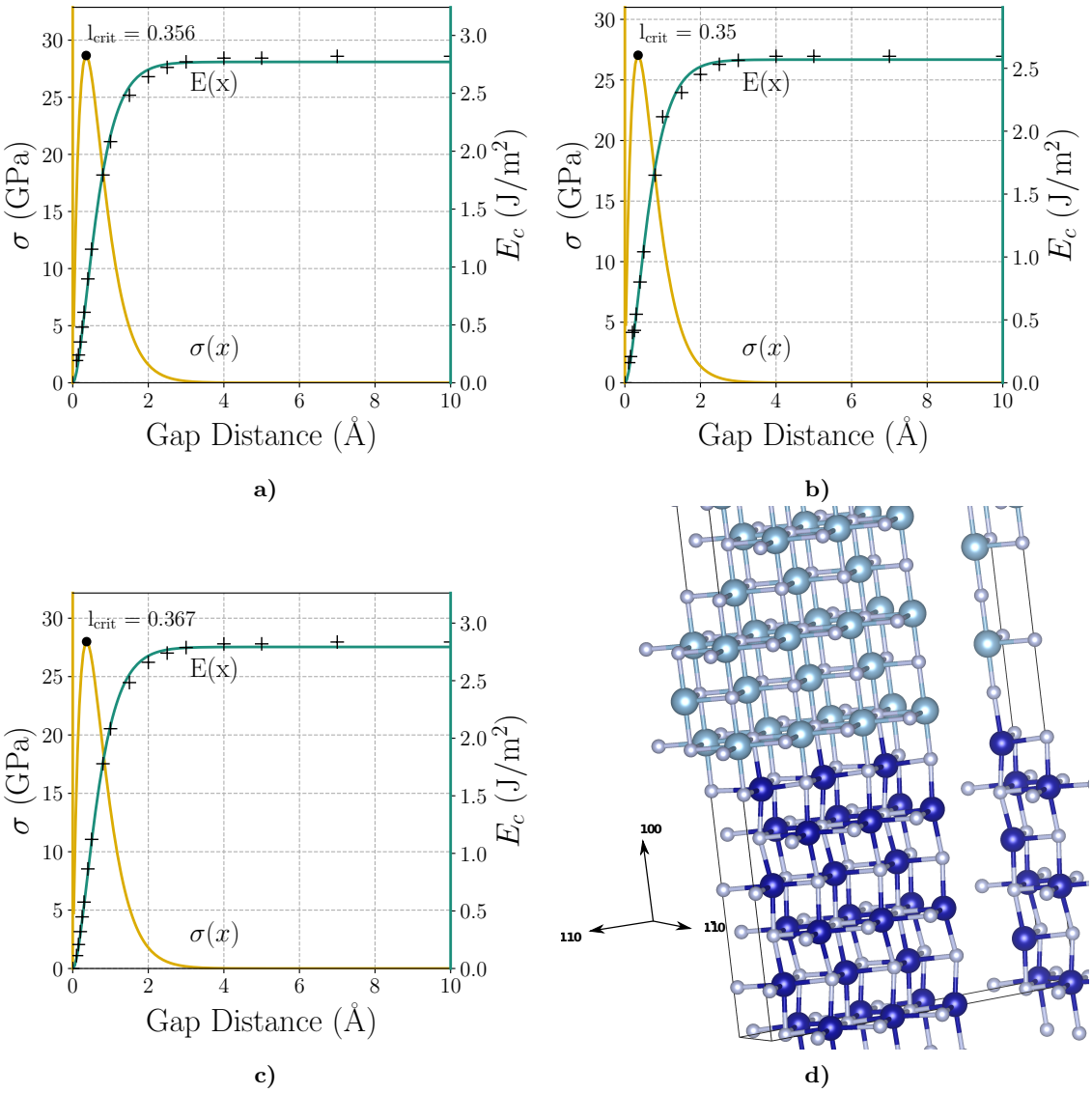

Figure 5.6: Critical stresses and cleavage energies for cleavages perpendicular to the interface (100) along the [010] direction of (a) afm (b) fm (100) and (c) pm CrN/TiN. In contrast to the cleavage in the interface direction, where differences between the different magnetic states occur perpendicular to the interface, the magnetic configuration does not play any significant role. (d) Shows the CrN/TiN supercell cleaved perpendicular to the (100) interface along the $(1\bar{1}0)$ plane. The structures were visualised using the VESTA3 software [140].

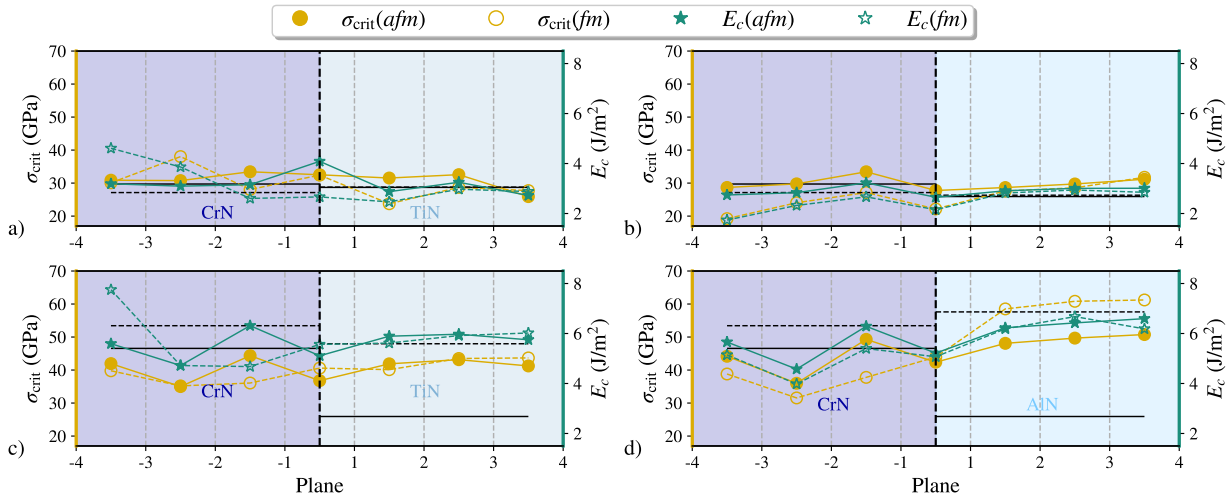

Figure 5.7: The critical stress (yellow) and the cleavage energy (green) for different material systems and interface orientations. The full and dashed lines correspond to the afm and fm magnetic state of CrN. (a) shows the values for CrN/TiN with the (100) interface, (b) CrN/AlN with the (100) interface, (c) CrN/TiN with the (011) interface and (d) CrN/AlN with the (011) interface. The horizontal lines denote the critical stress (solid lines) and the cleavage energy (dashed lines) for bulk afm-CrN and TiN or AlN as reference values for the SLs.

(100)-orientated CrN/TiN.

Several observations can be made. Firstly, the cleavage energies are reasonably converged for the maximum separation of 10Å. Secondly, the fit with Eq. 3.50 approximates the data well. Finally, there is no significant difference between afm-CrN/TiN (Fig. 5.6a), fm-CrN/TiN (Fig. 5.6b) and the pm-CrN/TiN (Fig. 5.6c) configurations. All three cases yield comparable parameters, E_c (cleavage energy for a large separation), critical length l_c and critical stress σ_{crit}.

The results for various cleavage planes and materials systems cleaved parallel to the interface are summarised in Fig. 5.7. The figures show both the cleavage energy E_c and the critical stress σ_{crit} for the interface and all parallel planes in the supercell, for fm and afm state of CrN, for the two interface orientations (100) and (110), and both CrN/TiN and CrN/AlN systems. At a first glance, one can immediately make three observations: (i) the values fluctuate depending on the actual cleavage plane, (ii) the actual magnetic state does not influence the values significantly (fm and afm cleavage properties are qualitatively, and often also quantitatively, almost overlapping), and (iii) the critical stress and the cleavage energy mostly follow each other. The latter can be expected since both high critical stress and high cleavage energy are related to the greater bond strengths. The (100) pm-CrN/TiN, which was cleaved just at the interface, fits into this trend as well with $E_c = 2.9\,\text{J/m}^2$ and $\sigma_c = 29.5\,\text{GPa}$.

Regarding the oscillatory behaviour, this was already shown in similar studies on different material systems [131, 132] and can be linked to Friedel oscillations in the electron charge density due to the interfaces [149]. Since the interface breaks translation symmetry, mobile charge tends to screen this perturbation. This process is, in general much more efficient in metallic systems (TiN, CrN) having free electrons than in semiconductors (AlN), the latter thus showing only very weak charge oscillations. Eventually, the charge oscillations lead to local strengthening/weakening of interplanar bonds and hence directly affect the cleavage properties. Importantly, the interface is not necessarily the weakest link in terms of the tensile strength (see, e.g., CrN/TiN (100) superlattice in Fig. 5.7b). Nevertheless, comparing the superlattice cleavage properties with values for bulk materials (solid horizontal lines), none of the systems is predicted to be superior to the individual homogeneous materials: the lowest critical stress of the superlattices (the weakest link) is always smaller than the smaller critical stress of the two bulks. Such behaviour is in line with other nitride superlattices [131, 132]. This holds true also for the direction perpendicular to the interfaces (cf. values in Figs. 5.6 and 5.7b), at least for the investigated bilayer period.

5.3.4 Fracture toughness

The stress intensity factor, K_{IC}, was calculated for different superlattice configurations according to Eq. (3.52) using the stiffness constants (Tab. 5.2) and the minimal cleavage energies from the previous section. The values are shown in Fig. 5.8. The blue and orange bars represent the (100) and (110) interfaces, respectively. Reference values for the binary nitrides are shown with the pale colours. Additional values corresponding to crack propagation planes perpendicular to the interfaces are marked with the hatched pattern. For clarity, each configuration is further labelled with the Miller indices of the crack surfaces.

The superlattice K_{IC} values never exceed the values of the corresponding binary systems (note that a fair comparison includes the same crack surfaces!). In the case of the (100) interfaces, the SL values lie always between the limits set by the binary nitrides. Contrarily, the K_{IC} SL values are lower than the corresponding binaries for the (011) orientated interfaces. This could indicate that the superlattice effect—K_{IC} values superior to the binary compounds [18, 19]—reaches the maximum enhancement for different bilayer period Λ depending on the orientation of the SL interface. Such speculation would require further analysis and likely also employment of methods beyond DFT. For the (110) directions, the binaries show higher fracture toughness compared to superlattices. This is because the cleavage energies are lower for the supercells than the ones of the binaries. Our results further

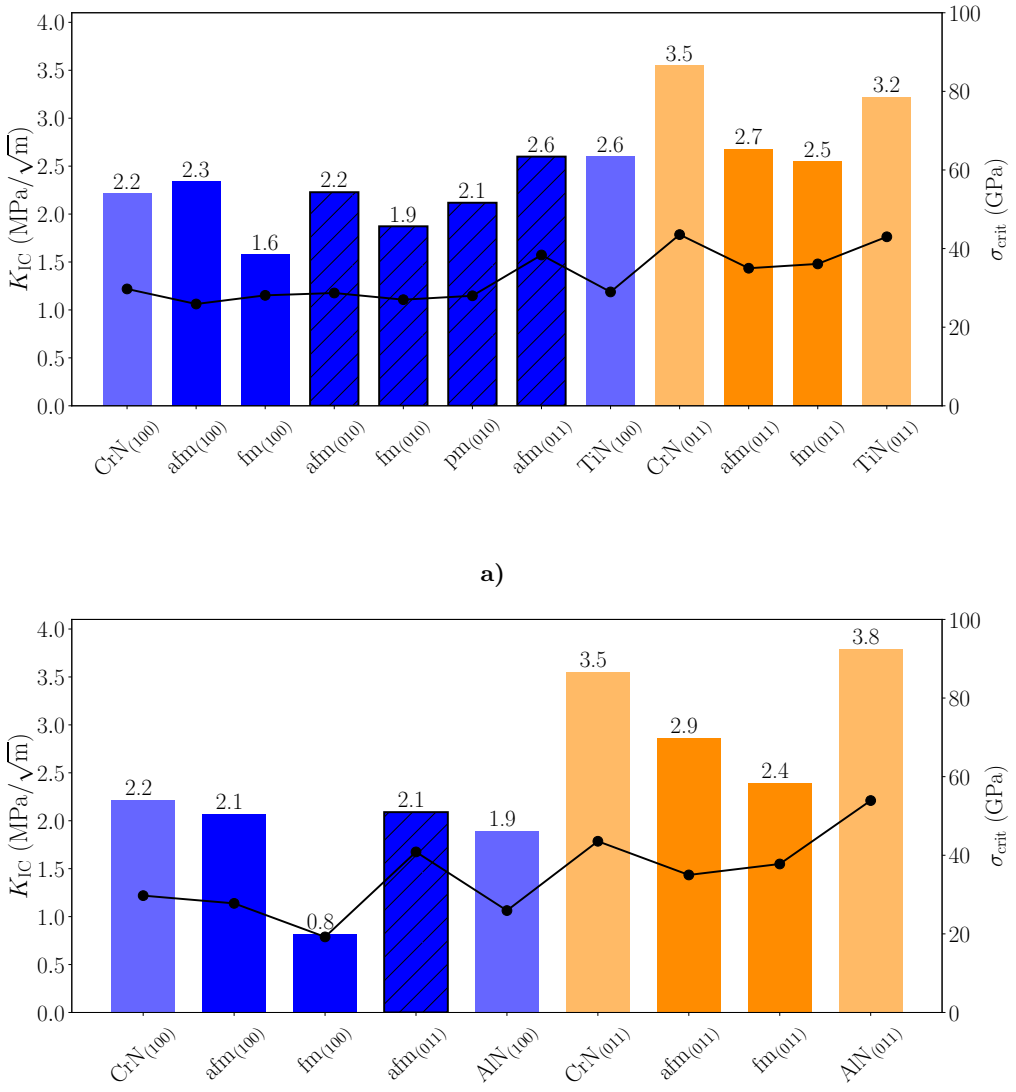

Figure 5.8: Fracture toughness K_{IC} for the a) CrN/TiN and b) CrN/AlN. The blue bars represent the (100), the orange ones the (011) interface. The black hatching denotes the fracture toughness perpendicular to the interface, the so created surface is denoted in the labels. In both material combinations, the (100) direction shows similar fracture toughness of the binaries and the superlattices even for the different fracture orientations and magnetic configurations. In contrast, the (110) interface sees a decrease in K_{IC} compared to the binaries.

suggest that cleaving the (100) planes is easier than the (011) planes. This is somewhat surprising result taking into account that the (100) direction is the stiffest for both CrN and TiN (see Fig. 5.4). According to Eq. (3.52), K_{IC} depends apart from the directional Young's modulus also on the corresponding surface energy (in our case, approximated by the cleavage energy). Therefore, the plane with the lowest cleavage energy becomes the decisive one (i.e. the weakest link) for the fracture toughness. The results in Fig. 5.7 clearly show, that the interface itself is not necessarily the weakest link: while E_c reaches a minimum at the interface in the afm-(100)CrN/AlN case, the minimum is predicted to be in the CrN layer in the afm-(011)CrN/AlN case (as well as in both fm-CrN/AlN cases). The factor limiting fracture toughness of CrN/TiN is TiN in the case of (100) interfaces, but it is the CrN in the case of (011) interfaces.

The black data points and lines in Fig. 5.8 represent corresponding σ_{crit} values. We see a qualitative agreement with the K_{IC} profile. This is not surprising since E_c and σ_{crit} are related (Eq. (3.51)), and as discussed above, E_c is the decisive quantity for the K_{IC} in the case when E_{hkl} is not vastly differing over the SL constituents. Consequently, high (minimum) critical stress can be used as an indicator for high fracture toughness.

A final comment concerns various magnetic configurations. The room temperature state of CrN is paramagnetic. Zhou *et al.* [136] suggested that (computationally cheaper) fm-CrN yields a reasonable approximation for the elasticity of pm-CrN. Inspecting the significantly lower K_{IC} values of the fm-CrN/TiN and fm-CrN/AlN SLs as compared with afm (and pm-CrN/TiN(010)), we conclude that the ferromagnetic state is not a reasonable approximation for fracture toughness. The underestimation of K_{IC} values can be traced to reduced cleavage properties in the fm state (Fig. 5.7). Although not so pronounced, such trend is also obtained for the cleavage planes perpendicular to the interface (Fig. 5.6) where the fm configuration yields both E_c and σ_{crit} lower than both afm and pm states.

5.4 Discussion

5.4.1 Stability of the afm-(100) state

The results in section 5.3.1 revealed an unexpected behaviour of fm-(100)CrN/AlN SL: stabilization of a "false" afm state (see Fig. 5.2c). In Fig. ,5.9 we show the development of individual magnetic moments of all Cr atoms during the cleavage process along various planes. The panels b and c correspond to cleaving between CrN planes -1 and -2, and -2 and -3,

respectively, demonstrate that as soon as the symmetry of the modelling box is broken by introducing extra spacing between the planes, the anti-parallel orientated spins turn back into the fm-configuration (or, similarly, that the flipping to the false afm-(100) state does not occur). On the contrary, when cleaving the SLs right in the middle of the CrN block, hence preserving the mirror symmetry of the model, the resulting system seems to alternate between two, presumably energetically almost identical, states, namely fm or afm-(100). Even more interestingly, as soon as the separation exceeds ≈ 1.5Å, the behaviour of -2 (violet) and -5 (orange) planes becomes uncorrelated (independent), meaning that the magnetic interaction causing the magnetic order becomes negligible. Those results suggest that the afm-(100) magnetic state is both a surface/interface-induced and symmetry-stabilized phenomenon.

5.4.2 Interplay between strength and magnetism

Starting from the cubic rock-salt lattice, CrN lowers its symmetry firstly by the antiferromagnetic order, which in turn leads to the orthorhombic structure [136]. Inspecting the directional Young's modulus (e.g., the green dashed lines in Fig. 5.4) yields $E_{[011]}(\mathrm{CrN}) > E_{[0\bar{1}1]}(\mathrm{CrN})$. Recalling that the afm order consists of alternating (011) double-planes with the same spin orientation (Fig. 5.1), one is tempted to ascribe the increased Young's modulus in the [011] direction to an attractive spin interaction between oppositely-orientated spins: while the Cr-Cr chains (first nearest Cr-Cr pairs) along the $[0\bar{1}1]$ consist of atoms with the same spin orientation, the Cr-Cr chains along the [011] direction contain anti-parallel spins on the Cr nearest neighbours. This speculation about magnetic-spin attraction can be further supported by inspecting the cleavage properties in Fig. 5.6d. The lowest critical stress and cleavage energy are obtained for cleaving between planes -2 and -3, which have parallel-orientated spins (Fig. 5.3d). On the other hand, cohesion between planes -3 and -4, and -2 and -1, in each case with oppositely orientated spins is clearly higher.

5.4.3 Experimental evidence

Figure 5.10shows the experimental results for the hardness, H, fracture toughness, K_{IC}, and Young's modulus, E, plot against the bilayer period of CrN/TiN superlattices as reported in Ref [130]. Both H and K_{IC}, exhibit the superlattice effect by peaking at a small bilayer period, similarly to previously reported behaviour for CrN/TiN [18] and other superlattices, TiN/WN [19] or MoN/TaN [20]. The hardness reaches maximum of 32.2 GPa for a bilayer

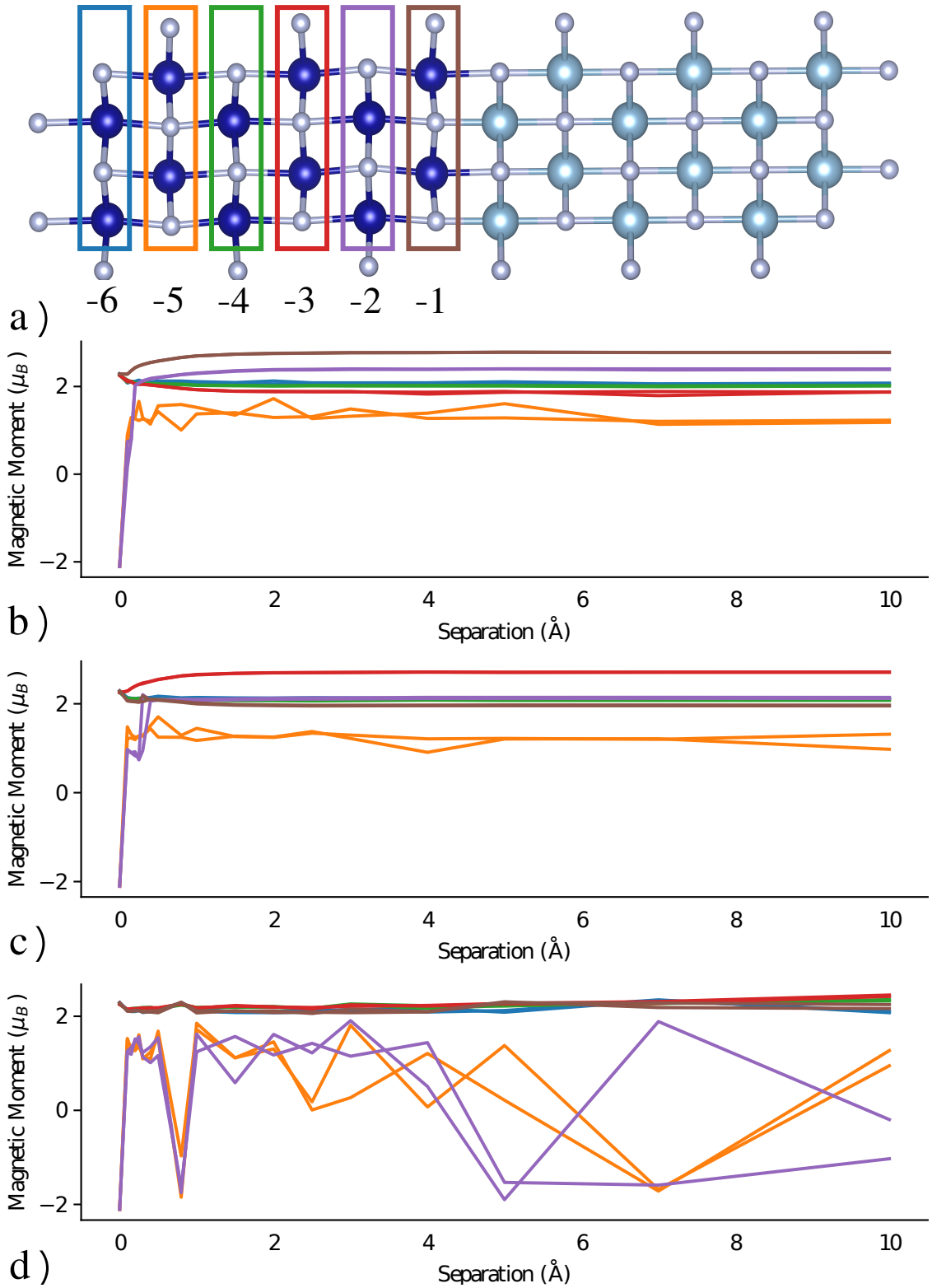

Figure 5.9: Development of the magnetic moments of the Cr atoms in fm CrN/AlN with (100) interface for the different cleaving steps. a) the coloured lines correspond to the colours used in the other plot to highlight the positions of the different Cr atoms, the dashed lines indicate the cleavage planes. b) cleaved between the planes −1 and −2, c) cleaved between the planes −2 and −3 and d) cleaved between the planes −3 and −4. Cr in the same planes have the same colours.

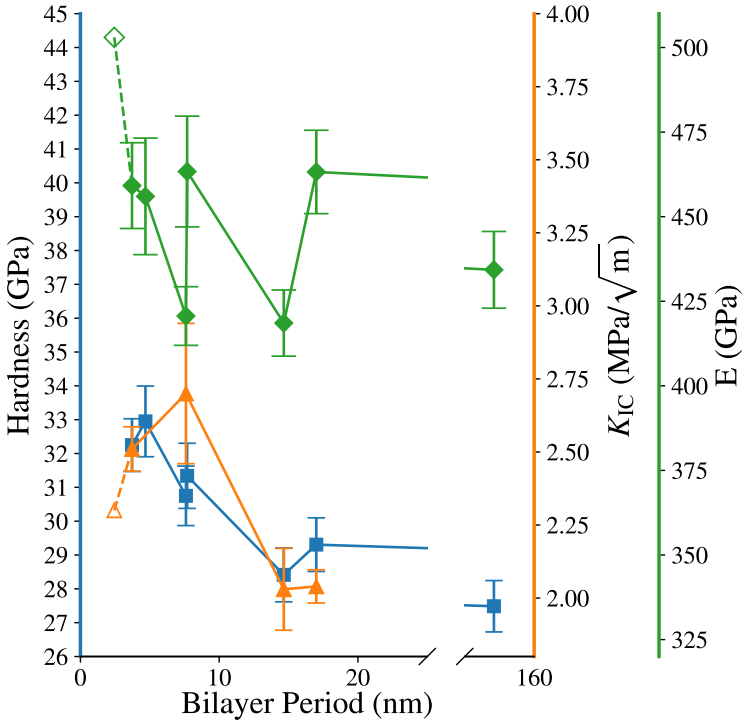

Figure 5.10: Results of the micromechanical experiments on CrN/TiN thin films. The hardness (blue squares) of the coatings increases to its maximum at a bilayer period of 4.7 nm and falls off afterwards. The fracture toughness (orange triangles) has a similar shape to the hardness, with an increase until 7.6 nm and a drop afterwards. The Young's modulus (green diamonds) exhibits fluctuating values for the different bilayer periods. For the fracture toughness and the Young's modulus, the calculated values are presented by the star symbols.

period of 4.7 nm, after which it decreases quickly to 28.4 GPa at 14.7 nm and then further decreases to 27.5 GPa at 157 nm. The fracture toughness shows a similar trend. It peaks with 2.7 MPa/$\sqrt{\text{m}}$ at a bilayer period of 7.6 nm and decreases afterwards towards 2 MPa/$\sqrt{\text{m}}$. It is important to note that the K_{IC} measurements at the peak have a high standard deviation. The absolute values for K_{IC} are in good agreement with the DFT data presented in this study. Considering that the crack in the experiment propagated perpendicular to the interfaces, the relevant values for the afm-(100)CrN/TiN system are 2.2 and 2.6 MPa/$\sqrt{\text{m}}$ for (010) and (011) fracture planes. The extrapolated experimental data trend to this small bilayer period range falls in between those two theoretical values. The indentation modulus values in Fig. 5.10 fluctuate between $\approx$ 420 and $\approx$ 463 GPa. The calculated values are in decent agreement with E_{100} for afm-(100)CrN/TiN (503 GPa). Although not an exhaustive proof, these good correlations between theoretical predictions and experimentally measured values of mechanical properties demonstrate, on the one hand, that the rather small atomistic models are relevant for modelling nitride superlattices (including magnetism), and on the other hand, they are capable of predicting not only trends, but often also quantitative values.

5.5 Summary

In this chapter, we have presented a comprehensive study on the impact of interface orientation and magnetic state of CrN/TiN and CrN/AlN cubic superlattices with a bilayer period of $\approx 2.5\,\mathrm{nm}$ on their structural and mechanical properties. Similarly to previous studies, also here interlayer distance oscillations appeared, mostly in the metallic (TiN, CrN) layers. Those were related to interface-induced Friedel charge oscillations. Analysis of local magnetic moments suggested that there is no correlation between those interplanar distances and magnetic moments on Cr atoms.

Next, we discussed the elastic properties of the superlattices. We could show that explicitly including interfaces is important, although in many cases, the computationally much more efficient continuum-mechanics based approach of Grimsditsh and Nizzoli brings sufficiently accurate results. Importantly, a hypothetical ferromagnetic state yields not only the softest elastic response but also a different symmetry of it with a very strong anisotropic character. This effectively rules out the fm state as an approximation for (computationally much more demanding) paramagnetic state of CrN.

Lastly, we calculated fracture toughness, K_{IC}. Although none of our geometries showed a superlattice effect, i.e. values exceeding those of binary constituent materials, a comparison with relevant experimental data from literature suggested not only qualitative but also quantitative agreement. The studied superlattice bilayer period of $\approx 2.5\,\mathrm{nm}$, mostly limited by the computationally expensive quantum mechanical treatment is smaller than that for which K_{IC} (and also hardness) experimentally show the peak.

Chapter 6

Twin boundary migration in CrN

The results of the chapter are part of the publication *Real-time atomic-resolution observation of coherent twin boundary migration in CrN* [29].

6.1 Introduction

Transition metal nitrides are known for their brittle behaviour and poor ductility, limiting their application. The mechanisms allowing plastic deformation of crystals are complicated to describe correctly. The exact mechanisms behind deformation in crystals are complicated even more for systems with simple structures. This is exacerbated for crystals with complex structures. For complex materials, a synchronous slip and twinning deformation mechanism was proposed to describe the deformation of the material [150]. The proposed mechanism could be shown in both Laves phases and α-alumina [151, 152]. For more complex materials, however, there is no evidence to support this suggested mechanism. In order to improve the poor ductility and toughness of TMN coatings engineering of grain boundaries became focus of some research and proofed effective [23, 153–155].

The rock-salt nature of CrN structure can be considered a complex crystal system with a Cr and N fcc sublattices. A special example of grain boundaries are twin boundaries which have gathered interest in recent times. In fcc metals, the $\Sigma 3\{111\}$ coherent twin boundary (CTB) was shown to improve strength, ductility, plasticity and thermal stability. [156–159]. Both the CTB defect motion and the migration of CTBs play a key role in the deformation and softening behaviour of metals [160–162] and were extensively studied. In TMNs, however, the processes of CTB migration had not been clearly described prior to this study. The lack of experimental results in rock-salt TMNs is partly due to the difficulty to image the light N atoms, thus preventing the acquisition of a clear picture of the real CTBs structure in

rock-salt TMNs. In addition, the stacking fault energy in transition metal nitrides is much higher ($\sim$1 J/m^2 [163–165]) then in metals, thus leading to fewer twins and making any observation more difficult.

The aim of this study was to shed light on the nucleation and migration of twin boundaries in CrN. A special focus was put on twin boundaries, namely the $\Sigma3\{111\}$ twin boundary. For this purpose, we employed DFT calculations which complement the experimental results published in Ref. [29].

6.2 Simulations

Ab initio calculations were performed within the Density Functional Theory as implemented in the Vienna Ab initio Simulation Package (VASP)[104]. The projector augmented wave method [105] potentials together with the generalised gradient approximation [166] to describe the exchange and correlation effects were employed. For these calculations, a cut-off energy of 500 eV and an automatically generated k-point mesh with a density corresponding to a length parameter $R_K = 50$ Å were used. The calculations were considered converged when the energy difference is smaller than 10^{-5} eV and the forces differ less than 10^{-2} eV/Å.

In order to create a $\Sigma3\{111\}$ twin boundary, Cr and N layers were stacked along the [111] lattice direction. To later allow for the required shear in individual planes to migrate the CTB, the other lattice directions are $[11\bar{2}]$ (the shear direction) and $[1\bar{1}0]$. In the defect-free configuration, the stacking order along [111] would be $A-B-C$ for Cr and $\alpha-\beta-\gamma$ for the N planes. A twin boundary is, in essence, a fault in the stacking sequence, reversing the order at the so called mirror plane. In TMNs this leaves the possibility that the mirror plane can be either a TM (Cr) or an N layer. For a CTB the order changes from $A\ \alpha\ B\ \beta\ C\ \gamma\ A\ \alpha\ B\ \beta\ C\ \gamma$ in the defect-free crystal to $A\ \alpha\ B\ \beta\ C\ \gamma\ C\ \beta\ B\ \beta\ A\ \alpha$ with the γ nitrogen plane as the mirror plane of the twin boundary (see Fig. 6.1 panel on the left). The twin boundary can migrate when the planes (Cr and N) next to the mirror plane move along the $[11\bar{2}]$ direction (in opposite directions from each other) restoring the stacking order of the perfect system. In the example above, this would mean a C-Cr and β-N plane shear to A-Cr and α-N, respectively. When both planes reach their new configuration, the B-Cr layer becomes the new mirror plane. There are six scenarios to reach the new configuration. First, one can distinguish between different orders. The Cr and N planes can shear either after each other or consecutively (asynchronous) or simultaneously (synchronous). For the asynchronous case, it would be possible for either the Cr or the N plane to move first. Another distinction is the direction of shear for the Cr and N planes. The planes could move either directly (direct)

Scenario	Order	Path	distance (Å)	Figure
1	Cr then N			
2	N then Cr	extended	1.69	Figures 6.3
3	Synchronous			
4	Cr then N			
5	N then Cr	direct	0.84	Figures 6.2
6	Synchronous			

Table 6.1: The different scenarios of migration for a $\Sigma 3\{111\}$ twin boundary. The arrow that indicates the direction of shear is valid for the crystal orientation shown in Fig. 6.1.

to the correct stacking order, C to A for Cr and β to α, or over an intermediate (extended) step, C to B to A and β to γ to α (see Fig. 6.1). A summary of the different cases can be found in Tab. 6.1.

Preceding the calculations to determine the CTB barriers, the cell containing a twin boundary (with N mirror plane) was structurally fully relaxed. A Cr and N layer was gradually moved along the $[11\bar{2}]$ direction, calculating the energy to determine the shear activation barriers for twin boundary migration. During the relaxation, the atoms were fixed in the x ($[11\bar{2}]$) and y ($[1\bar{1}0]$) direction so that only relaxation in the z ($[111]$) direction was possible. The top and bottom six layers were fixed in the z direction to mimic the bulk contribution. The barrier was calculated from the difference in energy between the individual steps and the relaxed state.

The CrN was considered in its anti-ferromagnetic state [135], to create the alternating sheets of Cr atoms with spin up and down the Cr layers were split into two sections along the [110] direction. The initial magnetic moment for the Cr atoms was set to $\pm 1.5\,\mu_{\mathrm{B}}$.

6.2.1 Results

The energy barriers for the direct migration paths (*Scenarios* 1-3) can be seen in Fig. 6.2. For the twin boundary to migrate, each plane has to shear for 0.84 Å in the $[11\bar{2}]$ direction. For the first 0.12 Å the three scenarios are energetically independent of the order in which the layers are moved. After that point, *Scenario* 2, in the N plane shifts first, starts to deviate from the other two scenarios in this group, which exhibit a smaller initial barrier. The maximum of the energy barriers are reached during the shift of the second plane for the asynchronous cases at -0.36 Å for *Scenario* 1 (blue in 6.2), 0.24 Å for *Scenario* 2 (green in 6.2) (green)) and after 0.6 Å for the synchronous *Scenario* 3 (red). The total height of

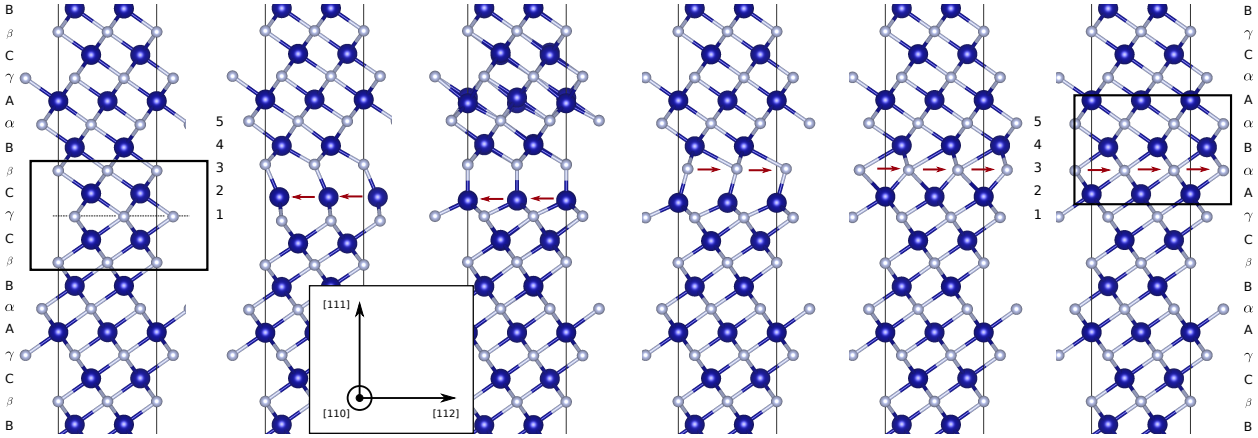

Figure 6.1: Example movement of the twin-boundary. On the left-hand side, the initial twin boundary can be seen in the middle of the black box as the centre line of N atoms (grey spheres). In the case shown, one of the adjacent Cr layers is moved along $[11\bar{2}]$ direction, and then the next N layer is transferred in the $[11\bar{2}]$ direction until a new twin-boundary forms. The new twin can be seen on the right-hand side in the black rectangle. This time as the line of Cr atoms (blue spheres) in the middle of the box.

the barriers are 1.18, 1.4 and 1.28 J/m^2 for *Scenario* 1, 2 and 3 respectively, making the first scenario the easiest out of those three. After both planes completed their shear of 0.84 Å, three scenarios end at 1 J/m^2. However, to fully create the new Cr mirror plane, another shear along the $[1\bar{1}0]$ direction is required reducing lowering the final energy to 0.42 J/m^2 which is also the energy difference between twin boundaries with a Cr or an N mirror plane. The barriers for the extended cases can be found in Fig. 6.3. In contrast to the direct cases, the shapes of the three scenarios differ. *Scenario* 4 has a local minimum after the Cr plane shifted completely and two maxima at 1.2 and −0.22 Å of shear. The maximum here is at 1.49 J/m^2 and with that higher than all three scenarios discussed before. *Scenario* 3 starts similar to *Scenario* 4, however, at the end of the initial shift of the N plane, the energy barrier increases drastically to values above 3 J/m^2. This sharp increase seems implausible; an investigation of the interplanar spacing and magnetic state could not provide any explanation yet. It could be that these two specific configurations have poorly chosen positions of the shifted atoms resulting in high energies. Concerning which scenario is the most likely for the twin boundary migration, *Scenario* 5 is still unlike as the barrier is already higher than 1.5 J/m^2 at a shear of 0.96 Å. *Scenario* 6 exhibits the highest barrier, excluding the doubtful values of *Scenario* 5, with 2.49 J/m^2 at a shear of −0.24 Å. For the extended scenarios, the new mirror plane is completely formed after a shift of the two planes for 1.69 Å. As for the direct cases, the energy difference between the N and the Cr mirror plane at the beginning and the end is 0.42 J/m^2.

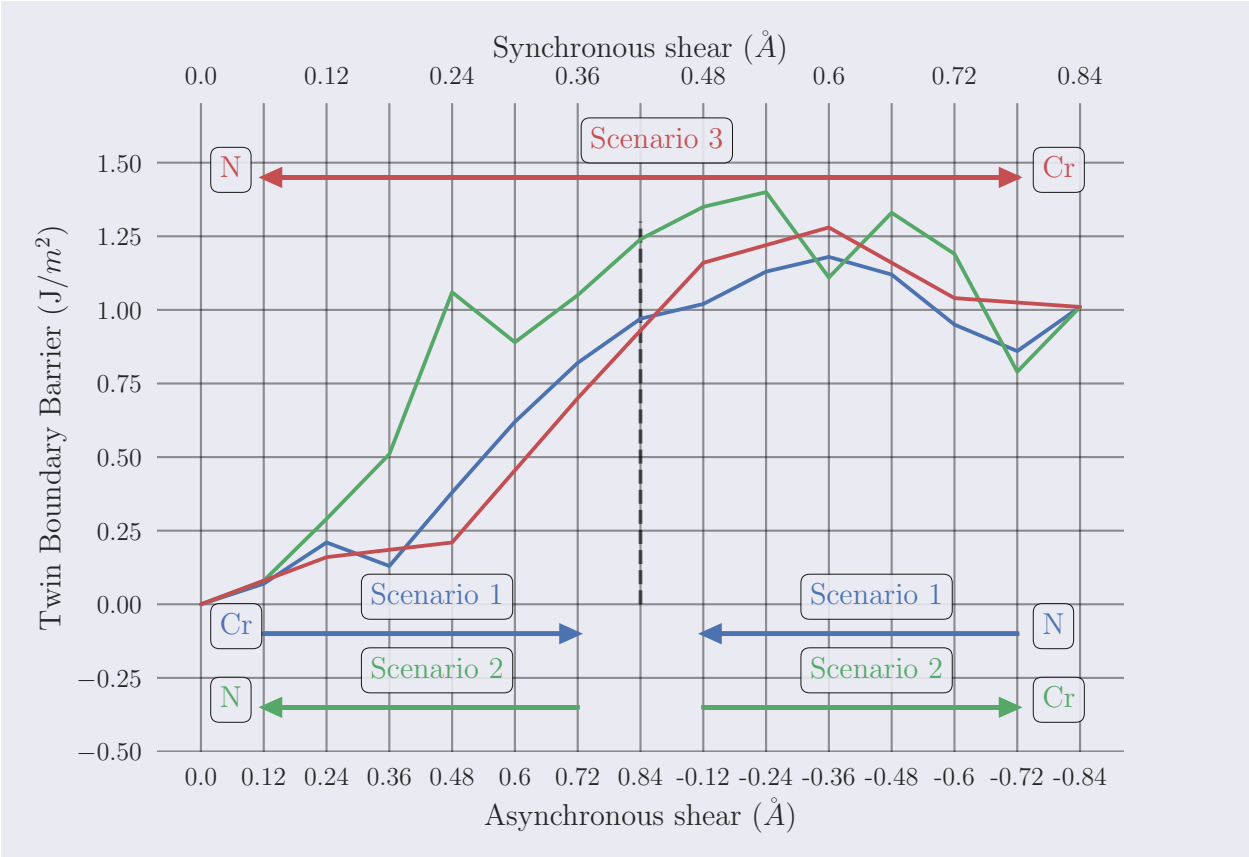

Figure 6.2: Energy barriers for the direct scenarios of the twin boundary migration. The x axis on the bottom corresponds to scenarios 1 and 2, whereas the numbers shown are for *Scenario* 1 (Cr and then N). For *Scenario* 2 the sign for the x axis changes. The top x axis relates to the *Scenario* 3, with the labels denoting the shift of the Cr atoms.

6.2.2 Discussion

Looking at the six scenarios, *Scenario* 1 is the one with the lowest barrier and should therefore be the preferred path for $\Sigma 3\{111\}$ twin boundary migration starting with an N mirror plane. From the point of a Cr terminated CTB, the inverse path of *Scenario* 1 should be the one with the lowest barrier, which means the process is reversible. Again the direct path to reinstate the correct stacking order is taken (change of direction for both N and Cr), starting this time with the shear of one of the N planes next to the Cr mirror plane, followed by the corresponding Cr plane. The symmetric geometry of the twin boundary has the consequence that it can migrate in either direction along [111] without considering any external stresses. The energy difference of $0.45\,\mathrm{J/m^2}$ between the N and Cr terminated twin boundary suggests that CTBs with N mirror is the stable configuration.

The results are in good agreement with high-resolution transmission electron microscopy (HRTEM) findings of twin boundaries in CrN [29]. Most of the observed CTB in this study

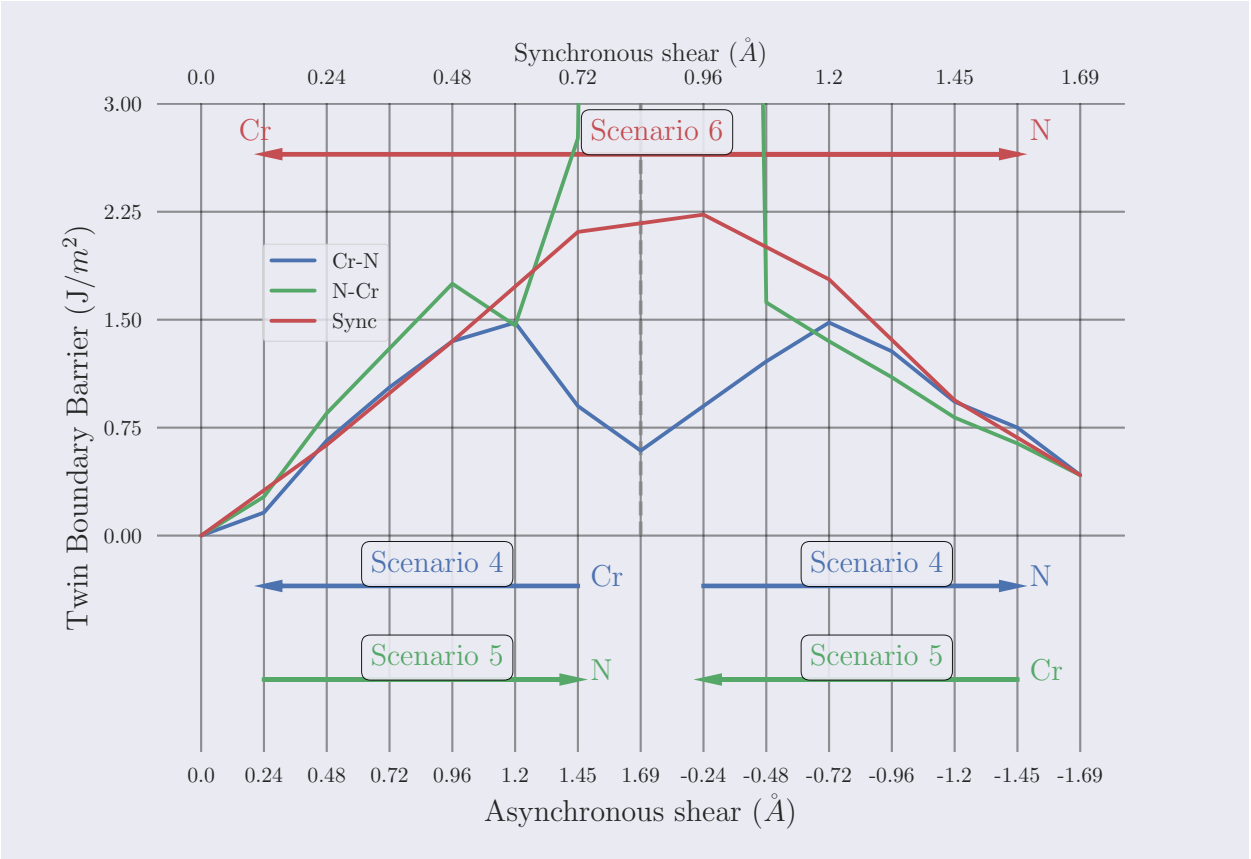

Figure 6.3: Energy barriers for the direct scenarios of the twin boundary migration. The x axis on the bottom corresponds to *Scenarios* 4 and 5, whereas the numbers are shown for *Scenario* 5 (N and then Cr). For *Scenario* 4 the sign for the x axis changes. The top x axis relates to the *Scenario* 6, with the labels denoting the shift of the Cr atoms.

were N terminated, supporting the conclusion that a Cr mirror plane is an unstable state. During the HRTEM investigation, the authors were also able to observe the migration of a CTB, confirming an asynchronous process starting with motion of the Cr plane before the N plane follows, which corresponds to *Scenario* 1 in the calculations.

6.2.3 Conclusion

In this chapter, the different possible paths for $\Sigma 3\{111\}$ twin boundary migration in CrN were investigated with Density Functional Theory. We were able to show that an asynchronous process with shear of a Cr flowed by an N plane going directly to the correct stacking order is the preferred path. It was also revealed that a CTB is in its stable state when terminated by an N plane.

Chapter 7

Tensile loading of AlN/TiN superlattices

Parts of the results in the following chapter were published in: *Atomistic mechanisms underlying plasticity and crack growth in ceramics: a case study of AlN/TiN superlatticest* [167].

7.1 Motivation

The good mechanical properties of transition metal nitrides are often diminished by their brittle nature. To improve those shortcomings, studies have shown that a superlattice structure [54, 168–170] can improve both hardness and fracture toughness [1, 24, 25, 81, 171] for certain layer thicknesses. The here studied AlN/TiN system has already attracted a lot of research interest [29, 54, 168]. The heterogeneous elastic behaviour of the two constituting materials and the lattice constants mismatch ($\approx 4.8\,\%$) [172] of their cubic (rocksalt, rs) B1 configuration make this pair a prime candidate for the superlattice effect. In a study by Fallmann *et al.* [54], magnetron-sputtered AlN/TiN multilayers with B1 structure were investigated. They determined a peak hardness ($H \approx 37\,\mathrm{GPa}$) and minimal indentation modulus ($E \approx 400\,\mathrm{GPa}$) are both present in the smallest bilayer period of 2.5 nm. Applying the empirical approach of H/E ratio as an indicator for the toughness of a material, [173–175] one can conclude that the smallest bilayer periods are the most promising candidates for improved mechanical properties. This conclusion is supported by cube-corner indentation experiments, which find higher toughness for smaller bilayer periods as well [54]. Since B1-AlN is metastable, the range of thicknesses to fully stabilise AlN in the B1 phase is rather limited. Dependent on the substrate, the maximum layer thickness is the smallest of

1.5 nm for MgO (100) and 0.9 nm for Si(100) or Al_2O_3 [54, 176, 177]. At larger thicknesses, the B1-AlN tends to transform to its ground-state, the hexagonal B4-structure (wurtzite, wz). AlN has a third polymorph: it assumes the cubic B3 structure (zincblende, zb). Despite better matching lattice parameters between the rocksalt TiN and the zincblende AlN, a free dangling N bond in this configuration leads to higher interface energies. This leads to the stabilisation of AlN in its B1 phase [178]. Knowledge of the transition between the AlN phases makes it possible to design coatings with the desired properties and to hinder unwanted transformations [179]. DFT studies have shown that the transition from B3 to B1 can be triggered by uniaxial loading along the [110] direction [98]. The B4 to B1 transition happens similarly under a uniaxial tension along the $[1\bar{2}10]$ direction or by shear in the $(10\bar{1}0)[1\bar{2}10]$ slip system of the hexagonal system [99].

In this study, classical molecular dynamics simulations were performed to investigate mechanisms behind the strengthening of multilayered structures at the atomistic level.

7.2 Simulations

Classical molecular dynamics simulations (CMD) were performed within the MD code LAMMPS [106]. The interatomic interactions were described with a Modified Embedded-Atom Method (MEAM) MEAM Al-Ti-N potential created by Almyras *et al.* [180]. The timestep between two consecutive steps was set to 1 fs for all simulations. The cells for tensile simulations contained around 250 000–300 000 atoms with non equilibrium dimensions of $7.6 \times 7.6 \times 40.3$ nm and $8.5 \times 7.1 \times 45.0$ nm. The cells are made up of alternating TiN and AlN layers, of the same thicknesses, with B1 (rocksalt) structure and nominal bilayer periods of $\Lambda = 1.25$, 2.5, 5 and 10 nm. The layers were stacked along the vertical z axis along the [001] lattice direction. The horizontal x and y axis are along the [100]/[[110] and [010]/$[1\bar{1}0]$] respectively. Before the cells were put under uniaxial tensile loading, they were relaxed at 300 K under isobaric-isothermal (NPT) conditions governed by the Nosé-Hoover thermostat controlling the stress(pressure) on the non-strained lattice directions. The strain was applied along the different directions in increments of 0.005 Å in each timestep which translates to a constant rate of 500 m/s. The resulting stresses were calculated every 100th step and stored along with the atomic positions for further evaluation.

The analysis of the simulations and visualisations were done with the help of the OVITO package [181]. The presence of B3 and B4 structures was determined with the help of the *Identify diamond structure* [182] function and the *Dislocation analysis* [183] function was used to determine the dislocation length in the superlattices.

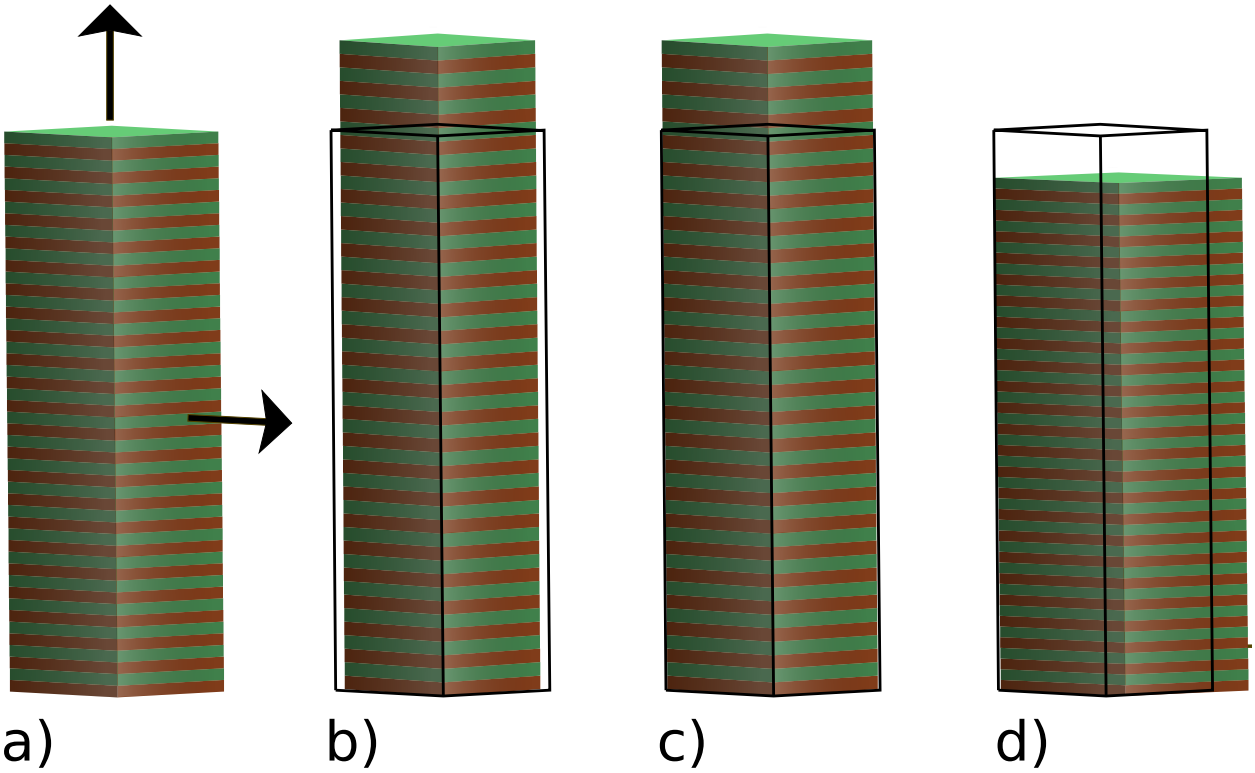

Figure 7.1: Scheme of a tensile simulation of a multilayered cell. a) the relaxed box is strained within the interface plane or perpendicular to it. b) Tensile loading out of the interface plane along [001] with Poisson's contraction considered. c) Tensile loading out of the interface plane along [001] without Poisson's contraction. d) Tensile loading within the interface plane considering Poisson's contraction.

It should be noted that the simulations assume a perfect initial structure without any prior impurities like vacancies, dislocations or cracks. Therefore, the mechanical response reported in this work corresponds to the ideal scenario and should be looked at only qualitatively.

7.3 Results

Stress-strain curves

The AlN/TiN superlattice was put under uniaxial tensile loading in three lattice directions within the interface and perpendicular to it. Applying tension parallel to the interface (along [100] or [110]) can be related to micromechanical experiments like nanoindentation [184] and microcantilever bending, [49, 50] which introduce an in-plane tensile stress state. The results of those simulations show the capability of the coating to redistribute pressure applied normal to the surface (i.e. nanoindentation) laterally. On the other hand, tensile loading perpendicular to the interface (along [001]) can show the resistance of the coating against delamination. Figure 7.2 shows the stress/strain curves (σ/ϵ) of the different bilayer

periods strained along the various lattice directions. A few parameters are used to describe and compare the different systems and scenarios. The yield strain (ϵ_Y) denotes the end of elastic and the start of plastic deformation. In the cases without plastic deformation, ϵ_Y is calculated as the point where the σ/ϵ slope is $\leq 10\,\%$ of the initial slope. The corresponding stress is the yield strength (σ_Y). The point of the maximal stress is the tensile strength (σ_T) at (ϵ_T). The last point of interest is the point of fracture at the fracture strain (ϵ_F). It is connected to the modulus of toughness (U_T), which is described by the area under the σ/ϵ curve representing the ability of the material to store energy until the point of fracture without any initial crack present.

The stress/strain curves for loading along the [100] direction can be seen in Fig. 7.2 a) and b). The former contains the results without consideration of Poisson's contraction, the latter with. The overall trends for both cases are similar. The main difference is overall higher σ_T and a larger impact of the bilayer period on σ_T and ϵ_T when Poisson's contraction is not considered. Another difference is the non-zero stresses in the two other lattice directions in the cases with fixed cell sizes. Without relaxation, the maximal tensile strengths are 24.2, 21.2 and 16.5 GPa for bilayer thicknesses of 2.5, 5 and 10 nm. Allowing relaxation decreases σ_T to 19.3, 19.0, 17.2 and 16.0 GPa for thicknesses of 1.2, 2.5, 5 and 10 nm respectively. The difference between the two methods is with 25 and 22 % much larger for the thinner layers of 2.5 and 5 nm than for the 10 nm with just 10 %. A reduction of the bilayer period from 2.5 nm to 1.25 nm results in only a marginal increase of both σ_T and ϵ_T. For both approaches, the initial slopes for the different bilayer periods are the same. The curves start to separate when the yield strength is reached, which happens at strains around 4 %. One can see a short period of decreasing stresses at ϵ_Y in both Fig. 7.2 a) and b). At this point, the coordination number of some AlN atoms changes from 6 to 4–5, i.e. not yet fully transforming. The transition from the initial B1 rocksalt structure to B3 starts at strains of about 10 %. After reaching σ_T the stresses drop sharply to around 7–10 GPa where the stress stays for the remainder of the simulation. The points of fracture (ϵ_F) for loading along the [100] were determined by a visual inspection, looking for the development of cracks in the simulation box. It should be noted here that for the remaining loading scenarios, Poisson's contraction was always considered, as it is expected to mimic closer the material's behaviour under realistic loading conditions of coatings. The initial results are qualitatively similar for the two scenarios loaded along the [100]. Therefore, the evaluation of phase transformation, dislocation development and failure mechanisms was limited to these cases.

The stress-strain curves for tensile loading along the [110] lattice direction can be seen in Fig. 7.2 c), straining the cell again within the interface plane. The results show that loading

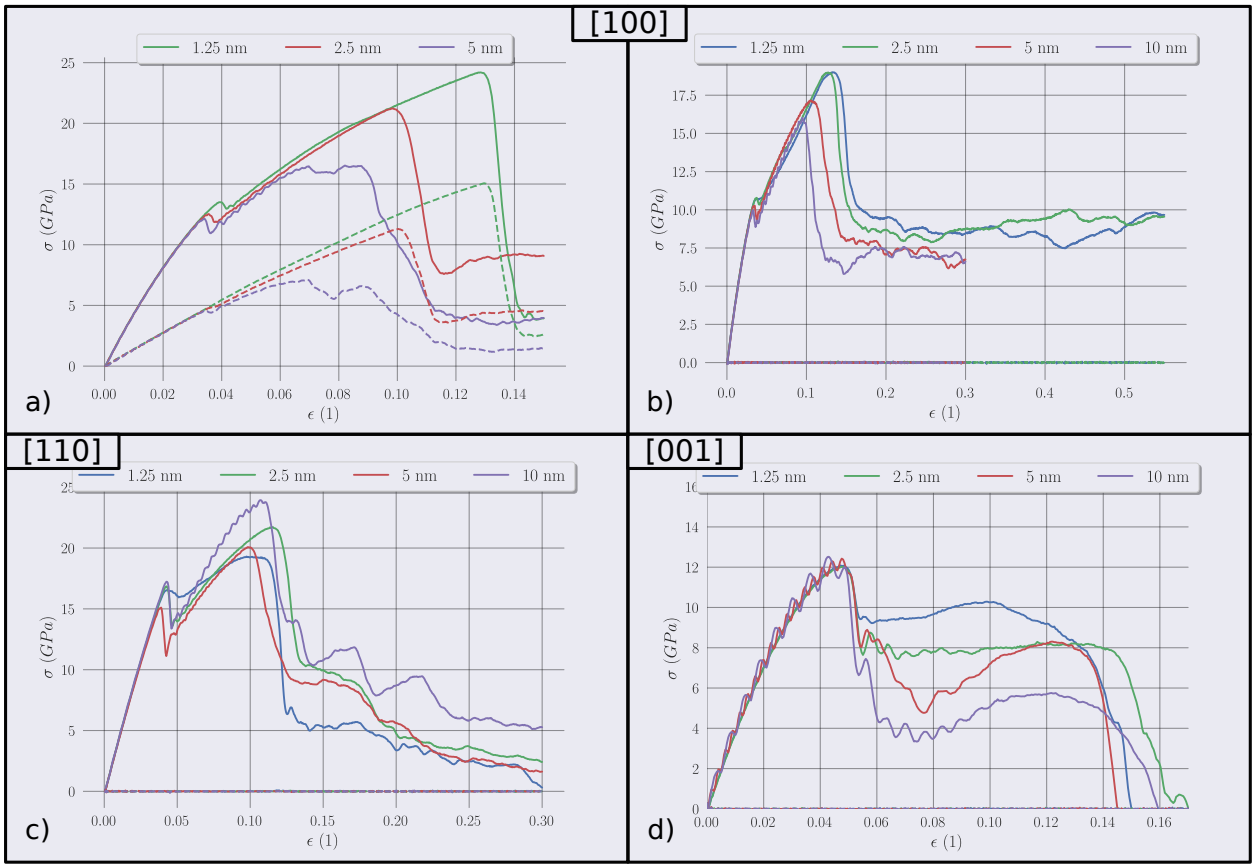

Figure 7.2: σ-ϵ curves for the different layer thicknesses strained along the [100] a) without Poisson's contraction and b) with Poisson's contraction, c) [110] and d) [001] direction.

along [110] the superlattices exhibit stronger resistance with the highest σ_T overall. The ultimate tensile strength are 19.3, 19.0, 20.1 and 23.6 GPa for 1.2, 2.5, 5 and 10 nm bilayer thicknesses respectively. In all cases, σ_T corresponds to strains around 10 %. In line with the loading along the [100] direction, the yield strength is reached at strains of about 4 % accompanied by a short period of stress relief. After reaching σ_T the stresses decrease sharply by roughly 10 GPa. In contrast to the previous cases, the stresses stay not at a constant level but decrease slowly until the formation of cracks.

Strain applied perpendicular to the interface along the [001] direction yields the lowest overall ultimate tensile strength with values for σ_T between 12.1–12.5 GPa (see Fig. 7.2 d). In contrast, the cells show no plastic deformation before σ_T is reached. The consequence of this is that $\sigma_T = \sigma_Y$ and $\epsilon_T = \epsilon_Y$. With increasing bilayer period, there is a slight increase in σ_T. After reaching the tensile strength, the stresses are relieved by the B1→B4 transformation before any occurrence of cracks.

Strain	Λ [nm]	ϵ_Y [%]	[GPa]	U_T [GPa]
[100]	**1.25**	4.0	19.3 (13.6%)	5.00 (50.0%)
	2.5	3.6	19.0 (12.4%)	5.06 (50.0%)
	5	3.5	17.2 (10.5%)	2.81 (30.0%)
	10	3.2	16.0 (9.5%)	2.50 (30.0%)
[110]	**1.25**	4.3	19.3 (9.7%)	2.44 (30.0%)
	2.5	4.2	21.7 (11.5%)	2.93 (30.0%)
	5	3.9	20.1 (9.8%)	2.58 (30.0%)
	10	4.1	23.6 (10.7%)	3.3 (30.0%)
[001]	**1.25**	4.7	12.1 (4.7%)	1.26 (15.0%)
	2.5	4.8	12.0 (4.8%)	1.23 (17.0%)
	5	4.8	12.4 (4.8%)	1.05 (14.5%)
	10	4.3	12.5 (4.3%)	0.91 (16.0%)

Table 7.1: The yield strain ϵ_Y, the tensile strength σ_T (at $\epsilon_{\max}$) and the modulus of toughness U_T (at ϵ_F). The strains at which the [100] and [110] start to fracture were visually determined by monitoring the development of cracks during the simulations considering the Poisson's contraction. For the [001] case, the cells separated when the curves reach zero for the first time after the start of the simulation.

Structure evolution and dislocations

The large scale CMD simulations allow to look into changes in the crystal structure, the failure mechanisms and the evolution of dislocations which all play a significant role in determining the strength of the superlattice. Figures 7.3-7.4 show snapshots of the AlN/TiN superlattices at certain strains for the different loading scenarios and highlight areas of phase transformation, dislocations and cracks.

Applying tensile loading along the [100] direction shows increased plasticity for smaller bilayer periods. As one can see in Fig. 7.3, the cells with $\Lambda = 1.25$–$2.5\,\text{nm}$ show no visible cracks even at strains of 50 %, whereas the larger bilayer periods exhibit the first cracks already at 15 % strain. This is due to the influence of the layer thickness on plastic deformation processes. For both Λ 1.25 and 2.5 nm dislocation networks form, spanning over multiple AlN and TiN layers. The dislocations are accompanied by local phase transformations of the B1 structure to mainly the hexagonal B4 or the hexagonal B_k phase (#194, $P6_3/mm$ [185, 186]) (Fig. 7.6). The B_k phase is an intermediate phase between B1 and B4 [186]. The ratio between B3 and B4(B_k) starts with one to one (with up to 10 % each)for $\Lambda = 1.25\,\text{nm}$ and then shifts towards more B4 regions. In larger bilayer periods, the dislocations and areas of transformation are predominantly located in the AlN layers without any networks spanning over several layers. Both the phase transformations and the nucleation of dislocations are initiated and start to grow rapidly at around $\epsilon = 10\,\%$ (Figures 7.8 and 7.7 a)).

This coincides with σ_T and the sharp decrease in stress as shown in 7.2 b). For the smaller bilayer periods, the fraction of transformed phases increases further after reaching σ_T. The phase transformation allows for the continuous release of stress during elongation due to the transformation. The initial defects form in the AlN layers (for all Λ) and often take the shape of Λ or V, as seen in Fig. 7.6 a). At the beginning of the defect growth, the interfaces stay coherent for superlattices with larger bilayer periods (Λ = 5 and 10 nm), However, the created wedges deform the Ti-N bonds locally and, under further elongation in the [100] direction, lead to the formation of nano-sized cracks in the TiN layers. The thinner bilayer periods (Λ = 1.25 and 2.5 nm) on the other hand, it shows that the formation of B4 in AlN which grows then into TiN (Λ = 1.25 nm) or simultaneous transformations of B1 to B_k in both AlN and TiN layers. The necessity for the transformation to cross the interface leads to a significant delay in fracture for the small bilayers, as it allows for a redistribution of the stresses. Energetically one can think that the transformation of a part of thin TiN layers is favoured over the induced interface strain between B1-TiN and B4-AlN. In the thicker layer, on the other hand, the interfacial strain is not as costly as the transformation over the whole TiN from an energy standpoint.

For strains applied along the [110] direction, the response is similar to elongation along [100]. However, there are some key differences. They show a lesser degree of dislocation formation, especially for the superlattices with smaller bilayer periods. There are no dense networks but local strands of dislocations in the {111} plane (Fig. 7.4). The Λ and V shape regions of lattice transformation can be found again when the cells are strained along the [110] direction. The simulations reveal that the most prevalent transformation is the B1 to B3 transition, which is initiated by $\{111\}\langle 1\bar{1}0\rangle$ slip. B3 starts to form in several AlN layers, as can be seen in Fig. 7.4 starting at strains of 10–12 %. There is a clear dependence on the amount of AlN that undergoes a phase transformation on the bilayer thickness. The thicker layers exhibit a significantly higher degree of transformation compared to their thinner counterparts. For Λ = 10 nm almost 50 % of the AlN transformed at the end of the simulation. This is in a strong contrast to only about 10 % for Λ = 1.25 nm. The thicker superlattices exhibit B1 to B4(B_k) transformation as well with up to 15 % for Λ = 10 nm (see Fig. 7.8 b)). When increasing the strain further, slip bands start to develop from these regions, leading to interpenetration of AlN and TiN layers. This can be clearly seen in Fig. 7.4 for Λ = 1.25 and 2.5 %. The interpenetration of the layers leads, under further elongation, to fracture in a 45° angle for all bilayer periods.

Applying tension out of the interface plane along the [001] direction reveals a significantly decreased ability of the superlattices to undergo a plastic deformation. At strains of around

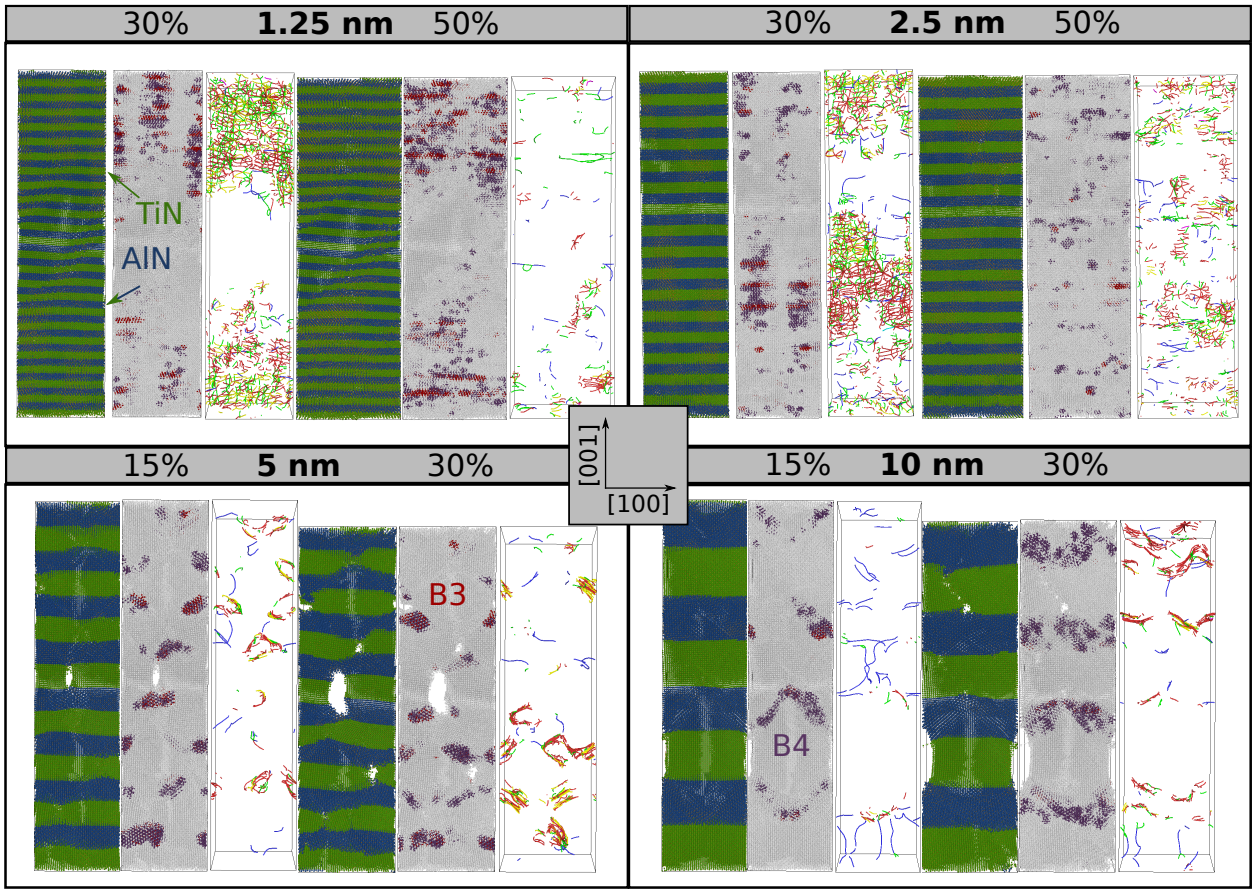

Figure 7.3: Selected snapshots of the ALN/TiN superlattices at different strains for tension [100]. For each snapshot, the superlattice structure on the left, the crystallographic phases (red = B3, purple = B4 and grey = rocksalt/other) in the middle and dislocation networks on the right are displayed.

15–18 % all bilayer periods cleave parallel to the interface in an AlN layer as seen in Fig. 7.5. The critical failure is preceded by B1 to B4(B_k) transformation in the AlN layers. The induced interface strain at the B1-TiN/B4-AlN interface weakens the bonding and leads to separation at or near the interface. The fraction of AlN that undergoes a transformation is again dependent on the bilayer period. The thicker layers exhibit a greater degree of transformation than the thinner ones, reaching up to 30 % B4(B_k) of total AlN (Figures 7.5 and 7.8 c)). For all Λ, a sharp drop in the B4 fraction, occurs once the cell is cleaved. For the $\Lambda = 5$ and 10 nm 5 and 5 % of B4 remain after the separation and the accompanied relieve of the stresses. The phase transformations are accompanied by the nucleation of some dislocations in the AlN.

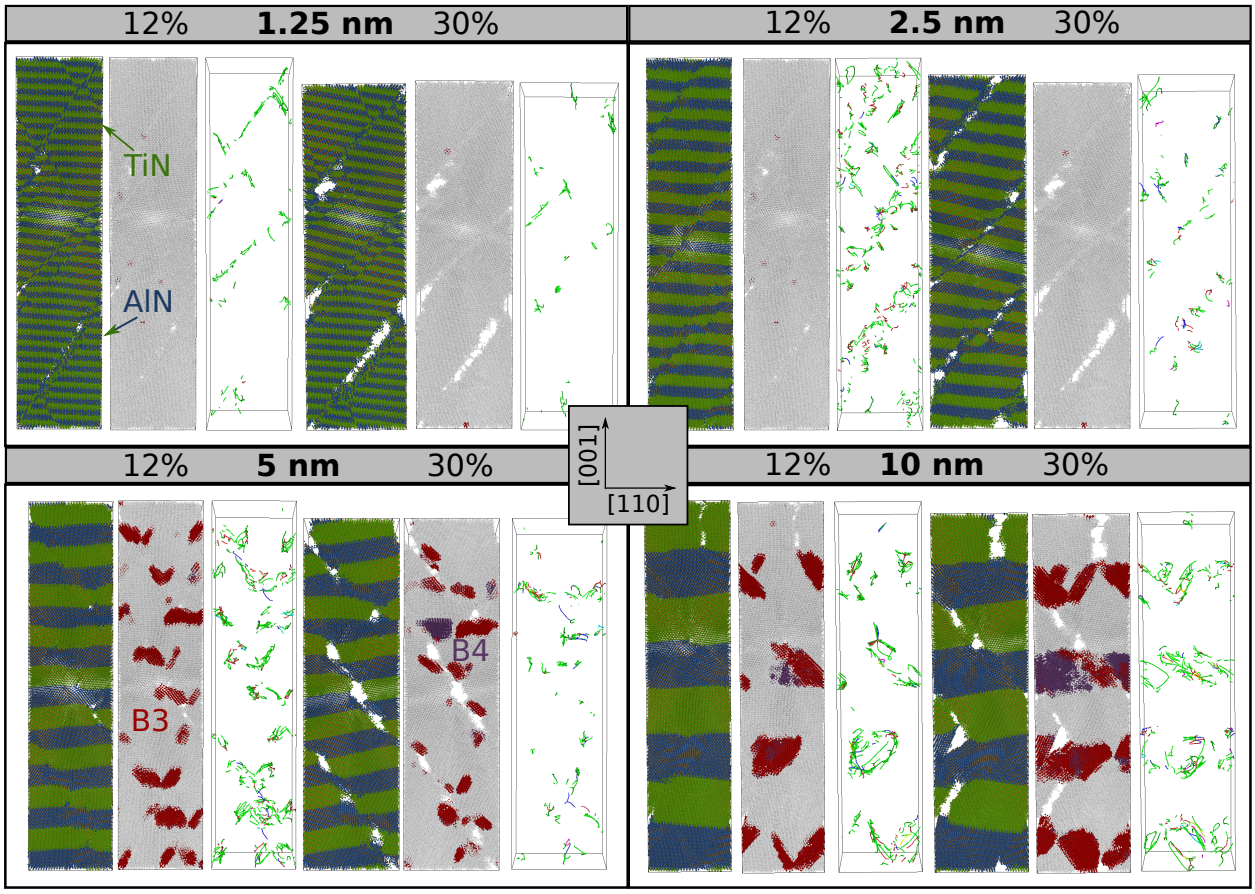

Figure 7.4: Selected snapshots of the ALN/TiN superlattices at different strains for tension [110]. For each snapshot, the superlattice structure on the left, the crystallographic phases (red = B3, purple = B4 and grey = rocksalt/other) in the middle and dislocation networks on the right are displayed.

7.4 Discussion and comparison with AIMD and experiments

The results discussed above point towards increased toughness for the AlN/TiN superlattices with moderately small bilayer periods when loaded within the interface plane. The toughening stems from the enhanced plasticity due to the B1-to-B3 and B1-to-B4 phase transitions. The findings fit well with the results from our *ab initio* molecular dynamics simulations [167]. Despite the good agreement, there are some discrepancies that should be noted. There are three reasons for the difference between the two approaches: I) the larger cell size of CMD compared to AIMD facilitate plastic deformation resulting in earlier yielding, II) the parameters of the used interatomic potential [180] in the CMD simulations was not fitted for large deformations and III) omission of the Poisson's contraction in the AIMD calculations do not allow for a relaxation of the lateral stresses. Paired with the low cutoff energy (300 eV), this leads to an overestimation of the stresses in AIMD.

Comparing the stress/strain curves of CMD and AIMD reveals over the board lower σ_T for

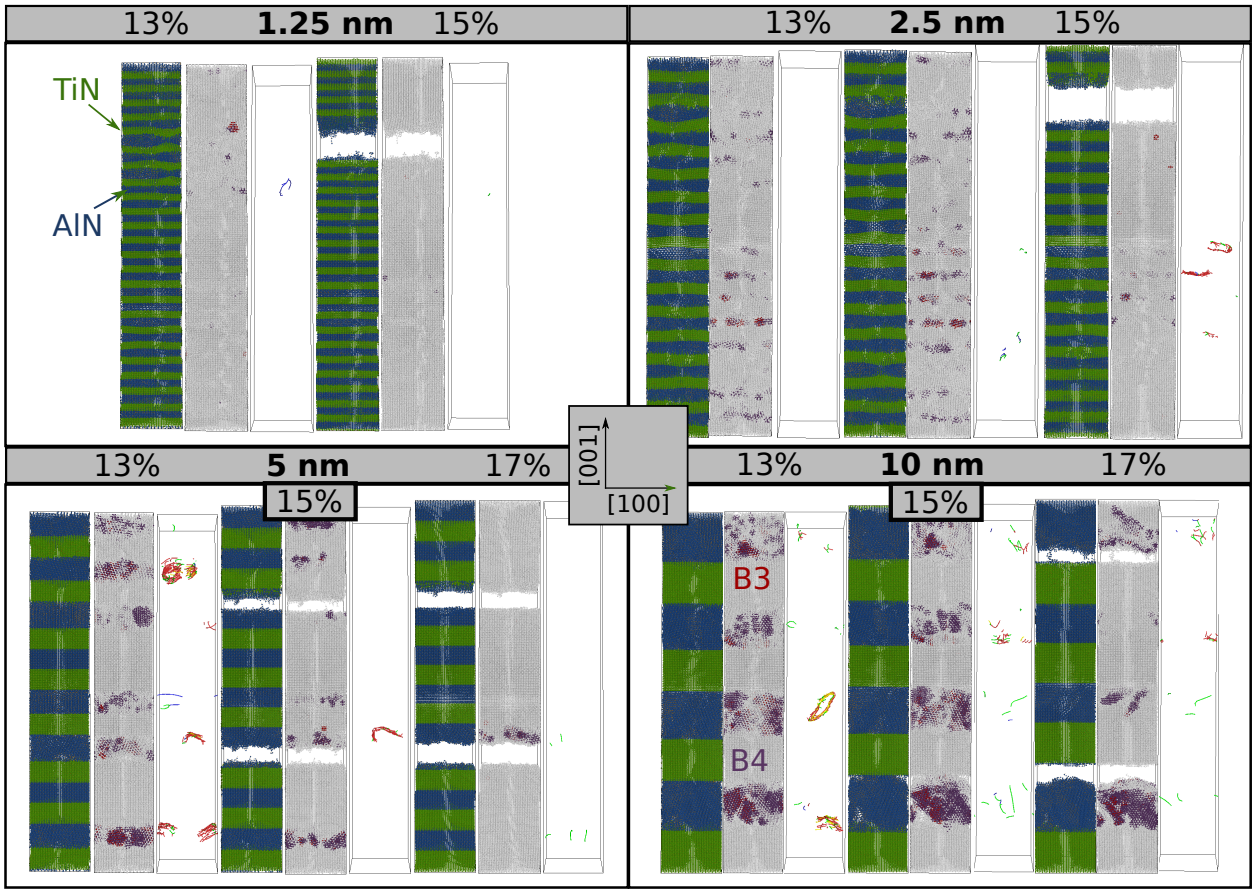

Figure 7.5: Selected snapshots of the ALN/TiN superlattices at different strains for tension [001]. For each snapshot, the superlattice structure on the left, the crystallographic phases (red = B3, purple = B4 and grey = rocksalt/other) in the middle and dislocation networks on the right are displayed.

the former. CMD shows an increase in σ_T with decreasing Λ for strains applied along the [100] direction compared to AIMD. Elongation in the other directions shows no effect of Λ on σ_T for both methods. In agreement is the increased in-plane plasticity for tensile loading along [100] and [110]. The predicted transformation paths are independent of the loading scenario (B1 $\leftrightarrow$ B3 for [110] and B1 $\leftrightarrow$ B4 for [100] and [001]) are in agreement between our CMD and the AIMD simulations [167]. Previous studies agree with our findings as well, showing the [98, 99] B3 to B1 and B4 [99] to B1 [98] pathways activated by strain. Furthermore, AIMD tensile loading of B1-$Al_{1-x}Ti_xN$ along [100] at room temperature shows the formation of tetrahedrally-coordinated (Al, Ti, N) networks and B4 like regions [31].

For both CMD and AIMD, tensile loading perpendicular to the interface in [001] direction results in cleavage parallel to the interface. Superlattices with $\Lambda = 2.5$ and 5 nm show no phase transformation in AIMD, which leads to brittle cleaving in TiN layers. In SL with $\Lambda = 1.25$ nm on the other hand, the *ab initio* simulations show a B1-to-B4 transformation in the AlN and consequently fracture at the interface in agreement with CMD. When the

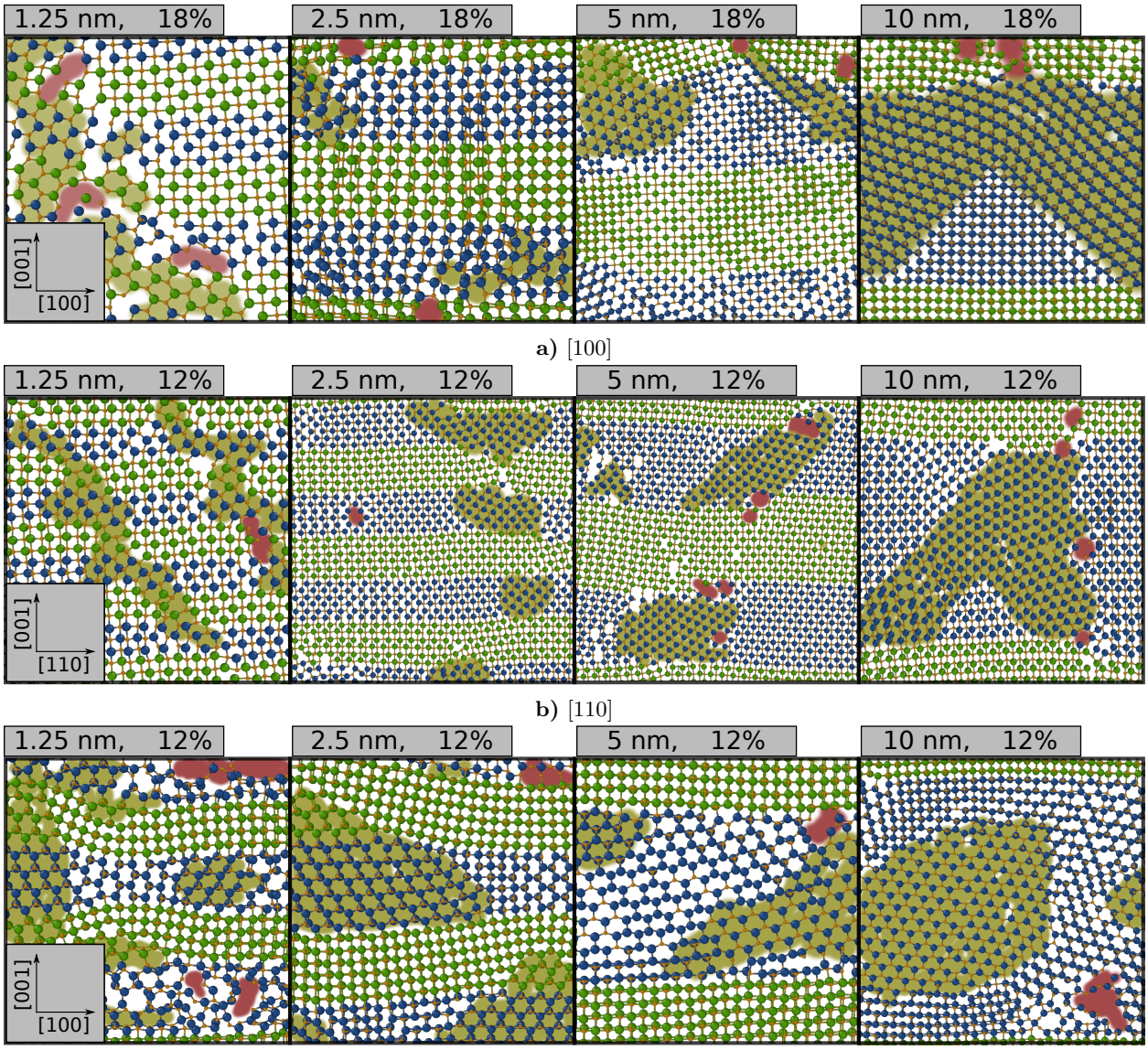

a) [100]

b) [110]

c) [001]

Figure 7.6: Selection of magnified snapshots of the AlN/TiN (blue, green) superlattices at specific strains. The images show thin slices of 1 nm (1-2 planes) for tensile loading along a) [100], b) [110] and c) [001]. The highlighted areas in yellow mark phase transformations in the cells, the red highlight marks cracks and voids.

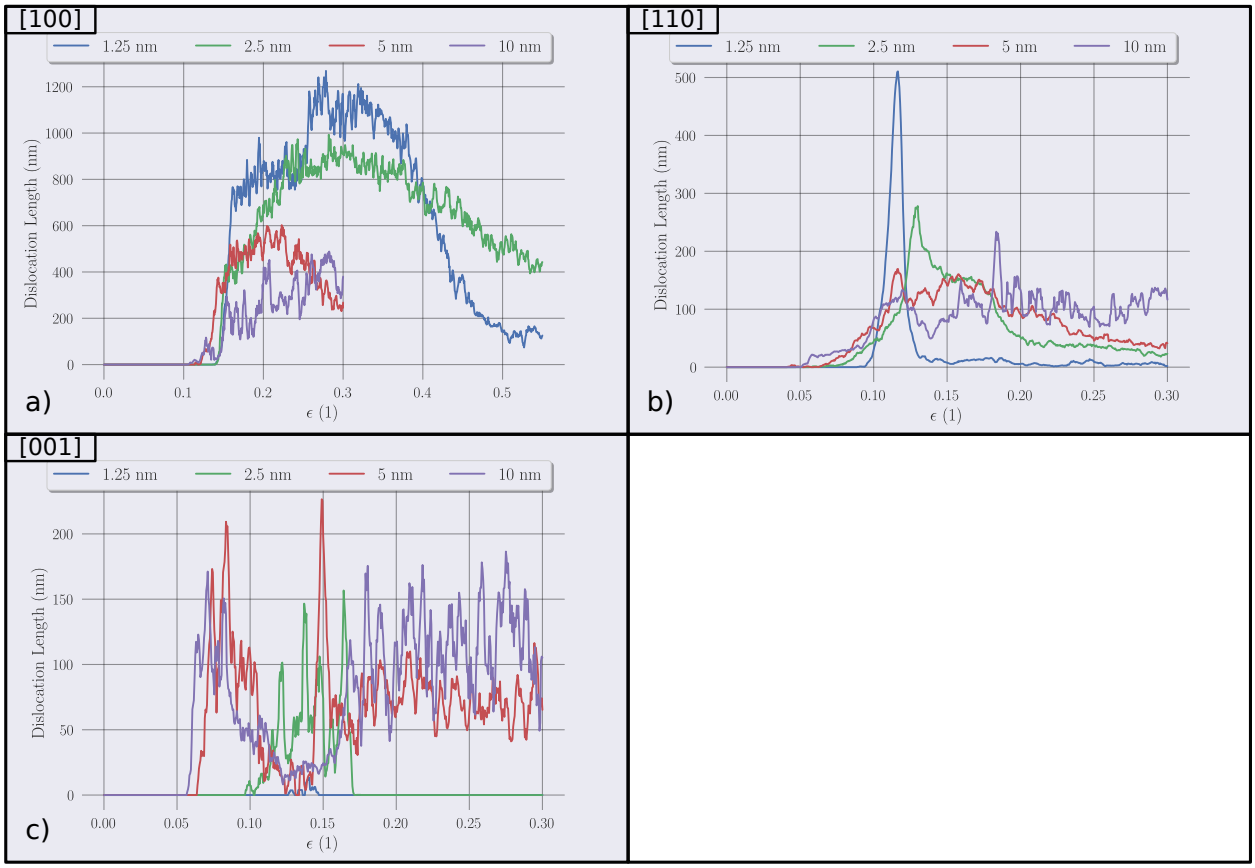

Figure 7.7: Evolution of the total length of dislocations during elongation along a) [100], b) [110] and c) [001] for $\Lambda = 1.25$, 2.5, 2.5 and 10 nm. To smooth out larger spike the rolling average of six steps is plotted in this figure.

superlattices are put under tensile loading within the interface plane, the findings from AIMD support the ones from CMD and vice versa. For strains applied along the [110] direction, *ab initio* molecular dynamics can confirm the transformation of B1-AlN to B3-AlN, and for $\Lambda =$ 1.25 and 2.5 nm also its occurrence in TiN. Furthermore, the Λ and V defect shapes can be observed in AIMD as well, and the induced interface strains lead to broken bonds initiating cracks. For elongation along the [100] direction, AIMD can support the transformation path from B1-AlN to B4-AlN as well.

Some of the findings of the simulations can be supported by high resolution transmission electron microscopy (HRTEM) and nanoindentation experiments on magnetron-sputtered AlN/TiN superlattice thin films. The nanoindentation induces strains similar to the [100] and [110] elongations. HRTEM images of the thin film show layer interpenetration and cracks at an 45° angle similar to the failure mechanisms found during CMD with [110] tension [167]. Some AlN lattice parameters determined from TEM images were found to be enlarged compared to the expected B1-AlN values and are in a better agreement with what would be expected for B3-AlN rather than B1-AlN. This hints at a B1-to-B3 lattice transformation

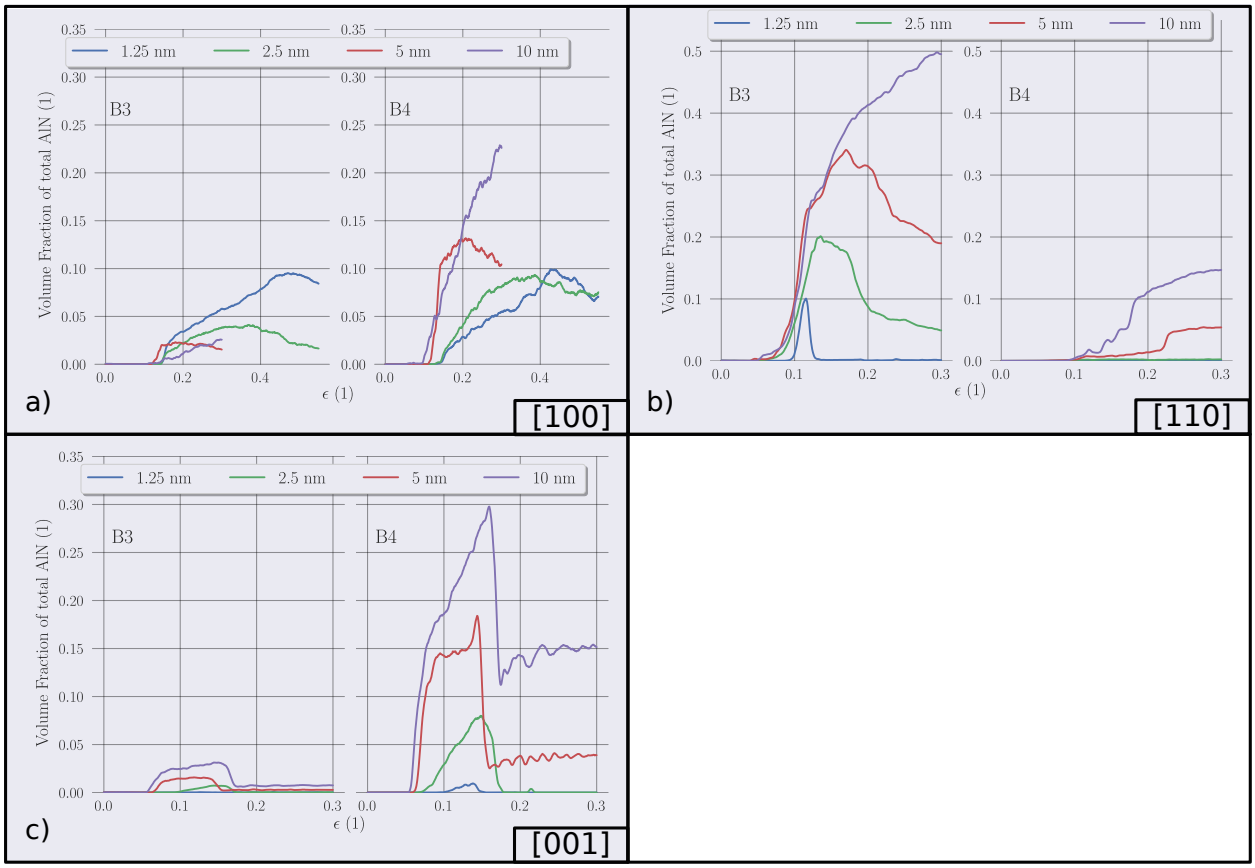

Figure 7.8: Volume fractions of B3 (left) and B4-AlN (right) within the AlN layers for tensile loading along the a) [100], b) [110] and c) [001] direction.

after nanoindentation [167]. In these experiments, no B4-AlN could be detected, however a study in ZrN/$Zr_{0.63}Al_{0.37}N$ could show strain triggered B1-to-B4 transformation [187] accompanied with improved fracture behaviour due to the volume expansion during the transformation.

7.5 Summary and Conclusion

AlN/TiN superlattices with bilayer period $\Lambda = 1.25$, 2.5, 5 and 10 nm were put under uniaxial tensile loading in [100], [110] and [001] lattice directions. Using classical molecular dynamics, the mechanisms behind plastic deformation on an atomistic level were investigated. The CMD findings are supported by both *ab initio* simulations and experiments. We were able to show that the mechanical behaviour is strongly dependent on the loading scenario and the bilayer period.

When tension is applied perpendicular to the interface ([001]), the superlattices crack parallel to the interface and show only poor plastic behaviour compared to loading parallel to the

interface ([100] and [110]), which exhibit much higher plasticity.

For all bilayer periods, elongation along the [110] direction leads to the transformation of B1-AlN to B3-AlN and later to shear bands and interpenetration of layers due to shear.

When strained along the [100] direction, the superlattices show an impact of Λ on σ_T. Further, the plasticity behaviour is also highly dependent on the bilayer period. For thin layers (Λ = 1.25 and 2.5 nm), the lattice transformation spanning multiple layers allows for effective stress distribution, greatly improving the toughness. In the larger bilayers (Λ=5 and 10 nm) the AlN transformations lead to increased strains at the interfaces with TiN, consequently leading to cracks in the TiN layers.

Our theoretical findings are supported by AIMD simulations and HRTEM investigations of AlN/TiN thin films. They support the hypothesis of formation of B3-AlN and the slip of layers in an 45° angle to the interface.

Our simulations suggest improved strength and toughness for smaller bilayer periods (Λ = 1.25 and 2.5 nm) due to transformations in AlN layers, that can stretch over the interfaces and thus greatly enhance the plasticity.

Chapter 8

Indentation of AlN/TiN superlattices

Parts of this chapter were published in ***Atomic insights on intermixing of nanoscale nitride multilayer triggered by nanoindentation*** *published in Acta materialia [188]*

8.1 Motivation

The previous chapter 7 discussed the response of tensile loading of AlN/TiN superlattices with various bilayer periods. Semi-(coherent) superlattices with a small bilayer period often lead to improved mechanical properties of the materials [1], including the AlN/TiN system [29, 54, 168]. The improved hardness and toughness have been attributed to interface coherence strains and differences in the elastic moduli [1, 81, 168]. However, this positive effect is lost when the bilayer period gets too small. The constituents of the individual layers start to intermix already during deposition. Without a sharp interface, the coherence stress fields and the difference in shear moduli vanishes, reducing the beneficial effect on mechanical properties.

However, the deposition process is not the only source of intermixing of layers, as large scale intermixing is also observed after heavy plastic deformation [189–191]. This opens the question if nanoindentation, which is commonly used to probe the hardness of thin-film materials, can induce intermixing at the interfaces as well, and if this leads to an underestimation of the hardness of the material when tested by nanoindentation.

In this chapter, we discuss the results of classical molecular dynamics simulations of nanoindentation applied to AlN/TiN superlattices. The goal was to shed light on the atomistic process during indentation and to clarify if intermixing induced by plastic deformation can occur. In addition, we investigated the impact of the superlattice bilayer period on the

hardness and plastic deformation processes.

8.2 Simulations

All molecular dynamic (MD) calculations were performed using the LAMMPS [192] code. The atomic interactions were described by an AlTiN MEAM potential [180]. To model the superlattices, alternating layers of cubic B1 ($Fm\bar{3}m$) TiN and AlN were stacked along the [001] lattice direction creating [001] interfaces. To study the effect of the bilayer period (Λ), cells with a 1:1 ratio of AlN to TiN with bilayer periods of $\Lambda = 1.25$, 2.5 and 5 nm were investigated. For each Λ, two cells, one with AlN and one with TiN as the top layer and surface. The cells have dimensions of $14.8 \times 14.8 \times 20.4$ nm with 470000 atoms. In order to study the size effect when comparing our CMD predictions with experiments, an additional cell with 0.8 nm AlN and 1.7 nm TiN with a cells size of $17.85 \times 17.85 \times 17.85$ nm and 590000 atoms was investigated.

The indenter object was considered as a rigid sphere exerting a repulsive force [193] on the atoms. It was implemented with LAMMPS *fix indent* routine and a force constant (K) of $10\,\mathrm{eV/\AA^3}$ which has proven reasonable for metals [194, 195]. A preliminary test showed a low sensitivity to smaller K values. The interaction of the indenter with the atoms can be described by

$$V(r) = \begin{cases} K(R-r)^3 & r < R, \\ 0 & r \geq R, \end{cases} \tag{8.1}$$

with R as the indenter radius and r the distance from the centre of the indenter to the atom. For the simulations, R was chosen as 3.5 nm. Before the indentation process, the cells were relaxed at 300 K with NPT thermostat. The indenter was placed in the centre of the cell 0.2 Å above the surface and advanced each step by 0.000 28 Å or 28 m/s for a duration of 200000 steps or an indentation depth (d) of about 5 nm. During the indentation process, a layer of 1 nm of atoms was fixed in its position. After the 200000 steps, the indenter was removed, and a 2 ps relaxation was performed.

The structural analysis was done with the help of OVITO [181] using the *Identify diamond structure* [182] and *Dislocation analysis* [183] functions.

It should be noted that from the very small scales in simulations, one can draw only conclusions for the initial stages of nanoindentation and the accompanying processes of plastic

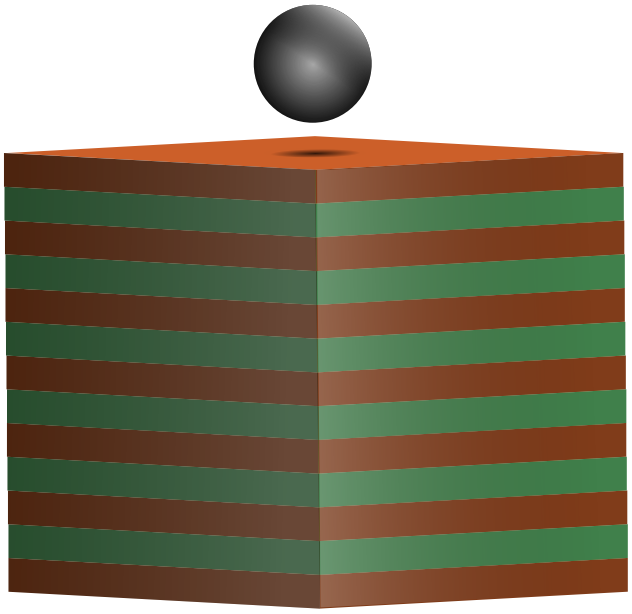

Figure 8.1: Simplified setup of an indentation simulation of a multilayered material. The indenter object is placed centred over the surface in stacking direction and then pushed with a constants speed into the material.

deformation.

8.3 Results

8.3.1 Force-displacement curves

Fig. 8.2 shows the force-displacement curves for the 1:1 AlN/TiN superlattices. A surface of TiN increases the indentation forces (F_I) by up to 25 % at $d = 1.25\,\text{nm}$ over a AlN surface. For $\Lambda = 1.25\,\text{nm}$ F_I starts to deviate from the other after half of the layer thickness. At this point, the effect of the weaker AlN layer underneath becomes noticeable. This can be for $\Lambda = 2.5\,\text{nm}$ as well, which starts to deviate from $\Lambda = 5\,\text{nm}$ at $d \approx 2.8\,\text{nm}$. At the end of the indentation, the ticker bilayer shows more resistance exhibiting a larger indentation force if a TiN layer is at the surface. The trend is reversed when an AlN layer is on top. Here the $\Lambda = 5\,\text{nm}$ shows the smallest forces with $10\,\mu\text{N}$ as maximum compared to $1.27\,\mu\text{N}$ with a TiN surface. For the smaller bilayers, the difference in F_I between the two possible surfaces starts to vanish at increasing indentation depths ending at around $1.17\,\mu\text{N}$ for both surfaces and thicknesses.

From $d = 3.5\,\text{nm}$ on the curves stat to flatten out since from this point on, the geometric factor of increasing contact area plays no role (we recall that the chosen radius of the spherical

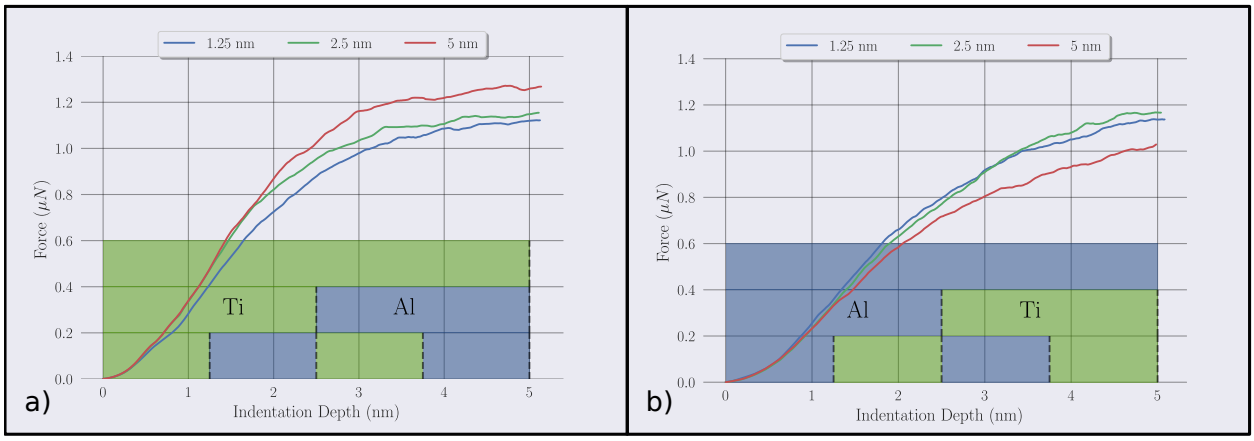

Figure 8.2: Force-displacement curves for AlN/TiN superlattices with bilayer periods of Λ = 1.25, 2.5 and 5 nm. a) TiN layer on the top, b) AlN layer on the top. The green(TiN) and blue(AlN) indicate the layer structure of the different cells.

Λ (nm)	TiN	AlN
1.25	23.1 GPa	21.0 GPa
2.5	26.1 GPa	20.1 GPa
5	27.7 GPa	18.6 GPa

Table 8.1: Hardness values at an indentation depth (d) of 2 nm for the different bilayer periods and TiN and AlN surface layers

indentor was 3.5 nm).

The hardness (H) can be calculated with :

$$H(d) = \frac{F(d)}{A(d)} \tag{8.2}$$

with F as the indentation force and A as the area of the imprint. The hardness was calculated at an indentation depth of 2 nm. TiN as the surface layer outperforms AlN surfaces independent of the bilayer period. For Λ = 1.25, 2.5 and 5 nm the supercells exhibit a hardness of 23.1, 26.1 and 27.7 GPa for TiN and 21.0, 20.1 and 18.6 GPa for AlN respectively (see also Tab. 8.1.

Intermixing and plastic deformation

Fig. 8.3 shows the development of dislocation length and quantifies the intermixing in the cell with different layer thicknesses for ALN and TiN. Figure 8.3 a) shows dislocations and crystal structures that are not of the initial B1 configuration. As one can see, the indenter influences the material only in its vicinity. A shell of amorphous material starts to form

around the indenter with a thickness of roughly 1.6 nm. Phase transformations from B1 to B3 or B4, as seen during tensile loading (Chapter 7), are mainly located at the surface to the side of the indenter and only in the cells with AlN layers on the top. B1 transforms mainly to B4 (see purple regions in Fig. 8.3 a)). During the indentation process, small areas under the indenter start to transform as well; however, these regions are not stable and continue transforming towards an amorphous state. Farther away from the indenter surface, the individual layers start to bend while maintaining an intact interface. Directly under the indenter tip, the layers get thinner due to compression on one hand and material transport to the side on the other hand.

In order to determine the composition of the amorphous region and to track the development in other parts of the cell, different volumes were probed, counting the number of Ti and Al atoms in them. The different volumes are defined by rings with a square profile (2×2 Å) different radii and the rotational axis along the [001] direction and with the same centre as the indenter. Figure 8.3d) shows compositional profile during the indentation in the four of the probed volumes (V_{A-D}, cf. Fig. 8.3c). It should be noted that the different radii lead to different total volumes, which is reflected by the total number of atoms. This makes the absolute comparison between individual volumes not accurate, and one should focus on the relative changes. Far away from the indenter (V_A), the composition stays constant over the whole simulation. Going closer to the indenter (V_B), the effect of the bending layers starts to show after $d = 3$ nm when the Al atoms start to be replaced by the Ti from the layer above. V_C and V_D were placed at the bottom of the AlN layer to prevent the effect of the curved layers. In both volumes, Ti atoms appear at indentation depth around $d = 4$ and 4.7 nm, respectively. In V_D the final composition is about 1-to-2 Al-to-Ti atoms which is the exact composition of the whole-cell hinting to the formation of a solid solution in the regions near the indentation site. Whenever Ti atoms enter formally exclusively with Al atoms filled volumes, the total number of atoms increases, hinting towards an increase in density in the plastically deformed regions.

The increase in Ti concentration in volumes V_C and V_D is facilitated by the transport of Ti atoms due to shear. In Fig. 8.4, one can see the transport of, in this case, Al atoms into the TiN layers. The figure shows only Al (blue) and N (grey) atoms which are not in the B1 structure. As one can see, Al atoms start to get dragged down into the material with the indenter, leading to intermixing after the initial indent. The panel on the right-hand side shows the imprint after removing the indenter and following relaxation. Most of the plastic deformation remains. This includes the intermixing and disappearance of the interfaces.

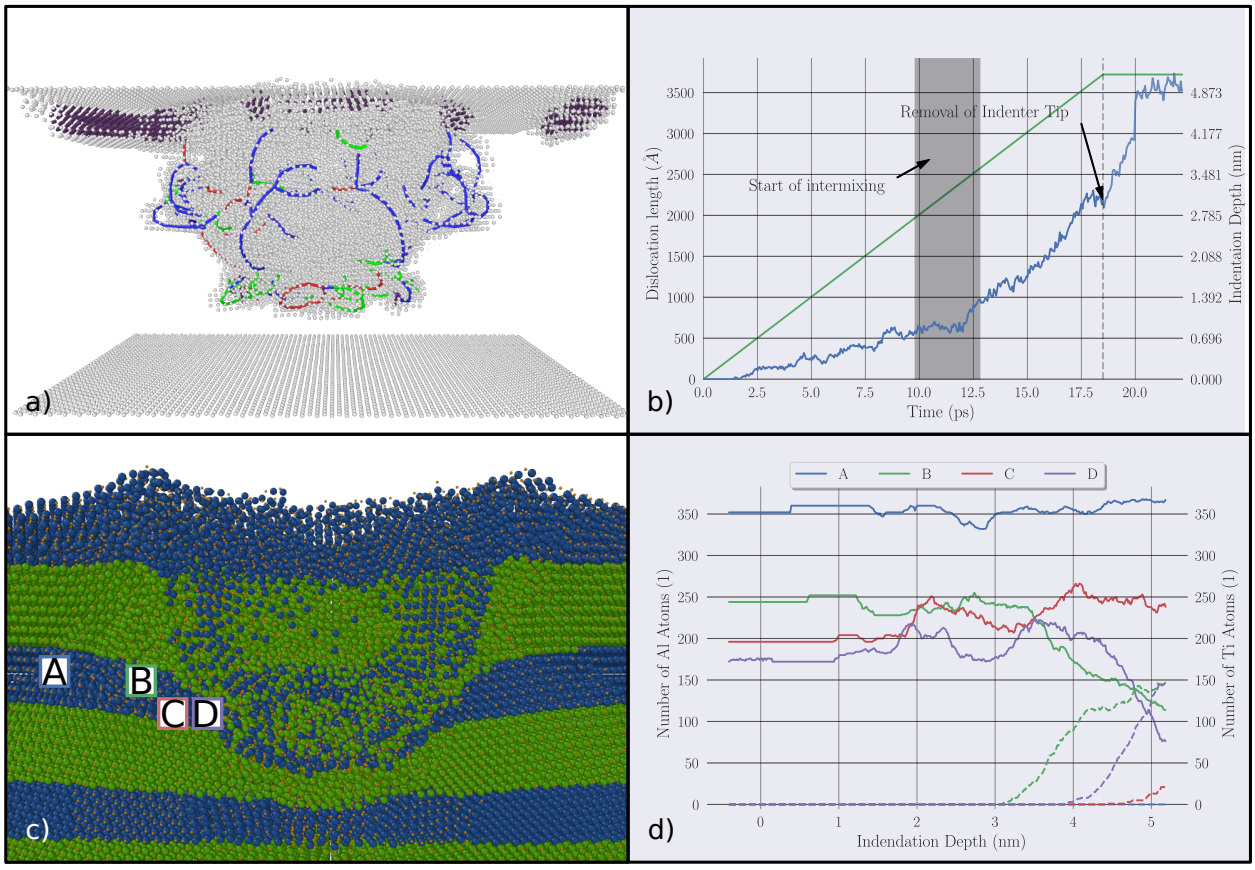

Figure 8.3: a) Structural changes and dislocations in AlN/TiN superlattices (0.7/1.4 nm) during indentation. The violet regions highlight B1 to B4 transformation of AlN. b) Development of the dislocation length during the indentation simulation. c) and d) Selected volumes and their composition during the indentation process.

The dislocations which form during the indentation span in half loops from the imprint surface and back to it. The amount of dislocation length grows slowly until the indenter is almost halfway in the material and the intermixing has started (see Fig. 8.3 b)). After removing the indenter from the cell, the dislocation length increase rapidly due to the decrease in the compressive forces exerted by the indenter object.

8.3.2 Discussion and comparison to experiments

The effect of the bilayers period on the indentation force is not straightforward to extract from the simulation results. The smaller bilayers show an increased resistance compared to the weak AlN layer in the Λ =5 nm, however, here, only one layer was probed, and no intermixing, bending etc. was allowed to happen yet. An increase would fit to the results from the tensile loading (see Chapter 7) and from literature, [54, 168] in which smaller bilayers show improved mechanical properties. The calculated hardness values (see Tab. 8.1) fit well to experimental results of AlN/TiN superlattices. For superlattices with a 1 to 1 ratio Chen

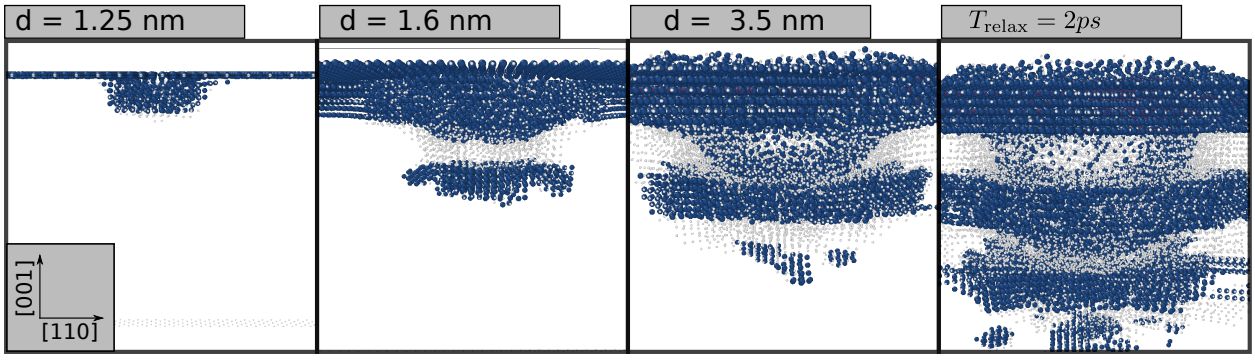

Figure 8.4: Snapshots during indentation of AlN/TiN SL with $\Lambda = 1.25\,\mathrm{nm}$ and an AlN layer at the surface at selected indentation depths a)-c). For better visualisation, all Ti atoms, as well the N (grey) and Al (blue) atoms in the B1 structure were removed. d) Remaining plastic deformation after removing the indenter relaxation of 2 ps.

et al. [196] determined a hardness of 34.0 and 31.4 GPa for $\Lambda = 7$ and 11 nm respectively. Although the calculations show lower hardness, the differences are not too big, especially for a TiN surface and $\Lambda = 5\,\mathrm{nm}$, considering different indenter shapes and only very small indentation depths during the simulations.

Comparing the two possible choices of surface layers, a thicker layer of the stronger material, in this case, TiN, seems beneficial for hardness at the very onset of nanoindentation. This could be a design approach in the future to have a thicker layer at the top of a superlattice to improve the resistance against the formation of cracks at the surface while still benefiting from the superlattice effect of the layers beneath. The lack of phase transformation (B1 to B4) in the TiN surface layer and higher Young's modulus, compared to AlN (see 5.2), could be the deciding factors in these specific pairing of materials. For a more general selection criteria, additional studies are required.

During the indentation, an amorphous shell forms around the indenter. Within this amorphous region, the interfaces start to deteriorate as intermixing of the two layers starts to happen. The process is governed by the shear exerted by the indenter on the material. Within the intermixing zones, a solid solution with the composition approaching that of the whole cells (nominal overall composition) starts to form. These findings correlate well with experimental observations of nanoindented B1 AlN/TiN layers[184], although on a much smaller scale. There, the authors found , with the help of high-angle annular dark-field (HAADF) imaging, that regions away from the imprint ($\approx$ 250–300 nm) show a still intact superlattice structure. Closer to the indentation site ($\leq 150\,\mathrm{nm}$) the structure vanishes, and a homogenous phase (identified as a solid solution) was detected.

Phase transformation to B3 or B4, as observed during the tensile loading, happens only

locally and is confined to the AlN layers and regions near to the indenter. Dislocations appear in half loops close to the imprint surface. They stay in the vicinity of the indent and do not spread through the rest of the cell.

8.4 Summary

Nanoindentation was modelled on B1 AlN/TiN superlattices within the framework of classical molecular dynamics. Dependent on the top layer material, larger bilayer periods lead to higher hardness in the initial nanoindentation phase compared to the thinner ones. Throughout the indentation process, the layers start to intermix and form a solid solution near the imprint surface, driven by the plastic deformation. These regions converge toward the composition of the whole cell. Their presence decreases the interface fraction , leading to a possible reduction in the mechanical properties. These findings are supported by experiments. Further investigation of the atomistic processes during the plastic deformation in superlattices will be desirable to gain more insight which can eventually lead to formulation of design rules for superlattices with superior mechanical properties.

Chapter 9

Summary

In this work, atomistic simulations based on Density Functional Theory and molecular dynamics were used to study the impact of defects in transition metal nitrides. Using these frameworks, we were able to investigate the defects in ways not available in experiments.

We could successfully study point defects in $Mo_xAl_{1-x}N$) and their impact on thermal stability and strength (see Chapter 4). Further assessments of the defects at temperatures above 0 eV would be a good topic for a future project as the temperature has a significant impact on the thermal stability.

The confirmation of the migration path of coherent twin boundaries (see Chapter 6) demonstrates the capability of DFT simulations to analyse even dynamic processes. Further research on the impact of different stress states on the energy barrier to overcome for any movement would be an exciting topic as stresses are the driving force behind continuous motion in one direction.

The consideration of the magnetism of CrN in the AlN/CrN and TiN/CrN (see Chapter 5) proved to be difficult in the simulations, especially in the paramagnetic cases. Here, more extensive calculations for paramagnetic CrN at elevated temperatures and/or larger cells would be advisable to get more insight into these systems. Despite the difficulties, we could show.

The results obtained from the molecular dynamics simulations of AlN/TiN superlattices (see Chapters 7 and 8) were unexpected. The possibility of observing the phase transformation of AlN was not expected but allowed us to explain the toughening of the superlattices in greater detail and with more confidence. The indentation results fit well with experimental data, although the simulations were performed on a much smaller scale with penetration of only up to four layers (for the smallest bilayer). Future calculations, to better investigate

the superlattice structure, should be performed with larger cells, indenters and to greater depths.

Bibliography

[1] R. Hahn, M. Bartosik, R. Soler, C. Kirchlechner, G. Dehm, and P. H. Mayrhofer, Scripta Materialia **124**, 67 (2016).

[2] U. Helmersson, S. Todorova, S. Barnett, J.-E. Sundgren, L. Markert, and J. Greene, Journal of Applied Physics **62**, 481 (1987).

[3] M. to Baben, M. Hans, D. Primetzhofer, S. Evertz, H. Ruess, and J. M. Schneider, Materials Research Letters **5**, 158 (2017).

[4] P. H. Mayrhofer, A. Hörling, L. Karlsson, J. Sjölén, T. Larsson, C. Mitterer, and L. Hultman, Applied Physics Letters **83**, 2049 (2003).

[5] R. O. Ritchie, Nature Materials **10**, 817 (2011).

[6] C. Mitterer, in *Comprehensive Hard Materials*, edited by V. K. Sarin (Elsevier, Oxford, 2014) pp. 449–467.

[7] C. M. Koller, R. Hollerweger, C. Sabitzer, R. Rachbauer, S. Kolozsvári, J. Paulitsch, and P. H. Mayrhofer, Surf. Coat. Technol. **259, Part C**, 599 (2014).

[8] Y. X. Xu, L. Chen, F. Pei, Y. Du, Y. Liu, and J. L. Yue, Thin Solid Films **565**, 25 (2014).

[9] R. Hollerweger, H. Riedl, M. Arndt, S. Kolozsvari, S. Primig, and P. H. Mayrhofer, Thin Solid Films **688**, 137290 (2019).

[10] F. Guo, J. Wang, Y. Du, D. Holec, P. Ou, H. Zhou, L. Chen, and Y. Kong, Appl. Surf. Sci. **470**, 520 (2019).

[11] H. Lind, F. Tasnádi, and I. A. Abrikosov, New J. Phys. **15**, 095010 (2013).

[12] P. H. Mayrhofer, R. Rachbauer, D. Holec, F. Rovere, and J. M. Schneider, in *Comprehensive Materials Processing*, edited by S. Hashmi, G. F. Batalha, C. J. V. Tyne, and B. Yilbas (Elsevier, Oxford, 2014) pp. 355–388.

[13] B. Hamid, M. to Baben, F. Nahif, D. Music, V. Schnabel, K. P. Shaha, S. Mraz, J. Bednarcik, J. Michalikova, and J. M. Schneider, J. Appl. Phys. **117**, 025302 (2015).

[14] P. H. Mayrhofer, C. Mitterer, L. Hultman, and H. Clemens, Prog. Mater Sci. **51**, 1032 (2006).

[15] S. Veprek, A. S. Argon, and R. F. Zhang, Philos. Mag. Lett. **87**, 955 (2007).

[16] J. Zalesak, M. Bartosik, R. Daniel, C. Mitterer, C. Krywka, D. Kiener, P. H. Mayrhofer, and J. Keckes, Acta Mater. **102**, 212 (2016).

[17] N. Ghafoor, I. Petrov, D. Holec, G. Greczynski, J. Palisaitis, P. O. A. Persson, L. Hultman, and J. Birch, Sci. Rep. **8**, 16327 (2018).

[18] R. Hahn, M. Bartosik, R. Soler, C. Kirchlechner, G. Dehm, and P. Mayrhofer, Scripta Materialia **124**, 67 (2016).

[19] J. Buchinger, N. Koutná, Z. Chen, Z. Zhang, P. H. Mayrhofer, D. Holec, and M. Bartosik, Acta Mater. **172**, 18 (2019).

[20] R. Hahn, N. Koutná, T. Wójcik, A. Davydok, S. Kolozsvári, C. Krywka, D. Holec, M. Bartosik, and P. H. Mayrhofer, Communications Materials **1**, 62 (2020).

[21] S. Nikolov, M. Petrov, L. Lymperakis, M. Friák, C. Sachs, H.-O. Fabritius, D. Raabe, and J. Neugebauer, Adv. Mater. **22**, 519 (2010).

[22] M. Meindlhumer, J. Zalesak, R. Pitonak, J. Todt, B. Sartory, M. Burghammer, A. Stark, N. Schell, R. Daniel, J. F. Keckes, M. Lessiak, A. Köpf, R. Weißenbacher, and J. Keckes, Nanoscale **11**, 7986 (2019).

[23] R. Daniel, M. Meindlhumer, W. Baumegger, J. Todt, J. Zalesak, T. Ziegelwanger, C. Mitterer, and J. Keckes, Mater. Des. **161**, 80 (2019).

[24] X. Chu and S. A. Barnett, Journal of Applied Physics **77**, 4403 (1995).

[25] F. H. Mei, N. Shao, J. W. Dai, and G. Y. Li, Materials Letters **58**, 3477 (2004).

[26] V. Chawla, D. Holec, and P. Mayrhofer, Journal of Physics D Applied Physics **46**, 045305 (2013).

[27] M. Friák, D. Tytko, D. Holec, P.-P. Choi, P. Eisenlohr, D. Raabe, and J. Neugebauer, New J. Phys. **17**, 093004 (2015).

[28] M. Schlögl, B. Mayer, J. Paulitsch, and P. H. Mayrhofer, Thin Solid Films **545**, 375 (2013).

[29] Z. Chen, Y. Zheng, L. Löfler, M. Bartosik, H. Sheng, C. Gammer, D. Holec, and Z. Zhang, Acta Materialia **208**, 116732 (2021).

[30] K. Kutschej, P. Mayrhofer, M. Kathrein, P. Polcik, R. Tessadri, and C. Mitterer, Surface and Coatings Technology **200**, 2358 (2005).

[31] D. G. Sangiovanni, F. Tasnádi, L. J. S. Johnson, M. Odén, and I. A. Abrikosov, Phys. Rev. Materials **4**, 033605 (2020).

[32] F. F. Klimashin, H. Euchner, and P. H. Mayrhofer, Acta Mater. **107**, 273 (2016).

[33] F. Anğay, L. Löfler, F. Tetard, D. Eyidi, P. Djemia, D. Holec, and G. Abadias, Journal of Vacuum Science & Technology A **38**, 053401 (2020).

[34] L. Hultman, J. Bareño, A. Flink, H. Söderberg, K. Larsson, V. Petrova, M. Odén, J. E. Greene, and I. Petrov, Phys. Rev. B **75**, 155437 (2007).

[35] S.-H. Jhi, S. G. Louie, M. L. Cohen, and J. Ihm, Phys. Rev. Lett. **86**, 3348 (2001).

[36] C.-S. Shin, S. Rudenja, D. Gall, N. Hellgren, T.-Y. Lee, I. Petrov, and J. E. Greene, Journal of Applied Physics **95**, 356 (2004).

[37] A. Mei, H. Kindlund, E. Broitman, L. Hultman, I. Petrov, J. Greene, and D. Sangiovanni, Acta Materialia **192**, 78 (2020).

[38] A. Madan, I. W. Kim, S. C. Cheng, P. Yashar, V. P. Dravid, and S. A. Barnett, Physical Review Letters **78**, 1743 (1997).

[39] S. Barnett and A. Madan, Physics World **11**, 45 (1998).

[40] P. B. Mirkarimi, L. Hultman, and S. A. Barnett, Applied Physics Letters **57**, 2654 (1990).

[41] M. Stueber, H. Holleck, H. Leiste, K. Seemann, S. Ulrich, and C. Ziebert, Journal of Alloys and Compounds **483**, 321 (2009), 14th International Symposium on Metastable and Nano-Materials (ISMANAM-2007).

[42] A. Wagner, D. Holec, P. H. Mayrhofer, and M. Bartosik, SSRN Electron. J. (2020), 10.2139/SSRN.3694125.

[43] R. Daniel, M. Meindlhumer, J. Zalesak, B. Sartory, A. Zeilinger, C. Mitterer, and J. Keckes, Mater. Des. **104**, 227 (2016).

[44] A. A. Griffith and G. I. Taylor, Philos. Trans. R. Soc. London. Ser. A, Contain. Pap. a Math. or Phys. Character **221**, 163 (1921).

[45] G. R. Irwin, Journal of Applied Mechanics-Transactions of the ASME **E24**, 351 (1957).

[46] M. Janssen, J. Zuidema, and R. Wanhill, *Fracture Mechanics - 2nd Edition*, Vol. 2nd edition (Spon Press, 2004).

[47] T. Anderson, *Fracture Mechanics: Fundamentals and Applications* (Spon Press, 2017).

[48] M. Sebastiani, K. E. Johanns, E. G. Herbert, and G. M. Pharr, "Measurement of fracture toughness by nanoindentation methods: Recent advances and future challenges," (2015).

[49] K. Matoy, H. Schönherr, T. Detzel, T. Schöberl, R. Pippan, C. Motz, and G. Dehm, Thin Solid Films **518**, 247 (2009).

[50] S. Brinckmann, K. Matoy, C. Kirchlechner, and G. Dehm, Acta Materialia **136**, 281 (2017).

[51] S. Zhang, E. Byon, M. Li, Y. He, F. Cai, L. Wang, H. Li, and S. Si, Thin Solid Films **519**, 1901 (2011).

[52] M. Ueno, A. Onodera, O. Shimomura, and K. Takemura, Phys. Rev. B **45**, 10123 (1992).

[53] R. Pandey, A. Sutjianto, M. Seel, and J. E. Jaffe, Journal of Materials Research **8**, 1922 (1993).

[54] M. Fallmann, Z. Chen, Z. L. Zhang, P. H. Mayrhofer, and M. Bartosik, Surface and Coatings Technology **375**, 1 (2019).

[55] Z. Zhang, X. Gu, D. Holec, M. Bartosik, P. H. Mayrhofer, and H. P. Duan, Phys. Rev. B Condens. Matter **95**, 155305 (2017).

[56] C. Kral, W. Lengauer, D. Rafaja, and P. Ettmayer, Journal of Alloys and Compounds **265**, 215 (1998).

[57] F. Lévy, P. Hones, P. Schmid, R. Sanjinés, M. Diserens, and C. Wiemer, Surface and Coatings Technology **120-121**, 284 (1999).

[58] G. Bertrand, H. Mahdjoub, and C. Meunier, Surface and Coatings Technology **126**, 199 (2000).

[59] J. Patscheider, MRS Bulletin **28**, 180–183 (2003).

[60] E. Vera, M. Vite, R. Lewis, E. Gallardo, and J. Laguna-Camacho, Wear **271**, 2116 (2011), 18th International Conference on Wear of Materials.

[61] Y. Zhong, X. Xia, F. Shi, J. Zhan, J. Tu, and H. J. Fan, Advanced Science **3**, 1500286 (2016).

[62] D. J. Ham and J. S. Lee, Energies **2**, 873 (2009).

[63] B. W. Roberts, Journal of Physical and Chemical Reference Data **5**, 581 (1976).

[64] K. S. Keskar, T. Yamashita, and Y. Onodera, Japanese Journal of Applied Physics **10**, 370 (1971).

[65] P. Mayrhofer, R. Rachbauer, D. Holec, F. Rovere, and J. Schneider, "Comprehensive materials processing," (Elsevier, Oxford, 2014) pp. 355–388.

[66] S. T. Oyama, *The Chemistry of Transition Metal Carbides and Nitrides* (Springer, Dordrecht, 1996).

[67] H. Kindlund, D. Sangiovanni, I. Petrov, J. Greene, and L. Hultman, Thin Solid Films **688**, 137479 (2019), a Special Issue "Thin Film Advances", dedicated to the 75th birthday of Professor Joe Greene.

[68] P. H. Mayrhofer, H. Willmann, and C. Mitterer, Surf. Coatings Technol. **146-147**, 222 (2001).

[69] F. Rivadulla, M. Bãobre-López, C. X. Quintela, A. Pĩeiro, V. Pardo, D. Baldomir, M. A. López-Quintela, J. Rivas, C. A. Ramos, H. Salva, J. S. Zhou, and J. B. Goodenough, Nat. Mater. **8**, 947 (2009).

[70] L. M. Corliss, N. Elliott, and J. M. Hastings, Phys. Rev. **117**, 929 (1960).

[71] J. Almer, U. Lienert, R. L. Peng, C. Schlauer, and M. Odén, J. Appl. Phys. **94**, 697 (2003).

[72] K. J. Martinschitz, R. Daniel, C. Mitterer, and J. Keckes, J. Appl. Crystallogr. **42**, 416 (2009).

[73] L. Cunha, M. Andritschky, K. Pischow, and Z. Wang, Thin Solid Films **355**, 465 (1999).

[74] B. Warcholiński, A. Gilewicz, Z. Kukliński, and P. Myśliński, Vacuum **83**, 715 (2008).

[75] H. Ljungcrantz, M. Odén, L. Hultman, J. E. Greene, and J. Sundgren, Journal of Applied Physics **80**, 6725 (1996).

[76] R. Leutenecker, B. Fröschle, U. Cao-Minh, and P. Ramm, Thin Solid Films **270**, 621 (1995).

[77] D. Gall, S. Kodambaka, M. A. Wall, I. Petrov, and J. E. Greene, Journal of Applied Physics **93**, 9086 (2003).

[78] J. Price, J. O. Borland, and S. Selbrede, Thin Solid Films **236**, 311 (1993).

[79] B. Avasarala and P. Haldar, Energy **57**, 545 (2013).

[80] M. Bartosik, R. Hahn, Z. Zhang, I. Ivanov, M. Arndt, P. Polcik, and P. Mayrhofer, International Journal of Refractory Metals and Hard Materials **72**, 78 (2018).

[81] J. Buchinger, N. Koutná, Z. Chen, Z. Zhang, P. H. Mayrhofer, D. Holec, and M. Bartosik, Acta Materialia **172**, 18 (2019).

[82] E. Bailey, N. M. T. Ray, A. L. Hector, P. Crozier, W. T. Petuskey, and P. F. McMillan, Materials **4**, 1747 (2011).

[83] P. Patsalas, C. Charitidis, and S. Logothetidis, Surf. Coatings Technol. **125**, 335 (2000).

[84] K. Balasubramanian, S. V. Khare, and D. Gall, Acta Mater. **152**, 175 (2018).

[85] D. G. Sangiovanni, V. Chirita, and L. Hultman, Phys. Rev. B **81**, 104107 (2010).

[86] H. Kindlund, D. G. Sangiovanni, L. Martínez-De-Olcoz, J. Lu, J. Jensen, J. Birch, I. Petrov, J. E. Greene, V. Chirita, and L. Hultman, APL Mater. **1** (2013), 10.1063/1.4822440.

[87] H. Kindlund, D. G. Sangiovanni, J. Lu, J. Jensen, V. Chirita, J. Birch, I. Petrov, J. E. Greene, and L. Hultman, Acta Mater. **77**, 394 (2014).

[88] J. Chen, L. L. Boyer, H. Krakauer, and M. J. Mehl, Phys. Rev. B **37**, 3295 (1988).

[89] S. Kassavetis, B. D. Ozsdolay, N. Kalfagiannis, A. Habib, J. H. Tortai, S. Kerdsongpanya, R. Sundararaman, M. Stchakovsky, D. V. Bellas, D. Gall, and P. Patsalas, J. Phys. Chem. C **123**, 21120 (2019).

[90] H. Jehn and P. Ettmayer, J. Less-Common Met. **58**, 85 (1978).

[91] G. Gassner, P. H. Mayrhofer, K. Kutschej, C. Mitterer, and M. Kathrein, Surf. Coatings Technol. **201**, 3335 (2006).

[92] S. A. Glatz, C. M. Koller, H. Bolvardi, S. Kolozsvári, H. Riedl, and P. H. Mayrhofer, Surf. Coatings Technol. **311**, 330 (2017).

[93] J. C. Schuster and H. Nowotny, J. Mater. Sci. **20**, 2787 (1985).

[94] J. F. Yang, Z. G. Yuan, Q. Liu, X. P. Wang, and Q. F. Fang, Mater. Res. Bull. **44**, 86 (2009).

[95] V. Moraes, H. Riedl, R. Rachbauer, S. Kolozsvári, M. Ikeda, L. Prochaska, S. Paschen, and P. H. Mayrhofer, Journal of Applied Physics **119**, 225304 (2016).

[96] S. Strite and H. Morkoç, Journal of Vacuum Science & Technology B: Microelectronics and Nanometer Structures Processing, Measurement, and Phenomena **10**, 1237 (1992).

[97] I. Petrov, E. Mojab, R. C. Powell, J. E. Greene, L. Hultman, and J. Sundgren, Applied Physics Letters **60**, 2491 (1992).

[98] R. F. Zhang, S. H. Sheng, and S. Veprek, Physical Review B - Condensed Matter and Materials Physics **76** (2007), 10.1103/PhysRevB.76.075208.

[99] R. F. Zhang and S. Veprek, Acta Materialia **57**, 2259 (2009).

[100] P. Hohenberg and W. Kohn, Phys. Rev. **136**, B864 (1964).

[101] W. Kohn and L. J. Sham, Phys. Rev. **140**, A1133 (1965).

[102] D. M. Ceperley and B. J. Alder, Phys. Rev. Lett. **45**, 566 (1980).

[103] J. G. Lee, *Computational materials science : an introduction* (Boca Raton, FL : Taylor & Francis, 2016).

[104] G. Kresse and J. Furthmüller, Physical Review B **54**, 11169 (1996).

[105] G. Kresse and D. Joubert, Physical Review B **59**, 1758 (1999).

[106] S. Plimpton, J. Comput. Phys. **117**, 1 (1995).

[107] M. S. Daw, S. M. Foiles, and M. I. Baskes, "The embedded-atom method: a review of theory and applications," (1993).

[108] M. I. Baskes, Phys. Rev. B **46**, 2727 (1992).

[109] B.-J. Lee and M. I. Baskes, Phys. Rev. B **62**, 8564 (2000).

[110] L. Verlet, Phys. Rev. **159**, 98 (1967).

[111] W. C. Swope, H. C. Andersen, P. H. Berens, and K. R. Wilson, J. Chem. Phys. **76**, 637 (1982).

[112] R. Yu, J. Zhu, and H. Ye, Computer Physics Communications **181**, 671 (2010).

[113] R. Hill, Proc. Phys. Soc. Sect. A **65**, 349 (1952).

[114] J. F. Nye, *Physical properties of crystals* (Clarendon Press, Oxford, 1957).

[115] S. Pugh, The London, Edinburgh, and Dublin Philosophical Magazine and Journal of Science **45**, 823 (1954).

[116] D. G. Pettifor, Materials Science and Technology **8**, 345 (1992).

[117] J. H. Rose, J. R. Smith, and J. Ferrante, Phys. Rev. B Condens. Matter **28**, 1835 (1983).

[118] P. Lazar, J. Redinger, and R. Podloucky, Phys. Rev. B Condens. Matter **76**, 174112 (2007).

[119] M. Ohring, *The Materials Science of Thin Films*, 2nd ed. (Elsevier, 2013) pp. 1–704.

[120] H. Kindlund, D. G. Sangiovanni, I. Petrov, J. E. Greene, and L. Hultman, Thin Solid Films **688**, 137479 (2019).

[121] J. Chen, L. L. Boyer, H. Krakauer, and M. J. Mehl, Phys. Rev. B **37**, 3295 (1988).

[122] N. Koutná, R. Hahn, J. Zálešák, M. Friák, M. Bartosik, J. Keckes, M. Šob, P. H. Mayrhofer, and D. Holec, Mater. Des. **186**, 108211 (2020).

[123] J. Xu, H. Ju, and L. Yu, Vacuum **103**, 21 (2014).

[124] D. Gehringer, "sqsgenerator," (2021).

[125] M. Moakher and A. N. Norris, Journal of Elasticity **85**, 215 (2006).

[126] J. Zalesak, D. Holec, I. Matko, M. Petrenec, B. Sartory, N. Koutná, R. Daniel, R. Pitonak, and J. Keckes, Acta Mater. **131**, 391 (2017).

[127] M. Lahmer, Computational Condensed Matter **21**, e00405 (2019).

[128] H. Rueß, D. Music, A. Bahr, and J. M. Schneider, Journal of Physics: Condensed Matter **32**, 025901 (2019).

[129] G. Abadias, P. Djemia, and L. Belliard, Surface and Coatings Technology **257**, 129 (2014), 25 years of TiAlN hard coatings in research and industry.

[130] L. Löfler, R. Hahn, P. H. Mayrhofer, M. Bartosik, and D. Holec, Acta Mater. **218**, 117095 (2021).

[131] P. Řehák, M. Černý, and D. Holec, Surf. Coat. Technol. **325**, 410 (2017).

[132] N. Koutná, P. Řehák, Z. Chen, M. Bartosik, M. Fallmann, M. Černý, Z. Zhang, M. Friák, M. Šob, P. H. Mayrhofer, and D. Holec, Scr. Mater. **165**, 159 (2019).

[133] N. Koutná, R. Hahn, J. Zálešák, M. Friák, M. Bartosik, J. Keckes, M. Šob, P. H. Mayrhofer, and D. Holec, Mater. Des. **186**, 108211 (2020).

[134] F. Wang, D. Holec, M. Odén, F. Mücklich, I. A. Abrikosov, and F. Tasnádi, Acta Mater. **127**, 124 (2017).

[135] L. M. Corliss, N. Elliott, and J. M. Hastings, Physical Review **117**, 929 (1960).

[136] L. Zhou, F. Körmann, D. Holec, M. Bartosik, B. Grabowski, J. Neugebauer, and P. H. Mayrhofer, Physical Review B **90**, 184102 (2014).

[137] K. Yaddanapudi, AIP Advances **8**, 125006 (2018).

[138] F. Rivadulla, M. Bãobre-López, C. X. Quintela, A. Pĩeiro, V. Pardo, D. Baldomir, M. A. López-Quintela, J. Rivas, C. A. Ramos, H. Salva, J. S. Zhou, and J. B. Goodenough, Nature Materials **8**, 947 (2009).

[139] J. E. Sundgren, B. O. Johansson, S. E. Karlsson, and H. T. Hentzell, Thin Solid Films **105**, 367 (1983).

[140] K. Momma and F. Izumi, J. Appl. Crystallogr. **44**, 1272 (2011).

[141] A. van de Walle, P. Tiwary, M. de Jong, D. L. Olmsted, M. Asta, A. Dick, D. Shin, Y. Wang, L. Q. Chen, and Z. K. Liu, Calphad **42**, 13 (2013).

[142] M. Friák, W. A. Counts, D. Ma, B. Sander, D. Holec, D. Raabe, and J. Neugebauer, Materials **5**, 1853 (2012).

[143] H. Titrian, U. Aydin, M. Friák, D. Ma, D. Raabe, and J. Neugebauer, MRS Online Proceedings Library Archive **1524** (2013/ed), 10.1557/opl.2013.41.

[144] M. Grimsditch and F. Nizzoli, Phys. Rev. B Condens. Matter **33**, 5891 (1986).

[145] M. Zhang and J. He, Surface and Coatings Technology Proceedings of the 7th International Conference on Plasma Surface Engineering, **142-144**, 125 (2001).

[146] U. P. Verma and P. S. Bisht, Solid State Sciences International Symposium on Structure-Property Relationships in Solid-State Materials, **12**, 665 (2010).

[147] P. H. Mayrhofer, D. Music, T. Reeswinkel, H. G. Fuß, and J. M. Schneider, Acta Mater. **56**, 2469 (2008).

[148] M. Grimsditch and F. Nizzoli, Physical Review B **33**, 5891 (1986).

[149] R. F. Zhang, A. S. Argon, and S. Veprek, Phys. Rev. Lett. **102**, 015503 (2009).

[150] M. L. Kronberg, Acta Metall. **5**, 507 (1957).

[151] M. F. Chisholm, S. Kumar, and P. Hazzledine, Science (80-.). **307**, 701 (2005).

[152] N. Shibata, M. F. Chisholm, A. Nakamura, S. J. Pennycook, T. Yamamoto, and Y. Ikuhara, Science (80-.). **316**, 82 (2007).

[153] P. H. Mayrhofer, C. Mitterer, L. Hultman, and H. Clemens, Progress in Materials Science **51**, 1032 (2006).

[154] R. Daniel, M. Meindlhumer, W. Baumegger, J. Zalesak, B. Sartory, M. Burghammer, C. Mitterer, and J. Keckes, Acta Materialia **122**, 130 (2017).

[155] Z. Li, P. Munroe, Z. tao Jiang, X. Zhao, J. Xu, Z. feng Zhou, J. qing Jiang, F. Fang, and Z. han Xie, Acta Materialia **60**, 5735 (2012).

[156] L. Lu, X. Chen, X. Huang, and K. Lu, Science **323**, 607 (2009).

[157] K. Lu, L. Lu, and S. Suresh, Science **324**, 349 (2009).

[158] M. Dao, L. Lu, Y. Shen, and S. Suresh, Acta Materialia **54**, 5421 (2006).

[159] J. Brown and N. Ghoniem, Acta Materialia **57**, 4454 (2009).

[160] Y. M. Wang, F. Sansoz, T. LaGrange, R. T. Ott, J. Marian, T. W. Barbee, and A. V. Hamza, Nature Materials **12**, 697 (2013).

[161] X. Ke, J. Ye, Z. Pan, J. Geng, M. F. Besser, D. Qu, A. Caro, J. Marian, R. T. Ott, Y. M. Wang, and F. Sansoz, Nature Materials **18**, 1207 (2019).

[162] X. Li, Y. Wei, L. Lu, K. Lu, and H. Gao, Nature **464**, 877 (2010).

[163] S. Yadav, X.-Y. Liu, J. Wang, R. Ramprasad, A. Misra, and R. Hoagland, Philosophical Magazine **94**, 464 (2014).

[164] H. Yu, M. Bahadori, G. B. Thompson, and C. R. Weinberger, Journal of Materials Science **52**, 6235 (2017).

[165] Y. Zhang, Z.-R. Liu, D.-W. Yuan, Q. Shao, J.-H. Chen, C.-L. Wu, and Z.-L. Zhang, Acta Metallurgica Sinica (English Letters) **32**, 1099 (2019).

[166] J. P. Perdew, K. Burke, and M. Ernzerhof, Phys. Rev. Lett. **77**, 3865 (1996).

[167] N. Koutná, L. Löfler, D. Holec, Z. Chen, Z. Zhang, L. Hultman, P. H. Mayrhofer, and D. G. Sangiovanni, Acta Mater. **229**, 117809 (2022).

[168] N. Koutná, P. Řehák, Z. Chen, M. Bartosik, M. Fallmann, M. Černý, Z. Zhang, M. Friák, M. Šob, P. H. Mayrhofer, and D. Holec, Scripta Materialia **165**, 159 (2019).

[169] D. Chen, Y. M. Wang, and X. L. Ma, Acta Materialia **57**, 2576 (2009).

[170] D. Yin, Y. Yang, X. Peng, Y. Qin, and Z. Wang, Physica E: Low-Dimensional Systems and Nanostructures **63**, 125 (2014).

[171] R. Hahn, N. Koutná, T. Wójcik, A. Davydok, S. Kolozsvári, C. Krywka, D. Holec, M. Bartosik, and P. H. Mayrhofer, Communications Materials **1**, 1 (2020).

[172] D. Holec, M. Friák, J. Neugebauer, and P. H. Mayrhofer, Phys. Rev. B **85**, 064101 (2012).

[173] J. Musil and M. Jirout, Surface and Coatings Technology **201**, 5148 (2007).

[174] F. F. Klimashin and P. H. Mayrhofer, Scripta Materialia **140**, 27 (2017).

[175] V. Moraes, L. Zauner, T. Wojcik, M. Arndt, P. Polcik, H. Riedl, and P. H. Mayrhofer, Acta Materialia **186**, 487 (2020).

[176] J. A. Yasi, L. G. H. Jr, and D. R. Trinkle, Acta Materialia **58**, 5704 (2010).

[177] M. S. Wong, G. Y. Hsiao, and S. Y. Yang, Surface and Coatings Technology **133-134**, 160 (2000).

[178] C. Stampfl and A. J. Freeman, Applied Surface Science **258**, 5638 (2012).

[179] Z. Li, S. Yadav, Y. Chen, N. Li, X. Y. Liu, J. Wang, S. Zhang, J. K. Baldwin, A. Misra, and N. Mara, Materials Research Letters **5**, 426 (2017).

[180] G. A. Almyras, D. G. Sangiovanni, and K. Sarakinos, Materials (Basel). **12**, 1 (2019).

[181] A. Stukowski, Model. Simul. Mater. Sci. Eng. **18**, 15012 (2009).

[182] E. Maras, O. Trushin, A. Stukowski, T. Ala-Nissila, and H. Jónsson, Comput. Phys. Commun. **205**, 13 (2016).

[183] A. Stukowski, V. V. Bulatov, and A. Arsenlis, Model. Simul. Mater. Sci. Eng. **20**, 085007 (2012).

[184] Y. Chen, T. Guo, J. Wang, X. Pang, and L. Qiao, Scr. Mater. **201**, 113951 (2021).

[185] N. Farrer and L. Bellaiche, Phys. Rev. B **66**, 201203 (2002).

[186] D. Holec, R. Franz, P. H. Mayrhofer, and C. Mitterer, J. Phys. D. Appl. Phys. **43**, 145403 (2010).

[187] K. Yalamanchili, I. C. Schramm, E. Jiménez-Piqué, L. Rogström, F. Mücklich, M. Odén, and N. Ghafoor, Acta Mater. **89**, 22 (2015).

[188] Z. Chen, Y. Zheng, L. Löfler, M. Bartosik, G. K. Nayak, O. Renk, D. Holec, P. H. Mayrhofer, and Z. Zhang, Acta Mater. **214**, 117004 (2021).

[189] A. Bachmaier, M. Kerber, D. Setman, and R. Pippan, Acta Mater. **60**, 860 (2012).

[190] D. Raabe, S. Ohsaki, and K. Hono, Acta Mater. **57**, 5254 (2009).

[191] X. Sauvage, F. Wetscher, and P. Pareige, Acta Mater. **53**, 2127 (2005).

[192] A. P. Thompson, H. M. Aktulga, R. Berger, D. S. Bolintineanu, W. M. Brown, P. S. Crozier, P. J. in 't Veld, A. Kohlmeyer, S. G. Moore, T. D. Nguyen, R. Shan, M. J. Stevens, J. Tranchida, C. Trott, and S. J. Plimpton, Comput. Phys. Commun. **271**, 108171 (2022).

[193] C. L. Kelchner, S. J. Plimpton, and J. C. Hamilton, Phys. Rev. B **58**, 11085 (1998).

[194] Z. Lu, A. Chernatynskiy, M. J. Noordhoek, S. B. Sinnott, and S. R. Phillpot, J. Nucl. Mater. **467**, 742 (2015).

[195] G. Ziegenhain, H. M. Urbassek, and A. Hartmaier, J. Appl. Phys. **107** (2010), 10.1063/1.3340523.

[196] L. Chen, Y. X. Xu, Y. Du, and Y. Liu, Thin Solid Films **592**, 207 (2015).

Publications

During my PhD i was able to publish most of my work in peer reviewed journals. Most of it was presented in the previous chapters. In the following a short abstract of each publication and brief summary of my contribution is given.

Precipitation-based grain boundary design alters Inter- to Trans-Granular Fracture in Nanocrystalline AlCrN Thin Films

Meindlhumer, M.,Ziegelwanger, T.,Zalesak, J.,Hans, M., Löfler, L, Spor, S., Jäger, N. , Stark, A., Hruby, H., Rostislav, D.,Holec, D., Schneider, J.M., Mitterer, C., Keckes, J., Precipitation-based grain boundary design alters Inter- to Trans-Granular Fracture in Nanocrystalline AlCrN Thin Films, Acta Materialia (submited)

Thin films produced by physical vapour deposition often lack fracture strength and toughness, which is interpreted by low cohesive energy of underdense columnar grain boundaries, despite exhibiting high hardness and indentation modulus. In this study, mechanical and structural properties of arc evaporated $Al_{0.9}Cr_{0.1}N$ thin films were analysed using micromechanical tests, electron microscopy, atom probe tomography, and in situ high-energy high-temperature grazing incidence transmission X-ray diffraction. The heat treatment resulted in the formation of regularly-distributed globular c-Cr(Al)N and elongated c-CrN precipitates at intracrystalline Cr-enriched sublayers and at grain boundaries of columnar grains with sizes of 5 and 30 nm, respectively. Consequently, in situ micromechanical testing before and after the heat treatment revealed simultaneous enhancement of Young's modulus, fracture stress and fracture toughness by 35, 65 and 10 % respectively. Together with the strengthening of the film's mechanical properties, the fracture morphology of micro-cantilevers altered from inter- to trans-crystalline fracture, proving the enhanced grain boundary cohesion. In general, the reported experimental data indicate a paramount importance of the grain boundary segregation engineering for the improvement of mechanical properties of transition

metal nitride thin films.

My contribution: I planed and designed the calculations of this study to calculate the fracture toughness of several interfaces along with an estimation of the Young's modulus, I performed and evaluated all of those calculations and provided help with writing the manuscript and discussions.

Atomistic mechanisms underlying plasticity and crack growth in ceramics: a case study of AlN/TiN superlattices

Koutná, N., Löfler, L., Holec, D., Chen, Z., Zhang, Z., Hultman, L., Mayrhofer, P. H., & Sangiovanni, D. G. (2022). Atomistic mechanisms underlying plasticity and crack growth in ceramics: a case study of AlN/TiN superlattices. Acta Materialia, 229, 117809. https://doi.org/https://doi.org/10.1016/j.actamat.2022.117809

Interfaces between components of a material govern its mechanical strength and fracture resistance. While a great number of interfaces is present in nanolayered materials, such as superlattices, their fundamental role during mechanical loading lacks understanding. Here we combine ab initio and classical molecular dynamics simulations, nanoindentation, and transmission electron microscopy to reveal atomistic mechanisms underlying plasticity and crack growth in B1 AlN(001)/TiN(001) superlattices under loading. The system is a model for modern refractory ceramics used as protective coatings. The simulations demonstrate an anisotropic response to uniaxial tensile deformation in principal crystallographic directions due to different strain-activated plastic deformation mechanisms. Superlattices strained orthogonal to (001) interfaces show modest plasticity and cleave parallel to AlN/TiN layers. Contrarily, B1-to-B3 or B1-to-B4(Bk) phase transformations in AlN facilitate a remarkable toughness enhancement upon in-plane [110] and [100] tensile elongation, respectively. We verify the predictions experimentally and conclude that strain-induced crack growth via loss of interface coherency, dislocation pinning at interfaces, or layer interpenetration followed by formation of slip bands can be hindered by controlling the thicknesses of the superlattice nanolayered components

My contribution: I planed and designed the MD calculations of this study, I performed and evaluated all MD calculations and provided help with writing the manuscript and discussions.

Mechanical properties of CrN-based superlattices: Impact of magnetism

Löfler, L., Hahn, R., Mayrhofer, P. H., Bartosik, M., & Holec, D. (2021). Mechanical properties of CrN-based superlattices: Impact of magnetism. Acta Materialia, 218, 117095. https://doi.org/10.1016/J.ACTAMAT.2021.117095

Superlattices represent an important design concept for materials with exceptional properties. In this work, we report on the influence of different interface orientations and magnetic configurations of CrN in B1 CrN/(TiN,AlN) superlattices on their mechanical and the structural properties studied with the help of density functional theory. The oscillations of interplanar spacings, formerly linked to the cleavage strength in similar material systems, were found to be in no correlation with the magnetic moments of individual CrN planes. An explicit consideration of the interfaces is important for an accurate estimation of elastic constants. In this context, the continuum mechanics-based Grimsditsch and Nizzoli method ignoring interface properties yields even qualitatively wrong results. Similarly, our calculations show that the ferromagnetic state of CrN as an approximation of (computationally much more demanding) paramagnetic magnetic state does not provide correct predictions of the material behaviour. In other words, explicit treatment of the magnetic moments as well as the interfaces is necessary for qualitatively correct modelling of CrN-based superlattices. Finally, the theoretically predicted elastic constants and fracture toughness values were corroborated by CrN/TiN micro-cantilever experiments.

My contribution: I planed and designed the calculations of this study; I performed all calculations, evaluation and wrote the manuscript.

Real-time atomic-resolution observation of coherent twin boundary migration in CrN

Chen, Z., Zheng, Y., Löfler, L., Bartosik, M., Sheng, H., Gammer, C., Holec, D., & Zhang, Z. (2021). Real-time atomic-resolution observation of coherent twin boundary migration in CrN. Acta Materialia, 208, 116732. https://doi.org/10.1016/J.ACTAMAT.2021.116732

In this joint work using sing in-situ atomic-resolution electron microscopy and density functional theory were employed to study twin boundaries in CrN. We were able to show two different twin boundary defect (TD) nucleation and CTB migration modes at the CTB/ITB (incoherent twin boundary) and CTB/surface junctions. A new twin defect nucleation and

CTB migration mode are observed from the CTB/surface junction. We show that such CTB migration is associated with a boundary structure alternating from an N-terminated to Cr-terminated, involving Cr and N atom respective motion, i.e., asynchronous CTB migration. We further reveal the dynamic and thermodynamic mechanism of such asynchronous migration through strain analysis and DFT simulations. Our findings uncover an atomic-scale dynamic process of defect nucleation and CTB migration in a binary system, which provides new insight into the atomic-scale deformation mechanism in complex materials.

My contribution: I planed and designed the calculations of this study to determine the energy barrier of the CTB, I performed and evaluated all calculations and provided help with writing the manuscript and discussions.

Atomic insights on intermixing of nanoscale nitride multilayer triggered by nanoindentation

Chen, Z., Zheng, Y., Löfler, L., Bartosik, M., Nayak, G. K., Renk, O., Holec, D., Mayrhofer, P. H., & Zhang, Z. (2021). Atomic insights on intermixing of nanoscale nitride multilayer triggered by nanoindentation. Acta Materialia, 214, 117004.
https://doi.org/10.1016/j.actamat.2021.117004

Mechanical properties of nanoscale multilayer coatings are to a large extent governed by the number of interfaces and their characteristics. While for a reduced layer thickness, increasing strength and toughness values have been reported, properties degrade for layer thicknesses of just several nanometers. Here, we report on an entirely overlooked phenomenon occurring during the indentation of nanolayers, presum- ably explaining the degradation of properties. Nanoindentation, commonly used to determine properties of hard coatings, is found to disrupt and intermix the multilayer structure due to the deformation im- posed. Detailed electron microscopy studies and atomistic simulations provide evidence for intermixing in an epitaxial transition metal nitride superlattice thin film induced by nanoindentation. The formation of a solid solution reduces the interfacial density and leads to a sharp drop in the dislocation density. Our results confirm that plastic deformation causes the microstructure instability of nitride multilayer, which may further improve our understanding of multilayer strength mechanisms.

My contribution: I planed and designed the calculations of this study to performe MD nanoindentaion, I performed and evaluated all calculations and provided help with writing the manuscript and discussions.

My contribution: I planed and designed the calculations of this study, I performed and evaluated all ND calculations and provided help with writing the manuscript and discussions.

Surface stress of gold nanoparticles revisited.

Holec, D., Löfler, L., Zickler, G. A., Vollath, D., & Fischer, F. D. (2021). Surface stress of gold nanoparticles revisited. International Journal of Solids and Structures, 224, 111044. https://doi.org/10.1016/J.IJSOLSTR.2021.111044

The surface energy has been one of the topics of atomistic research for nanoparticles in the last decades. However, the physical role of surface stress and its quantification have been a lot less an object of research. Assumptions for the surface stress, going back to the thermodynamic basis of continua, have been popular. As an example the surface stress (state) follows as derivatives of the surface energy with a rather classical" evolution equation for the deformation energy. The current concept introduces a combination of atomistic modelling and continuum mechanics for a core-shell system. Considering crystalline and amorphous gold nanoparticles with radii in the range of 1 nm to 12 nm, we are finally able to independently calculate the values of surface stress and surface energy, both slightly decreasing with the increasing particle radius. Surprisingly large values of surface stress are predicted for the case of amorphous nanoparticles.

My contribution: For this publication I calculated the elastic constants of Au with classical molecular dynamics and provided help with writing the manuscript and discussions.

Structure, stress, and mechanical properties of Mo-Al-N thin films deposited by dc reactive magnetron cosputtering: Role of point defects

Anğay, F., Löfler, L., Tetard, F., Eyidi, D., Djemia, P., Holec, D., & Abadias, G. (2020). Structure, stress, and mechanical properties of Mo-Al-N thin films deposited by dc reactive magnetron cosputtering: Role of point defects. Journal of Vacuum Science & Technology A, 38(5), 053401. https://doi.org/10.1116/6.0000292

In this work, the structural and mechanical properties of ternary Mo-Al-N alloys are investigated by combining thin film growth experiments and density functional theory (DFT) calculations. thin films ($\tilde{3}$00 nm thick), with various Al fractions ranging from x = 0 to

0.5 and nitrogen-to-metal (Al +Mo) ratio ranging from y = 0.78 to 1.38, were deposited by direct-current reac- tive magnetron cosputtering technique from elemental Mo and Al targets under Ar + N2 plasma discharges. The Al content was varied by changing the respective Mo and Al target powers, at a fixed N2 (20 SCCM) and Ar (25 SCCM) flow rate, and using two different substrate temperatures Ts = 350 and 500 °C. The elemental composition, mass density, crystal structure, residual stress state, and intrinsic (growth) stress were examined by wavelength dispersive x-ray spectroscopy, x-ray reflectivity, x-ray diffraction, including pole figure and $\sin^2 \psi$ measurements, and real-time in situ wafer curvature. Nanoindentation tests were carried out to determine film hard- ness H and elastic modulus EIT, while the shear elastic constant C44 was measured selectively by surface Brillouin light spectroscopy. All deposited $Mo_xAl_{1-x}N$ films have a cubic rock-salt crystal structure and exhibit a fiber-texture with a [001] preferred orientation. The incorporation of Al is accompanied by a rise in nitrogen content from 44 to 58 at. %, resulting in a significant increase (2 %) in the lattice parameter when x increases from 0 to 0.27. This trend is opposite to what DFT calculations predict for cubic defect-free stoi- chiometric Mo1-xAlxN compounds and is attributed to variation in point defect concentration (nitrogen and metal vacancies) when Al substitutes for Mo. Increasing Ts from 350 to 500 °C has a minimal effect on the structural properties and phase composition of the ternary alloys but concurs to an appreciable reduction of the compressive stress from -5to -4 GPa. A continuous increase and decrease in transverse sound velocity and mass density, respectively, lead to a moderate stiffening of the shear elastic constant from 130 to 144 GPa with increasing Al fraction up to x = 0.50, and a complex and nonmonotonous variation of H and E_{IT} is observed. The maximum hardness of 33 GPa isfound forthe $Mo_{0.81}Al_{0.19}N_{1.13}$ film, with nitrogen content close to the stoichiometric composition. The experimental findings are explained based on structural and elastic constant values computed from DFT for defect-free and metal- or nitrogen-deficient rock-salt MoAlN compounds.

Fracture properties of thin film TiN at elevated temperatures

Buchinger, J., Löfler, L., Ast, J., Wagner, A., Chen, Z., Michler, J., Zhang, Z. L., Mayrhofer, P. H., Holec, D., & Bartosik, M. (2020). Fracture properties of thin film TiN at elevated temperatures. Materials and Design, 194(June), 108885. https://doi.org/10.1016/j.matdes.2020.108885

We provide an experimental and theoretical description of the high temperature fracture behaviour of TiN thin films. For this, we employ molecular dynamics and density functional

theory, to show that the surface energies drop insignificantly between 0 and 1000 K. We utilise these results to predict a slight decrease of the fracture toughness over the aforementioned temperature range. For the experimental perspective, we use unbalanced DC reactive magnetron sputtering to synthesise a TiN film, on which we perform in situ high temperature microcantilever bending tests. Upon increasing the testing temperature from room temperature to 773 K our results present a slight, irreversible decrease of K_{IC}, once the deposition temperature of the film (653 K) is exceeded. Based on our theoretical groundwork, as well as complementary data produced by X-ray diffraction, nanoindentation, transmission electron microscopy, and wafer curvature measurements, we identify growth defect recovery as the main reason behind the decrease of K_{IC}. We observe no change in the deformation and/or fracture mechanism of TiN across the experimentally investigated temperature range. Using an analytical model based on continuum mechanics, we estimate the influence of macro residual stresses on the temperature-dependent fracture toughness of TiN attached to a Si (100) wafer.

My contribution: I planed and designed the calculations of this study to determine the temperature dependent surface energies, I performed and evaluated all calculations and provided help with writing the manuscript and discussions.